VISER
www.viserdata.com

RESEARCH AND APPLICATION OF MATERIALS SCIENCE

ISSN 2661-4464(online) 2661-4456(print)
Volume 6 No. 2 2024

COMPANY INTRODUCTION

Viser Technology Pte. Ltd. was founded in Singapore with branch offices in both Hebei and Chongqing, China. Viser focuses on publishing scientific and technological journals and books that promote the exchange of scientific and technological findings among the research community and around the globe. Despite being a young company, Viser is actively connecting with well-known universities, research institutes, and indexation database, and has already established a stable collaborative relationship with them. We also have a group of experienced editors and publishing experts who are dedicated to publishing high-quality journal and book contents. We offer the scholars various academic journals covering a variety of subjects and we are committed to reducing the hassles of scholarly publishing. To achieve this goal, we provide scholars with an all-in-one platform that offers solutions to every publishing process that a scholar needs to go through in order to show their latest finding to the world.

Research and Application of Materials Science

Publisher: Viser Technology Pte. Ltd.

ISSN: 2661-4464(online)
2661-4456(print)

Frequency: Semi-annual

Add.: 111 North Bridge Rd, #21-01 Peninsula Plaza, Singapore 179098

https://www.viserdata.com/

Research and Application of Materials Science

Volume 6 No.2 (2024)

CONTENTS

Viser Technology Pte. Ltd.
Research and Application of Materials Science
DOI: 10.33142/rams.v6i2.14412

Research Article Open Access

Research Progress on the Recycle and Reuse of Wasted Aluminum Substrates of CTP Plates

Danchen LIU

Nanjing Jiangbei New Area Construction and Transportation Bureau, Nanjing, Jiangsu, 210000, China

*Corresponding Author: Danchen LIU, E-mail: 754806441@qq.com

Abstract

Recycling and reuse of wasted materials is a key topic in materials research, providing a new material recycling path for green manufacturing. As a national pillar industry, the greening and intelligent upgrading of the printing industry is an inevitable trend in the development of modern printing. To better implement the national "dual-carbon strategy" and cultivate new quality productivity, this paper presents a systematic literature review on the research progress of the recycling and reuse techniques of used aluminum substrates of CTP plates for offset printing. Analysis of existing industry data and literature shows that aluminum substrate of used CTP plates meets the recycle size and required physical and chemical characteristics, but the current research has not yet fully taken into account the integration of technical innovation in the recycling and reuse of aluminum substrate of used CTP plates. Based on material eco-cycling perspectives such as sustainable material utilization design, wasted material recycling device and multi-material fine separation process, this paper provides a unique outlook on the integrated development trend of recycling and reuse of aluminum substrates of used CTP plates, and provides greening case references for the safe management of wasted materials in the modern offset printing industry.

Keywords: *Aluminum substrate; CTP plate; Property analysis; Material reuse; 3D printing; Waste management*

1 Introduction

Computer to plate (CTP), is a digital pre-press plate production technology with high efficiency and environmental protection, which is to use computers and typesetting software for digital processing of the original text and images by typesetting and editing [1]. Computer direct-to-plate process eliminates the need for film, realizing the direct connection from the computer to the printing, both to save the photopolymer plate (PS plate) with a large number of necessary materials and exposure processing equipment, while reducing the number of image transfer to improve the rate of image reproduction.

CTP plates are plates produced directly using a highly efficient and ecological digitizing technology, which has become a common green plate for modern offset printing companies. According to research data from Verified Market Reports, the global CTP plate market size reached USD 4.17 billion in 2023 and is expected to grow to USD 5.08 billion by 2030 [2]. Data from Zhiyan Consulting shows that China's CTP plate production amounted to 49.98 million square meters in 2021, with imports totaling 3.193 million square meters and exports reaching 16.2236 million square meters, resulting in a domestic demand of 34.0757 million square meters for CTP plates [3]. The China's CTP plate market can be divided into five regions: East China, Central South, North China, Northeast, and Western China. Among these, East China and Central South account for 77.23% of the market share. CTP plate production enterprises in China are mainly located in regions such as Shanghai, Jiangsu, Zhejiang, Sichuan and Henan, with obvious differences among the production processes used in various consuming regions. As the demand and production of CTP plates in China are increasing, the number of discarded CTP plates that have exceeded their service life is also increasing dramatically, which implies that the exploration of safe and efficient recycling and reuse under the green printing strategy has become even more important and urgent.

CTP plates are categorized into four main types according to the imaging principle of plate production: photographic CTP plates, thermal CTP plates, violet laser CTP plates and other CTP plates [4], as shown in Figure 1. The photosensitive CTP plate contains photopolymerized CTP plate and silver salt CTP plate. This CTP plate type system utilizes the photosensitive material on the aluminum substrate, which undergoes a photopolymerization reaction after exposure, and displays the graphic through the photographic process. Photopolymerized CTP plate consists of three parts: a sand-metalized aluminum substrate, a

Received on October 31, 2024; Accepted on November 30th, 2024

photopolymerization layer (composed of film-forming resins, infectious materials, photoinitiators, monomers or zwitterions, stabilizers, and other additives), and a protective layer (polyvinyl alcohol oxygen barrier). The silver-salt CTP plates are mainly divided into silver-salt diffusion transfer plate (mainly composed of plate substrate, silver-salt emulsion layer and physical imaging layer) and composite silver-salt & PS plate (pre-sensitized photopolymer layer, bonding layer and silver halide emulsion layer are coated on the roughened and anodized aluminum plate substrate in turn). With cost advantages of silver salt CTP plate was produced only by Agfa, which was controversial for silver contamination of the waste liquid in the production process of the CTP plate, but only a small portion of the printing enterprises are now in use. Thermal sensitive CTP plates include thermal cross-linking plates, thermal ablative plates and thermal transfer plates. This type of CTP plate triggers a physical or chemical change in the polymer material through heat to form a graphic on the aluminum substrate. Thermal cross-linked CTP plates are mainly composed of a roughened aluminum plate and a single PS photographic layer that receives infrared exposure, while thermal fusion CTP plates are mainly composed of an aluminum plate that does not need to be roughened, an ink-friendly layer and a PVA layer (for conventional offset printing) or a silicone layer (for waterless offset printing). The violet laser CTP plates use the high energy of violet laser in the range of 405 ～ 410 nm to trigger a polymerization reaction of the resin in the photosensitive layer to form a graphic on an aluminum substrate, which is suitable for commercial and newspaper printing with high-resolution requirements [5]. Violet laser CTP plates are mainly composed of an aluminum substrate, a violet light-sensitive layer, and a protective layer of polyvinyl alcohol (PVA), which can be operated under a yellow safety light and have a long lifetime. The composition of these CTP plates reflects the application of different imaging techniques and material science to meet the efficiency, quality and environmental requirements in the offset printing industry. Each type of CTP plate has its own unique advantages and application scenarios, and its substrate is often made of lightweight and strong aluminum sheet.

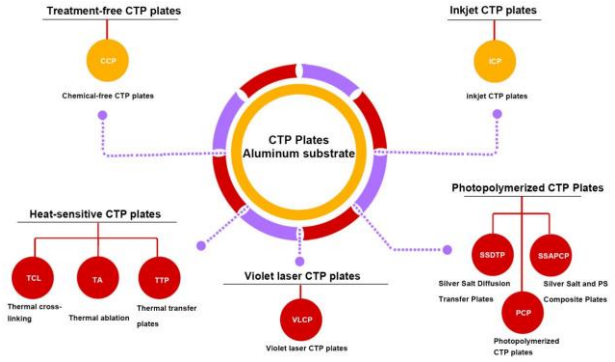

Figure 1 Classification of CTP plates

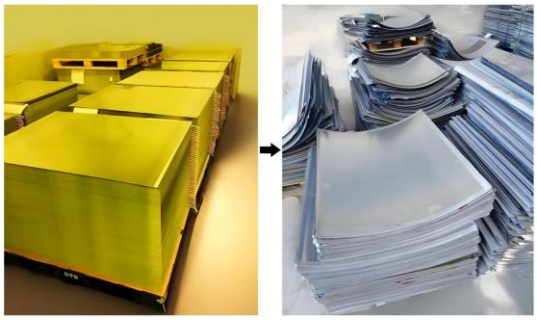

Figure 2 Before and after printing state of aluminum substrate of CTP plates

With the upgrading of the global green printing development, the CTP plate production system continues to innovate with green processes and develops treatment-free CTP plates and inkjet CTP plates. In a broad sense, treatment-free CTP plates can be printed on the printing machine without any subsequent processing after exposure and imaging on the platesetting equipment. Narrowly speaking, treatment-free CTP plates don't need chemical treatment after exposure and imaging on the platesetter, but there will still be individual non-chemical treatment processes. The international suppliers of treatment-free CTP plates include Fujifilm, Kodak, and Agfa, while domestic suppliers include LeKai Huaguang [6]. Inkjet CTP plates are formed by inkjet printing special ink directly on the surface of the aluminum substrate to form a graphic area (oleophilic), while no ink is printed on the part of the non-graphic area (hydrophilic), cured to form a printing plate for on-machine printing [7]. The main suppliers of inkjet CTP plates include well-known companies such as Glunz & Jensen, Zhongke Naxin, and Chengdu Xintu. Since the graphic information on the CTP plate is disposable, the graphic area on the aluminum substrate is cured after printing and can't be removed by conventional methods and restored to its original state for reuse. The current CTP plate production system is almost using aluminum sheet as the substrate, only a very small percentage of the flexible polymer substrate (e.g., polyester substrate) is used. In addition, the natural drying of spent CTP plates mainly contains aluminum substrate and residual curing layers, which can't be directly reused for new plates to be discarded by printing managers in warehouses or pulled to recycling stations, as shown in Figure 2. As a result, there is an urgent need for research on the reuse of spent CTP plates to focus on how to safely and efficiently utilize aluminum substrates by removing the residual curing layers, and to provide a high-value safety management case for the material innovation application for lower cost and higher efficiency of global green printing enterprises.

2 Analysis of Physical and Chemical Properties of Aluminum-based CTP Plates

The main process flow for producing

aluminum-based CTP plates in most enterprises is as follows: the raw material is annealed, cold rolled, straightened, longitudinal cut into aluminum sheet, then conducted the following steps: degreasing, electrolytic sanding, anodizing, photopolymer coating, drying. Among these, the cold rolling and drying procedures directly affect the physical and chemical properties of the aluminum substrate, as well as the number of printings it can endure[8]. Saeed Yaghoubi et al. carried out experimental tests to optimize the shape of aluminum substrate by varying the process temperature and underpressure rate, and analyzed the final thickness distribution and shape accuracy using a digital image correlation system to improve the physical forming accuracy of aluminum substrate [9]. Jia et al. explored the effects of cold rolling deformation and baking on the microstructure, mechanics, and physical and chemical properties of 1060 aluminum alloy for cast-pressed CTP plate, and found that better formability and higher print resistance were achieved with the first pressing rate of 58.2% and the baking treatment of 280 ℃×5 min[10]. On the other hand, Huang approached the target plate shape curve by adjusting the billet plate shape index, and carried out optimization research on rolling and finishing processes, so as to control the final rechecked plate shape of the aluminum substrate of the CTP plate within 6.0I units[11]. In addition, the modern CTP plate production line is basically equipped with automatic defects online detection equipment, such as Japan's FUTEC surface defect detection system for the aluminum coil with a width of 1.9 m and thickness of 0.28 mm when the highest line speed up to 250 m/min. Shen et al. introduced the human visual attention mechanism into the adaptive online detection algorithm of different types of defects on the surface of CTP plates, and reached a resolution of 0.1 mm for rapid detection of multiple types of defects on aluminum-based CTP plates with an average detection accuracy of 96.3%[12]. Meanwhile, in the optimization research of printing resistance of aluminum-based CTP plate, Yang found that the second phase composed of Fe element affects the surface properties of aluminium substrate through the energy spectrum analysis of the original aluminum sample of aluminium substrate, and proposed that controlling the content of Fe and Si and selecting the preferred grain refining methods can effectively improve the printing number of aluminium-based CTP plate. Thus, it can be seen that current research on the physical and chemical properties of aluminum substrates has covered the entire production process of aluminum-based CTP plates and also reflects the dimensional and surface characteristics of each aluminum substrate during both the fabrication and usage stages.

The aluminum substrates of CTP plates exhibit excellent print resistance, high resolution, and strong resistance to temperature and humidity. The commonly used aluminum alloys for CTP plates are 1050, 1060, and 1070, with aluminum content of ⩾99.50%, ⩾99.60%, and ⩾99.70%, respectively. Aluminum coils for CTP plates are usually processed in H18 or H19, which are in a high state of hardness and strength. The thickness of the aluminum substrate of the CTP plate is generally 0.280mm, and some adopt the thickness of 0.275mm. Aluminum substrate has good physical and mechanical properties, manifested in high mechanical stiffness, easy to form, good stability and fine surface treatment. According to the imaging principle of CTP plate and the difference of materials used, the aluminum substrate of CTP plate can also be divided into sand mesh aluminum substrate, roughened and anodized aluminum substrate. Among them, the sanded aluminum substrate has a multi-layered sand structure on the surface, which in turn exhibits good ductility and formability. Commercially available aluminum substrate for CTP plates have a mesh value of Ra of 0.45 to 0.60 μm, with an ideal value of 0.45 to 0.55 μm. The surface of the roughened and anodized aluminum substrate is formed by electrolytic roughening and anodic oxidation of the alumina film layer, which is high in hardness, good in chemical stability, and has high tensile strength and corrosion resistance. For aluminum substrates from discarded CTP plates, the common process involves washing off the ink adhered to the surface, followed by physical stripping of the cured layer and flat pressing, which quickly forms a relatively intact aluminum sheet. In some cases, discarded CTP plates with scratches on the surface due to usage can be coated with a layer of water-based paint to cover or decorate the surface, improving its appearance and making it more suitable for reuse in applications where a good surface finish is required.

In the printing enterprises, especially offset printing enterprises, the workshop needs CTP plate format type and quantity are more, and equipped with CTP plate making system plate format is larger, direct production out of the CTP plate usually need to be cut and punched in order to meet the different printing business requirements. The cutting of wide-format CTP plates can be done either manually with a specific tool or with a simple plate cutting device. This provides precise and easy shaping convenience for the innovative subsequent reuse of spent CTP plate substrates, allowing on-site reuse of spent CTP plate substrates without the need to purchase additional large-scale processing equipment. Acquiring an affordable wire extrusion unit with an FDM-type 3D printer is not a tough choice for a printing company or workshop to achieve a more flexible reuse of the aluminum substrate.

3 Current Situation Analysis of Recycling Technology for Spent Aluminum Sheets

Current Status of Recycling and Utilization Technology for Waste Aluminum Sheets

Scrapped metal sheets are becoming increasingly

valuable for reuse because of global warming, geopolitical instability and rising raw material costs. Aluminum sheet is widely used due to its light weight, high strength, good densification, and easy cutting, and its applications are mainly in the form of aluminum foil, aluminum sheet, aluminum plate, aluminum cans, and aluminum structures. The recycled volume of wasted aluminum in China continues to be high, growing from 4 million tons in 2015 to 7.8 million tons in 2023. Liu et al. summarized the research progress on primary grade recycling of aluminum cans and demonstrated that recycled aluminum cans have large advantages in terms of energy consumption and carbon emissions [13]. Li et al. summarized the advantages and disadvantages of the existing process methods, such as downgraded recycling, grade-preserving recycling and overgraded recycling of waste aluminum, and thus predicted the most promising technology for recycling waste aluminum [14]. Recycling degree of aluminum sheets varies from actual industrial applications, and its common challenge lies in the effective complexes separation and the precise removal of impurities. Based on the concept of "treating waste with waste", Liu et al. proposed to utilize the aluminum-containing strong alkaline waste liquid after alkali leaching and mechanical separation to compound with polymeric aluminum chloride for the aluminum separated from aluminum-plastic composite packaging waste as well as sewage treatment [15]. International packaging giant Tetra Pak, which is dedicated to the collection and recycling of used beverage paper packaging, has successfully facilitated the development of a 3D printing filament called ALFAPAK 3D between international Ecorevive SRL and material supplier Maip Compounding on aluminum-plastic composites from used beverage paper packaging [16]. Aluminum wire material shows great potential for metal 3D printing applications, pending the development of low-cost new aluminum alloy wire composite forming technology, which will lead to a large-scale solution for high-value reuse of small- and medium-sized aluminum sheets.

Gu et al. successfully separated the cathode material of used lithium-ion batteries from the aluminum foil components using an innovative method combining glycerol heating and mechanical agitation [17], without elaborating on specific aluminum foil reuse ideas. As aluminum sheet material becomes thicker and larger in practical applications, research on its recycling technology needs to move from simple recycling to integrated recycling. Alhefnawi highlights the priority of using recyclable aluminum panels for facade cladding materials in school buildings from a circular economy perspective, even though the thermal comfort of aluminum cladding requires a higher energy budget [18]. From a quantitative analysis of recycling strategies, Zaheer et al. proposed a point-by-point incremental molding process for the reuse of scrapped components with numerical simulation to reduce the geometric deviation, then obtained a robust component with finite deformation [19]. Meanwhile, the reforming recycling route is analyzed in terms of environmental performance with the traditional recycling route and solid recycling route, and demonstrates the advantages of energy saving and emission reduction [20]. Li et al. proposed a laser irradiation followed by mechanical stripping method for recycling the EVA layer on the backside of solar cells in crystalline silicon photovoltaic (PV) modules with respect to the efficient debonding of ethylene-vinyl acetate (EVA) copolymers [21]. Farioli et al. presented a framework for reproduction of curved alloy panels for automotive body panels and optimized the process parameters by using 0.8 mm DC 0.4 alloy panels with specific radii reshaped and flattened under different conditions [22]. For the reuse technology of spent aluminum-based extrusion die, Li Jian empirically proved through practical data that the aluminum profiles produced by using the refurbished and modified spent die can meet the requirements of construction use [23]. According to the production statistics of aluminum plates and strips from China Nonferrous Metals Processing Industry Association, the output of aluminum plates and strips in China in 2021 were 13.35 million tons, of which 500,000 tons of printing plate substrates were produced. This indicates that the recycling scale of aluminum-based plates is considerable, but the recycling ratio of aluminum -based CTP plates is yet to be improved.

4 Prospects for Integrated Recycling and Reuse Technology for Aluminum Substrates of Spent CTP Plates

The integrated technology of recycling and reuse of aluminum substrate for spent CTP plates refers to a series of processes to separate, recycle and reprocess aluminum substrate and other materials (curing layers) from spent CTP plates into new functional materials. This improves the recycling efficiency of spent CTP plates, reduces costs and environmental impacts via a top-level design perspective, achieves the resourceful utilization of the recycled aluminum substrate, and promotes the transformation of the printing industry into a green circular economy. The key to its realization lies in sustainable material utilization design enhancement, spent material recycling device optimization and multi-material fine separation process advancement.

4.1 Sustainable material utilization design enhancement

Sustainable material utilization design is mainly embodied in sustainable product integration design and closed-loop recycling system design, the former requires a full understanding of the physical and chemical properties of materials based on innovative structure or functional product design, and the latter focuses on the

construction of the material recycling system under the reuse of the ecological carbon footprint planning. Current research status of sustainable product integration design of aluminum substrate shows that this field is gradually becoming a hotspot in the intersection of industrial design and material science. From the industrial design perspective, the surface microstructure design and three-dimensional modeling of aluminum substrates of spent CTP plates offer infinite possibilities for sustainable material utilization. The main processing requirements are concentrated on mechanical strength and surface properties needed for physical operations like cutting, engraving, or folding. For example, after the surface curing layers of aluminum substrate of CTP plates scrapped in the printing workshop are removed by mechanical grinding, the creases and cutting paths required for the forming of common items in the workshop can be creatively generated by using AI technology to further develop innovative applications such as the re-foldable mosquito coils holders, polygonal convenience trash cans and optical disk holders, as demonstrated in Figure 3.

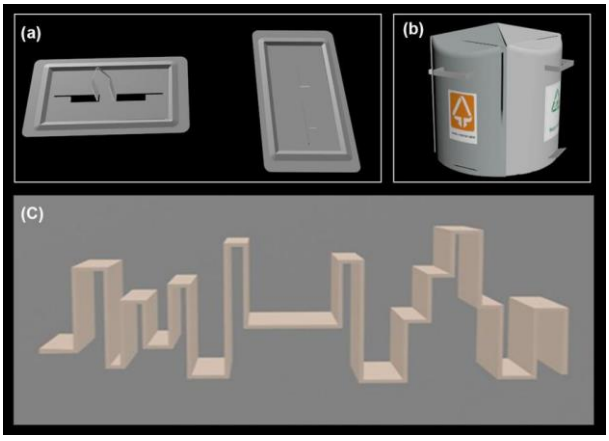

Figure 3 AI-generated creative cases for reuse of aluminum substrates: (a) Mosquito coil holders; (b) Trash cans; (c) Optical disk holders

The research focus of the closed-loop recycling system design is on how to efficiently build a complete circular chain from production to consumption to recycling, aiming to achieve efficient reuse of resources and minimize environmental impact through technological innovation, process optimization and policy support. In other words, it ensures that materials can be recycled and reprocessed many times throughout its entire life cycle, thus reducing resource consumption and waste generation, as well as promoting the low-carbon development of the functional use of spent materials. For example, Fujifilm has launched a closed-loop CTP plate recycling network to greatly reduce environmental loads and CO_2 emissions in the integrated recycling process of aluminum substrate of CTP plates, in cooperation with printing companies, newspaper publishers, aluminum recycling companies, alloy manufacturers, and roll manufacturing plants [24]. Thus, researchers can further explore how to minimize the environmental impact of aluminum substrates of CTP plates at all stages of design, fabrication, usage, and recycle and reuse.

4.2 Spent material recycling device optimization

In terms of the circulation environment, once the recycling path of spent materials has been determined, the recycling department adopts the spent material recycling device for processing and preparing the required physical and chemical properties for the next reuse step. Innovations in digital technology have led to more efficient recycling units, such as the thermal CTP plate recycling device, which improves the efficiency of the physical recycling of aluminum substrates by automating the guiding, leveling, auxiliary folding and flattening mechanisms [25]. Currently, innovative development of wasted material recycling facilities focuses on individual devices or complete production lines for catalytic cracking, catalytic hydrocracking, hydrocracking and component purification. BASF in Schwarzheide, Germany, established the first adjacent battery metal materials production and recycling center in Europe, including high-performance cathode active material production and battery recycling equipment [26]. This center is able to collect waste batteries and recover metal raw materials for the production of new battery materials, realizing the closed-loop recycling of battery metal materials. In recent years, the innovative research of recycling devices for aluminum-based waste materials have all relevant authorized invention patents, including aluminum chips recycling device, aluminum dregs recycling device, aluminum ash recycling device, aluminum foil recycling device and so on. In addition, the utilization of AI technology in wasted material recycling management greatly improves the fine separation of multiple materials between multi-process units. For example, AI vision-based rapid inspection devices can identify and reject real-time defects in recycled aluminum substrates [27], AI-controlled industrial robots can accurately classify and finely dismantle complex aluminum substrate products [28], and AI algorithm-based aluminum composition decontamination devices provide intelligent generation of refined and decontaminated material recipes [29].

4.3 Multi-material fine separation process advancement

The cured layers of graphic info on aluminum-based CTP plates are tightly bonded to the surface of the aluminum substrate, which makes the stripping process complex and difficult to remove completely. Judging from the material composition, the curing layers attached to the aluminum substrate of CTP plates are mainly the curing layers of photopolymer and residual ink co-mingled on the multi-layer sand mesh of the alumina, which are connected very densely. Traditional stripping

methods are not yet able to effectively remove the curing layers, while may cause scratches, deformation and other damages to the surface of aluminum substrate, affecting its closed-loop recycling value. In the grade preserving recycling process of aluminum substrate, the existing chemical stripping agents mainly include strong acid stripping agent, dry ink removal cleaning agent, pure solvent-based stripping agent, and eco-friendly stripping agent, among which the principle of efficient stripping of eco-friendly stripping agent, which is the most popular, needs to be further investigated. The development of stripping process with ultrasonic co-frequency technology [30] assisting eco-friendly organic surfactants will be the best green option, which is expected to break through the advanced waste-free process. However, in the degraded recycling process of aluminum substrate of CTP plates, many other non-aluminum components are mainly removed directly by physical stripping process, which in turn focuses on the reuse innovation of recycled aluminum. This method can reduce the reuse cost of recycled aluminum, although the amount of recycled aluminum is reduced to a certain extent, requiring a greater increase in novel high-value applications of recycled aluminum. For example, finely 3D printing aluminum powder for electron beam melt forming can be further 3D printed into high value-added personalized engineering components such as aluminum-based energy-containing components [31], automotive porous aluminum alloy cushion bumpers [32], and high-performance reflective aluminum mirrors [33]. If the expansion of the upgraded recycling process of aluminum substrate of CTP plates, the most urgent innovation lies in the fine control process of the chemical composition on the surface and internal of the aluminum substrate, which is not yet a mature industrialized application. As a result, solving the key materials, core devices and control software restricting the source reduction and harm reduction of waste materials will improve the green and intelligent level of the integrated equipment for recycling and utilization of aluminum substrate of CTP plates.

5 Conclusion

As a green plate material common to modern offset printing enterprises, the number of aluminum substrates of CTP plates for production needs and printing scraps in China is growing rapidly, which is inseparable from the research on the integrated technology and equipment for recycling and utilization in a safer, higher and green way. Starting from the management practice of spent aluminum substrates, this paper elaborates the plate production process, physical and chemical properties and recycling features of spent aluminum substrates of CTP plates, and further outlooks on the development challenges of the integrated recycling and reuse technology. It is worth noting that the high-value use of recycled scrap aluminum substrate requires further application of artificial intelligence technology and 3D printing technology, and the integrated new processes and materials required for the transformation of green printing under the national “Double Carbon” strategy have become more significant. Thus, this urgently requires a sufficient understanding of the green recycling path of multiple materials in parallel in the green printing flow, and further optimization of the refining and purification process of waste aluminum material, which is expected to break through the high-value reuse technology of the entire component of the aluminum substrate.

References

[1] Z. Pavlovic, S. Dedijer, N. Kasikovic, et al. Evaluation of effective models of offset CTP plate aluminium oxide surface roughness characterisation[J]. International Journal of Surface Science and Engineering, 2017, 11(5): 433-449.

[2] Verified Market Reports. CTP Technology Market Size, Global Trends | Forecast[R]. Verified Market Reports, 2023.

[3] Zhiyan Consulting. Research on the Prospect of the Chinese CTP Plate Industry and Competitor Analysis Report for 2022-2028[R]. Beijing: Zhiyan Consulting, 2022.

[4] Q.H. Yang, Y.X. Gao, J. Gao. Current Status and Future Development Trends of Offset Printing Plates[J]. Printing Technology, 2018 (10): 96-101.

[5] M.L. Zhou. Exploring Measures to Improve the Print Resistance of Environmentally Friendly Violet Laser CTP Plates[J]. Printing Magazine, 2022 (02): 69-72.

[6] J. Cao, Q.Y. Ma, P. Yang. Looking at CTP Technology Development from drupa 2016[J]. Printing Technology, 2016 (11): 14-16.

[7] J.Y. Yu, Y.L. Zhao. Exploration of Inkjet Plate Making and Its Printing Applicability[J]. Printing Technology, 2015 (09): 38-40.

[8] F. Chen, Z.W. Liu, Q.Y. Wang, et al. Analysis and Control Methods of Casting Defects in PS/CTP Plate Base Products by Continuous Casting[J]. Nonferrous Metal Processing, 2024, 53(02): 39-41.

[9] S. Yaghoubi, A. Piccininni, M. Seidi, et al. Multi-criteria optimization of the warm hydroforming process of an aluminum component based on the adaptive neuro-fuzzy inference system[J]. Journal of Manufacturing Processes, 2024 (132): 75-92.

[10] G.Z. Jia, Y.C. Huang, Y. Liu, et al. Effects of Cold Rolling Deformation and Baking Treatment on the Microstructure and Properties of CTP Aluminum Plates[J]. Materials Science and Engineering of Powder Metallurgy, 2018, 23(01): 54-62.

[11] Q.L. Huang. Process Research on Plate Shape Optimization for CTP Plate Base[J]. Light Alloy Processing Technology, 2016, 44(08): 35-38.

[12] L.Y. Shen, M. Zhu, B.H. Lang, et al. An Adaptive Detection Algorithm for Flaws on CTP Plates [J]. Journal of Changchun University of Science and Technology (Natural Science Edition), 2014, 37(06): 94-98.

[13] L.L. Liu, Z. Li, J.H. Zhong, et al. Review of Primary Recycling and Reuse of Aluminum Cans [J]. Food Industry, 2022, 43(09): 268-273.

[14] R.Y. Li, Y.W. Wang, B.J. Guo, et al. Research status of scrap aluminum recycling[J]. China Nonferrous Metallurgy, 2024, 53(4): 84-93.

[15] P.H. Liu, C.X. Ye, Q.R. Qian, et al. Research on accurate separation of aluminum-plastic composite packaging waste and reuse of its separated waste liquid[J]. Recyclable Resources and Circular Economy, 2023,16(05): 23-28.

[16] Tetra Pak. Finding the innovative approach: recycling PolyAl into filament for 3D printing [W/OL].Https://www.tetrapak.com/en-pl/insights/cases-articles/recycling-polyal-from-used-beverage-cartons-into-filament-for-3d. (Accessed date: 20th Nov. 2024)

[17] K.H. Gu, J.H. Chang, X.H. Mao, et al. Efficient separation of cathode materials and Al foils from spent lithium batteries with glycerol heating: A green and unconventional way[J]. Journal of Cleaner Production, 2022 (369):133-270.

[18] M.A.M. Alhefnawi, Energy budget in an educational building in KSA: The case of cladding with terracotta and aluminium[J]. Ain Shams Engineering Journal, 2021, 12(3): 3255-3261.

[19] O. Zaheer, G. Ingarao, A. Pirrotta, et al. Geometrical deviation of end-of-life parts as a consequence of reshaping by single point incremental forming[J]. International Journal of Advanced Manufacturing Technology, 2021, 115(5): 1579-1588.

[20] G. Ingarao, O. Zaheer, L. Fratini, Manufacturing processes as material and energy efficiency strategies enablers: The case of Single Point Incremental Forming to reshape end-of-life metal components[J]. CIRP Journal of Manufacturing Science and Technology, 2021 (32): 145-153.

[21] X.T. Li, H. Liu, J.C. You, et al. Back EVA recycling from c-Si photovoltaic module without damaging solar cell via laser irradiation followed by mechanical peeling[J]. Waste Management, 2022 (137): 312-318.

[22] D. Farioli, M. Fabrizio, E. Kaya, et al. Reshaping of thin steel parts by cold and warm flattening [J]. International Journal of Material Forming, 2023, 16(4): 35.

[23] J. Li. Key technology of reusing extrusion die for waste aluminum template[J]. Aluminum Processing, 2021 (4): 58-61.

[24] Fujifilm Corporation. Fujifilm Promotes an Innovative Offset Plate Recycling Program [W/OL]. Bisenet, 09-22-2011. https://bisenet.com/article/201109/105711.htm (Accessed date: 20th Nov. 2024)

[25] S.L. Meng, X. Meng. A Recycling Device for Thermosensitive CTP Plates[P]. Tianjin: CN201821505260.4, 2019-07-05.

[26] BASF. Battery Materials and Recycling Go Hand in Hand: BASF Opens Adjacent Battery Material Production and Recycling Center to Build a Closed-Loop Battery Value Chain in Europe[W/OL]. 2023 July 29. https://www.basf.com/cn/zh/media/news-releases/asia-pacific/ 2023 /07/p-23-251. (Accessed date: 20th Nov. 2024)

[27] R.F. Wei. Research on Surface Defect Identification Technology of Aluminum Profiles Based on Deep Learning[D]. Zhejiang University, 2019.

[28] X.Y. Zou, J.H. Huang, J.J. Huang. Artificial Intelligence Drives High-Quality Development of Aluminum Processing Products—A Case Study of the Aluminum Processing Industry[J]. Digitization user, 2021 (51): 79-81.

[29] J.F. Fatriansyah, R.K. Rizqillah, I. Suhariadi, et al. Composition-based aluminum alloy selection using an artificial neural network[J]. Modelling and Simulation in Materials Science and Engineering, 2023, 31(5): 55.

[30] Z.Q. Chen. Application of Ultrasonic Welding Machine in Printing CTP Plate Production Line[J]. Modern Manufacturing Technology and Equipment, 2017 (10): 136-137.

[31] J.H. Han, W.M. Jie, D.P. Chen, et al. Research Progress on 3D Printing of Aluminum-Based Energetic Materials[J]. Journal of Explosives and Propellants, 2023, 46(11): 937-949.

[32] Z. Tan. Research on 3D Printing of Porous Aluminum in Vehicle Collision Energy Absorption [J]. Farm Machinery Use and Maintenance, 2020 (11): 41-42.

[33] J.B. Cui, R.J. Zhao. Design and Manufacturing of High-Performance Reflective Aluminum Mirrors Using 3D Printing[J]. Integrated Circuit Applications, 2021, 38(07): 40-42.

Viser Technology Pte. Ltd.
Research and Application of Materials Science
DOI: 10.33142/rams.v6i2.14582

Research Article Open Access

Research Progress on Ionic Erosion of Steel-reinforced Concrete Structures under Marine Environments

Lei FAN[1, 2*], Jinhao ZHENG[1, 2], Chengtao WU[1, 2]

1. School of Civil Engineering and Architecture, Zhejiang University of Science & Technology, Hangzhou, Zhejiang, 310023 China
2. Zhejiang- Singapore Joint Laboratory for Urban Renewal and Future City, Hangzhou, Zhejiang, 310023, China

Corresponding Author: Lei FAN, E-mail: fanleigl@foxmail.com

Abstract

As one of the most widely used structural forms in the world, reinforced concrete structures have been widely used in various infrastructure construction. However, the corrosion of steel bars in concrete often leads to durability failure of reinforced concrete structures, leaving the structure unable to meet the requirements of design life. In reinforced concrete structures in marine environments, corrosion and degradation of steel bars caused by chloride ions is one of the important reasons for the durability failure of the structures. In this paper, the chloride ion erosion mechanism of concrete, steel bars and concrete-steel transition zone is introduced, the influence mechanism of different marine environmental factors on chloride ion erosion is clarified.

Keywords: Steel-Reinforced Concrete, Ionic erosion, Marine Environments, Transition Zone, Durability

1 Introduction

The ocean is the most extensive area on the earth's surface, with a total area of about 3.6×108 km^2, accounting for about 71% of the earth's surface area, containing rich mineral resources.

Seawater not only contains a variety of inorganic salts mainly NaCl, but also contains dissolved oxygen, particulate organic matter and humic substances including humic acid, etc., and the surface seawater is close to saturation with O_2 and CO_2, and the pH value is about 8.2, which is a corrosive electrolyte solution with a very complex composition. Chloride and sulfate ions in the marine environment infiltrate into the marine engineering from the outside through chemical potential energy and pressure drives, and these corrosive ions are transported to the surface of the steel bar through the pores and cracks in the concrete [1], by destroying the passivation film around the steel bar, the steel bar undergoes a chemical reaction, thereby reducing the service life of the marine project. With the new development period of marine engineering construction, there are more and more marine engineering applications such as cross-sea bridges, port wharves, island construction, submarine tunnels, offshore oil drilling platforms, and offshore floating buildings, and the lack of durability and structural damage caused by concrete cracking and steel corrosion has become an important problem of actual engineering failure.

Due to the increasing cost of repairing and updating offshore concrete structures, the cost of repairing reinforced concrete structures due to steel corrosion worldwide averages more than $100 billion per year [2], the world's loss due to steel corrosion accounts for 1%～2% of GDP [3]. It has accounted for the vast majority of the marine engineering construction budget of all countries in the world, therefore, the corrosion problem of the marine environment in the application of marine engineering, the development of new marine anti-corrosion technologies and new materials such as high-durability marine engineering concrete, high-corrosion resistant reinforcement, and heavy anti-corrosion coating is particularly important.

2 Marine Ion Erosion Mechanism in Concrete

Cl- erosion is often considered to be the main cause of the deterioration of reinforced concrete structures in chloride salt environments [4-5]. When the Cl- concentration is greater than a certain critical value, the reinforced concrete structure is easily damaged due to steel corrosion [6], the durability of the structure is reduced, which in turn leads to a shortened service life of the concrete structure [7-8].

2.1 Ionic erosion process in concrete

In 1997, Hooton [9] et al. pointed out that when concrete is exposed to chloride salts, there are at least six

Received on September 24, 2024; Accepted on October 22, 2024

transport mechanisms for chloride ions to enter the concrete: diffusion, capillary action, osmosis, adsorption, binding and diffusion, etc.

The erosion process of chloride ions in the marine environment is elaborated, including the permeation mechanism of chloride ions on the surface and inside of different materials (e.g., concrete, steel, alloys, etc.).

2.2 Diffusion

Saturated concrete is composed of liquid and solid phases, and the transmission speed of chloride ions in the liquid phase is much faster than that in the solid phase under the action of the concentration gradient, so the diffusion of chloride ions in the solid phase of concrete is negligible. When the solid phase blocks the transport path of chloride ions, the chloride ions continue to diffuse forward bypassing the solid phase, rather than directly diffusing from the solid phase, so the diffusion rate of chloride ions in saturated concrete is mainly determined by the diffusion rate and pore structure of chloride ions in the pore solution [10].

When the concrete is saturated, diffusion is the most important way for chloride ions to be transported to the surface of the rebar, and the law of erosion follows Fick's second law approximately [11]. Fick's first and second laws are derived from the Fourier heat conduction equation [12]. In 1970, Collepardi [13] et al. considering the actual situation in the concrete Cl-Fick's second law was first introduced to describe Cl in concrete in the diffusion process:

$$\frac{\partial C(x,t)}{\partial t} = D\frac{\partial^2 C(x,t)}{\partial x^2} \tag{1}$$

Where x is expressed as position. t represents time and D is chloride diffusion coefficient. $C(x,t)$ is the concentration of chloride ions at the x position at the t moment. If the initial conditions $C(0,t)=C_b$, $C(\infty,t)=C_0$ are given, the initial conditions $C(x,0)=C_0$ are set, and if the chloride diffusion coefficient is not a function of time and space, then the solution of the chloride ion transport equation can be written as:

$$C(x,t) = C_0 + (C_b - C_0)[1 - erf(\frac{x}{2\sqrt{Dt}})] \tag{2}$$

where erf is the error function. As can be seen from Equation (2), the concentration of chloride ions at this time is related to the chloride concentration at the initial moment in the concrete.

2.3 Convection

Convection refers to the mass transfer phenomenon caused by the movement of a fluid that drives the molecules or ions dissolved in the fluid. When the reinforced concrete structure is in an unsaturated state, the liquid containing chloride ions from the outside penetrates into the concrete pore structure, and the chloride ions will be convection. The flux of convection can be expressed by the following relation [14]:

$$N_{i,conv} = c_i u \tag{3}$$

Among them, c_i is the concentration of chloride ions. u is the flow velocity of seawater in the reinforced concrete structure, and the flux vector of chloride ion convection is positively correlated with the flow velocity of seawater, so the velocity of chloride ion convection is the same as the flow velocity of seawater. If you need to consider the change in chloride concentration caused by convection at a point on the reinforced concrete structure, you can bring Equation (3) into the mass continuity equation to solve:

$$(\frac{\partial c_i}{\partial t})_{conv} = -\nabla \cdot N_{i,conv} = -c_i \nabla \cdot u - u \cdot \nabla c_i \tag{4}$$

Considering that seawater is an incompressible fluid, the mass of the entire seawater is conserved, so the inclusion term ($\nabla \cdot u$) is zero. Therefore, there is only a difference in the concentration of chloride ions, the concentration of chloride ions in the lining structure is caused by convection change, so Equation (4) can be rewritten as:

$$(\frac{\partial c_i}{\partial t})_{conv} = -u \cdot \nabla c_i \tag{5}$$

The convection zone usually occurs in the area where the reinforced concrete structure meets the external environment, and the thickness of this area is usually 0～20mm. When chloride ions enter the area 20 mm away from the concrete surface, the chloride ion transport mode is mainly diffusion.

2.4 Capillary water absorption

When a liquid comes into contact with a solid, the surface forms an interfacial energy, which is caused by the difference between the attraction of the liquid to the surface molecules and the attraction of the solid to the surface molecules, and this difference can draw the water in the pores to a certain height and form a meniscus in the pores. This transport mechanism mainly occurs in the shallow protective layer, which generally cannot transport chloride ions to the surface of the reinforcement in reinforced concrete, unless the quality of the concrete is very poor and the thickness of the protective layer is very small. However, this mechanism allows for rapid chloride ion transfer to a certain depth of the protective layer, which reduces the diffusion distance of chloride ions to the surface of the rebar [15].

2.5 Thermal migration

Ions or molecules move faster in a hot environment than in a cold environment. If the saturated concrete contains a uniform concentration of chloride ions, and when a part of the concrete is heated, the chloride ions will migrate from the high temperature to the low temperature part, and migrate from the outside to the inside of the

concrete under the action of temperature difference.

2.6 Electromigration

After chloride ions penetrate into the concrete structure of offshore engineering, it will cause the corrosion of the steel bar and produce galvanic cells. This corrosion phenomenon produces two types of galvanic cells: microcells and galvanic cells [16-17]. A micro-battery is a corroded cell that provides both the anode and the cathode on the same rebar, the area where the anode is not rusted, and the cathode is an oxide of iron on the rebar. Macro-battery refers to a corroded battery with different steel bars providing an anode and a cathode respectively, the anode is the unrusted steel bar, and the cathode is the corroded part of the steel bar that has been corroded. Since both microcells and macro-batteries generate an electric field, the chloride ions in the seawater that invade the concrete under the action of the electric field will move towards the cathode, and the electromigration process can be described by the Nernst-Planck equation [18]:

$$J = D\frac{z_i FE}{RT}C \tag{6}$$

Among them, J is the flow rate of chloride ions in the process of internal electromigration of concrete, D is the diffusion coefficient of chloride ions, F is Faraday's constant 96485.33 C/mol. z_i is the valency of chloride ions, and R is the molar constant of gas 8.314. T represents the internal temperature of concrete. E indicates the electric field strength of the electric current, C is the concentration of chloride ions.

3 Chloride Ion Erosion Process of Steel bars

3.1 Passivation film destruction

Calcium silicate in Portland cement, a concrete component, produces $Ca(OH)_2$ hydration, so that the pore fluid in the concrete presents a high alkalinity, the pH value is between 12.5～13.5, and the OH is in the pore fluid. It is adsorbed on the surface of the steel bar and formed by the reaction with Fe oxide film, which is complete and dense, effectively protects the steel bar from corrosion. The high activity and small ionic radius of Cl^- make it dominant in the competitive adsorption with OH^-, and OH^- preferentially combines with Fe, and Cl^- can penetrate the defects of passive film of steel bar. When the amount is large enough, that is, the pH value of the steel bar surface will drop rapidly at the same time, and the dissolution of the passivation film will be intensified. When a certain critical value is reached, this value is usually Cl^-/OH^-～0.6, the passivation film is activated and begins to dissolve, at which point if there is water and oxygen around the reinforcement, the reinforcement begins to corrode [19]. In this level of erosion mechanism, the effect of Cl^- is mainly manifested in competitive adsorption.

3.2 Formation of corrosive batteries

With the dissolution of the passivation film in some areas of the steel bar surface, the iron matrix is exposed, because the activity of the iron matrix is higher, and the activity of the passivation film coverage area is low, so the surface of the steel bar forms a pattern of large cathode and small anode. The iron matrix is a small anode, the passivation film coverage area is a large cathode, and the concrete pore fluid around the steel bar contains a large number of ions. It can be used as an electrolyte, and because there is an electric potential difference between the large cathode and the small anode, the corrosion battery is formed, accompanied by charge transfer and material transfer, and the corrosion current is generated [20]. The dissolution of the passivation film is often in a small and variable area, so the corrosion of the steel bar caused by the erosion of this layer is often pitting, but the development rate is very fast.

3.3 Chloride ion depolarization

After contributing to the formation of corroded cells, Cl- further accelerates the corroded cell reaction by removing or slowing down anodic polarization. In the corrosion cell reaction, anodizing generates Fe^{2+}, which combines with nearby Cl^- to form $FeCl_2$, which is soluble and spreads outward with the concrete pore liquid, and OH will be encountered in the process-, $FeCl_2$ with OH^-. The reaction produces poorly soluble $Fe(OH)_2$, $Fe(OH)_2$ with H_2O, O_2. Continue the reaction generation of $Fe(OH)_3$, Fe_2O_3 and Fe_3O_4, whereas Cl^- is released and returns to the vicinity of the anode again to combine with Fe^{2+}, and the cycle repeats [21].

In this process, Cl-It plays the role of catalysis and transport, so that the Fe2+ near the anode will not accumulate, resulting in polarization, which will affect the reaction rate of the battery, in fact, only a small amount of Cl- can accelerate the corrosion reaction repeatedly, the following is the main chemical equation of the cathode and anode reaction [22]:

Anode reaction: $Fe \rightarrow Fe^{2+} + 2e^-$

Cathodic reaction: $2H_2O + O_2 + 4e^- \rightarrow 4OH^-$

Corrosion products:

$$Fe^{2+} + 2Cl^- + 2H_2O \rightarrow Fe(OH)_2 + 2HCl$$
$$4Fe(OH)_2 + 2H_2O + O_2 \rightarrow 4Fe(OH)_3$$
$$2Fe(OH)_3 \rightarrow Fe_2O_3 + 3H_2O$$
$$6Fe(OH)_2 + O_2 \rightarrow 2Fe_3O_4 + 6H_2O$$

3.4 Conductivity

Electrochemical reactions are mainly manifested in charge transfer and species transfer, so the ion pathway in the electrolyte is particularly important. The presence of the concrete porosity is able to increase the conductivity of the concrete pore fluid, reduce the ohmic

resistance of the electrochemical cathodic and cathodic reactions. In addition, the presence of Ca^{2+}, K^{+}, etc., further increases the material transport rate and accelerates the electrochemical reaction [23].

4 Reinforcement-concrete Transition Zone

4.1 Formation of a reinforcing steel-concrete transition zone

The structure of the rebar-concrete interface is complex, including the C-S-H gel layer、$Ca(OH)_2$. Deposition layer, corrosion product layer, oxide scale on the surface of steel bar, bubbles and voids in the water secretion area, etc. The bond-concrete interface transition zone can be regarded as the third phase of reinforced concrete materials, and its formation and evolution mechanism is very complex and affected by many factors. YS Ji found [24] that there is a special area of weakness between the steel surface and the cement slurry, that is, the transition zone of the reinforcement-concrete interface. They believe that the "wall effect" is the main reason for the formation of the reinforcement-concrete interface transition zone, that is, a layer of water film will be formed on the surface of the reinforcement, and the cement concentration is close to zero at the surface of the reinforcement and increases with the increase of the distance from the reinforcement surface, so the composition and structure of the hydration products in the reinforcement-concrete interface transition zone are different from the matrix.

In addition, there are studies show that [25-26] the bottom of the horizontally arranged steel bar is prone to form a water-draining area during the concrete pouring process, and after the cement is hydrated, the area may have defects such as holes. During the pouring and vibrating of the new concrete, gravity makes the aggregate sink, and the buoyancy makes the bubbles and slurry move upward, and the horizontal steel bars hinder the movement of the bubbles and the slurry, causing them to gather at the bottom of the steel bar, and eventually form holes and cavities [27-28]. The size of the holes and cavities is related to the height of the concrete under the reinforcement at the time of pouring.

4.2 Structural characteristics of the reinforcing steel-concrete transition zone

The pore structure of the reinforcing steel-concrete interface transition zone is affected by the direction of the reinforcement [29]. The structure of the transition zone between the reinforcement and the upper part of the horizontal reinforcement is dense, but the structure of the interface transition zone at the lower part of the reinforcement is more complex, and the structure is composed of the water drainage zone, the floating bubble hole and the cement slurry porous layer [30].

Kenny et al [31] and Horne et al [32] indicated that the horizontal arrangement of the reinforcement will hinder the floating process of air bubbles in the concrete, and the bubbles will converge at the bottom of the reinforcement, resulting in the formation of a water secretion zone on the lower side of the reinforcement. It makes the porosity in the lower interface of the reinforcement significantly higher than that of the upper interface and the vertical reinforcement interface. Zhang et al [33] through the analysis of backscattered electron images, it is found that the porosity of the area under the reinforcement is obviously higher than that of the concrete matrix, and the area with large porosity is mainly concentrated in the interface transition zone. The area with medium porosity and low porosity mainly appears at the location of mortar and coarse aggregate.

The transport mechanism of chloride ions in concrete is complex, and the capillary pore structure has a significant effect on chloride ion transport in the porous system of hardened concrete [34], of which the pores that have the greatest impact on permeability are concentrated in the 10 nm～10 μm range, but overall, the rate of migration in the concrete matrix is positively correlated with the total porosity of the concrete [35].

5 Factors Influencing Chloride Ion Transport Characteristics

5.1 Temperature

Temperature is one of the important factors affecting the diffusion of chloride ions in the salt spray environment. The increase of ambient temperature will accelerate the thermal movement of chloride ions, cause the acceleration of the chemical reaction rate of cementitious materials, reduce the physical adsorption capacity of hydration products to chloride ions, and improve their chemical binding effect on chloride ions [36-38].

The increase of temperature will accelerate the evaporation of water in concrete, accelerate the crystallization and precipitation of chloride ions in the pore solution, and promote the cracking of concrete. It provides a new channel for chloride ion transport [39].

The Arrhenius formula was used to analyze the effect of temperature on the chloride diffusion coefficient in concrete, and it was found that the apparent chloride diffusion coefficient increased significantly with the increase of temperature [40]. The effect of increasing temperature on chloride ion transport has a dual effect: first, high temperature will reduce the pore water saturation and accelerate the hydration of cement, reduce the porosity of the matrix, thereby slowing down the erosion of chloride ions; The second is the decomposition of Friedel's salt will release the adsorbed bound chloride ions, increase the concentration of free chloride ions, change its activation energy. The increase of the temperature will accelerate the water transport in the concrete, thereby accelerating the convection rate of chloride ions [41-43].

5.2 Wind speed

The effect of wind speed on chloride ion transport is mainly reflected in the first stage of erosion, where ocean aerosols in the atmosphere are transported inland by the sea breeze and settle at a certain distance [44-45]. Wind speed can affect the concentration of chloride ions in the atmosphere by affecting the distance and amount of ocean aerosols transported [46]. The increase in the concentration of chloride ions in the atmosphere will accelerate the deposition of chloride ions on the surface of concrete, creating more favorable conditions for the transport of chloride ions to the interior of concrete. Some scholars believe that when the wind speed exceeds 3 m/s, the concentration of chloride ions in the air will rise rapidly [47-48]. Secondly, wind speed increases the humidity gradient inside the concrete [49], increases the water migration rate, and accelerates the convection of chloride ions. Gustafsson et al [50] found that the chloride ion deposition rate under different wind speed conditions was measured by chloride ion detector, and it was found that the chloride ion deposition rate had a good correlation with the exponential wind speed, and the correlation coefficient at each position was above 0.99. In general, the increase of wind speed will accelerate the deposition of chloride ions on the surface of concrete, intensify the capillary adsorption of the matrix, increase the transmission rate of chloride ions, and adversely affect the chloride ion erosion resistance of concrete.

5.3 Distance from shore

Chloride ions in the atmosphere settle due to gravity and the blocking of trees and mountains as they move inland, causing chloride concentrations to decrease farther away from the coastline [51]. The transport process of chloride ions inside the concrete is closely related to the amount of chloride ions deposited. Meira et al [52] found that the quantitative relationship between chloride ion deposition and chloride ion content in concrete at different distances from the coast was established, and a nonlinear relationship between the two was determined. The Civil Engineering Society of Japan has established the value of chloride ion concentration on the surface of concrete in coastal atmospheric areas [53]. The chloride ion concentration on the concrete surface in the coastal atmosphere is shown in Table 1.

Table 1 Concentration of chloride ion on concrete surface in coastal atmospheric area [53]

Distance from coast line/km	Chloride ion concentration(mass friction)/%
Near the coast line	0.450
0.10	0.225
0.25	0.150
0.50	0.100
1.00	0.075

In general, the amount of salt spray in the atmosphere is closely related to the distance from the coastline, and the reduction of the salt spray content weakens the erosive effect of chloride ions, that is, the farther away from the coastline, the less susceptible the reinforced concrete structure is to the erosion of chloride ions.

5.4 Exposure time

In general, the erosive effect of chloride ions on concrete increases with the increase of exposure time. With the increase of exposure time, the amount of chloride ions deposited on the surface of the concrete gradually increases, and the chloride ions transported to the concrete through capillary adsorption and diffusion also increase until the dynamic equilibrium is reached. The study shows that with the increase of the service life of reinforced concrete structures, the chloride ion erosion depth of reinforced concrete structures also increases, and the chloride ion erosion depth of concrete structures in 60 years of service is 1.5 times that of 10 years of service [54]. In order to explore the time-varying characteristics of chloride ion transport in self-compacting concrete, a five-month real-sea exposure test was carried out. The results show [55] that the longer the exposure time, the higher the concentration of chloride ions within a certain erosion depth, and the chloride concentration tends to be consistent beyond this depth. The diffusion coefficient of chloride ions is negatively correlated with time.

5.5 Cement composition

5.5.1 C3A and C4AF

In the case of internal chloride ions, Racheeduzzafar et al [56] found that the water-soluble chloride ion decreased significantly with the increase of C_3A content. In addition, they soaked concrete, a cement formulation containing 9% and 14% C_3A, in a chloride salt solution, which was confirmed by X-ray diffraction analysis Formation of salts. Blunk et al [57] found that the pure C_3A-gypsum mixture and ordinary cement and C_3S slurry were soaked in chloride salt solutions of different concentrations, and it was found that the amount of chloride ions adsorbed by the C_3A-gypsum mixture was greater than that of the other two slurries. By soaking ordinary cement slurry and sulfate-resistant cement slurry in a 20g/l NaCl solution, Arya et al [58] found that the amount of chloride adsorbed by sulfate-resistant cement was much lower than that of ordinary cement slurry because of the C_3A of sulfate-resistant cement. Some of the results of studies on the internal chloride ions on the surface [59-60], The higher the C_3A content, the greater the chloride ion adsorption.

Chloride ions and C_3A and C_4AF can undergo chemical reactions to form Friedel's salts and their analogues. Therefore, the content of C_3A and C_4AF in cement determines the chemical adsorption of chloride ions. Friedel's salts may be produced by the direct

reaction of C_3A and $CaCl_2$. When chloride salts taste sodium chloride, the reaction equation is as follows [61]:

$$Ca(OH)_2 + 2NaCl = CaCl_2 + 2Na^+ + 2OH^- \quad (7)$$

$$C_3A + CaCl_2 + 10H_2O \rightarrow C_3A \cdot CaCl_2 \quad (8)$$

According to Suryavanshi et al [62] study, Friedel's salts and their analogues can be formed by two different mechanisms: the adsorption mechanism and the ion exchange mechanism. In the adsorption mechanism, the formation of Friedel's salt is to adsorb chloride ions in pore solution through the interlayer ($[Ca_2Al(OH)_6 \cdot 2H_2O]^+$) of AFm phase to achieve electrical neutrality. The mechanism of ion exchange is that chloride ions replace hydroxyl ions between the layers of AFm hydration phase (C_4AH_{13}) to form Friedel's salt, which can be expressed by the following formula: $R-OH^- + Na^+ + Cl^- \rightarrow R-Cl^- + Na^+ + OH^-$. Where R is $[Ca_2Al(OH)_6 \cdot nH_2O]^+$.

When Friedel's salt is formed by adsorption mechanism, sodium ions equivalent to chloride ions are also adsorbed from the pore solution to maintain the electrical neutrality of the pore solution. When Friedel's salt is formed by ion exchange mechanism, some hydroxyl ions are released into the pore solution, which increases the PH value of the pore solution. It is generally believed that the adsorption of chloride ions increases with the increase of the aluminum phase, and in the case of carbonization or sulfate ion intrusion, the chemisorption is reversible[63].

5.5.2 C3S and C2S

C-S-H gel is the main hydration product of cement, which determines the physical adsorption of chloride ions. Physical adsorption is due to the adsorption of chloride ions by C-S-H gels.

Ramachandran et al considered [64] that chloride ions in C-S-H are classified into three categories: chemical adsorption on the surface of hydrated calcium silicate; adsorption in the interlayer of C-S-H; It is tightly adsorbed in the molecules of C-S-H. The higher the content of C_3S and C_2S, the higher the content of C-S-H, and the higher the content of chloride ions in physical adsorption. Tang et al [65] found that the chloride ion adsorption capacity of ordinary Portland cement concrete depends entirely on the content of C-S-H, and has no relationship with the water-cement ratio and aggregate content. Beaudoin et al [66] believed that the chloride adsorption capacity of C-S-H depends on its calcium-silicon ratio C/S, and that a low calcium-silicon ratio may lead to a low adsorption capacity. However, by incorporating chloride ions in the Alite phase, Lambert et al [67] found the C-S-H phase is thought to adsorb only a very small amount of chloride ions.

C_3A and C_4AF controlled the chemisorption of chloride ions, while C_3S and C_2S determined the physical adsorption of chloride ions. By soaking the pure monomer compounds C_3A, C_4AF, C_3S and C_2S in chloride ion solution, Zibara [61] found that C_3A is an important influencing factor for chloride ion adsorption: in the high concentration range (1.0-3.0 mol/l), C_3A content is a good indicator of the chloride ion adsorption capacity of cement; In the low concentration range (0.1 mol/l), the C_3A content is no longer a good adsorption capacity of cement, but only an indicator. The adsorption capacity of C_4AF for chloride ions is about one-third of that of C_3A, and the contribution of C_3S to chloride adsorption is between 25% and 50%.

5.6 Marine conditions

In the marine environment, according to the location of the concrete structure, the concrete structure can be divided into underwater zone, tidal range zone, splash zone and atmospheric zone. The chloride ion transport mechanism in concrete in different areas is different [68].

(1) The underwater zone refers to the substructure completely submerged in seawater, the concrete in this area is in a saturated state. There is no humidity gradient, and the chloride ion transport mechanism is mainly diffusion caused by the difference of chloride ion concentration inside and outside the concrete [69].

(2) The tidal range zone refers to the structural part within the range of the elevation of the tide water level, which is subjected to the alternating dry and wet environment, and there is chloride ion concentration gradient, humidity gradient, concrete pore surface tension, etc. inside the concrete, so its chloride ion transport mechanism is the coupling of various mechanisms such as diffusion, unsaturated seepage and capillary absorption [69].

(3) The splash zone refers to the structural part near the high tide level that is impacted by the splash of waves, and this area is also affected by the alternating dry and wet environment, and the chloride ion transport mechanism is similar to that of the tidal range zone.

(4) The atmospheric zone refers to the superstructure that does not come into contact with seawater, and this area is mainly through the accumulation of chloride ions in the air on the surface of concrete, and then transport inward under the concentration gradient, and its main transport mechanism is diffusion. Among them, the tidal range area and splash chloride ion in the alternating dry and wet environment have the fastest transmission rate and the most serious corrosion.

5.7 PH value of concrete porosity

Back in the 60s of the 20th century, Venu, etc [70] proposed that hydroxide ion is one of the important factors to inhibit the corrosion of steel bars caused by chloride ions. Ghods [71], Li and Sagues [72] proposed that the higher the pH value of the concrete pore fluid, the greater the critical chloride ion concentration. Tan et al. [73] studied the inhibition of carbonate and bicarbonate on the corrosion of steel bars by using the simulated solution of concrete pore fluid. Figueira et al [74] proposed that when the pore fluid pH decreases from 13.5 to 11.6, the corrosion

resistance of the steel bar will gradually decrease. The effect of pH on the critical chloride concentration was analyzed by concrete pore fluid simulant by Figueira [75].

6 Conclusion and Prospect

The deterioration mechanism of reinforced concrete structures in the marine environment and the analysis of their time-varying reliability are one of the important topics to be solved in engineering. In this paper, we introduce the mainstream physical experimental research methods in the academic circles based on the chloride ion transport mechanism, and comprehensively evaluate the advantages and disadvantages of each interface optimization method based on the influence of various factors on ion erosion in the marine environment. Therefore, future research can seek breakthroughs in the following several areas to advance the service life of marine engineering.

The simulation method of steel corrosion process in concrete still needs to be further explored and improved. In all physical experiments, the use of reasonable test methods is an important prerequisite to ensure the correctness of the research results. Because chloride ions enter the concrete slowly, it takes years or decades to reach the surface of the rebar and accumulate to a certain point where the rebar begins to corrode. Therefore, scholars often use accelerated test methods to simulate the corrosion process of steel bars, and accelerated tests are often different from the actual situation. It is still worth exploring the relationship between the results of laboratory tests and the results of field tests.

In actual marine engineering, reinforced concrete structures mostly work under certain loads, and at present, a series of durability studies of concrete are mostly carried out on the basis of the non-load state, which has certain limitations and has a certain gap with the actual concrete engineering. In the future, the research on the durability of concrete under various environmental factors under stress should be strengthened and expanded, so that the research results are closer to engineering practice.

Acknowledgments: This work were supported by Natural Science Foundation of Zhejiang Province (LQ23E080003), a Doctoral program of Zhejiang University of science and technology (F701104L08) and The Special Fund Project of Zhejiang University of Science and Technology's Basic Scientific Research Business Expenses in 2023 (2023QN016).

Conflict of interest: No potential conflict of interest was reported by the authors.

References

[1] L. G. Zheng, H. Y. Yang. Effect of organic rust inhibitors on the corrosion behaviour of steel reinforcement in concrete specimens immersed in saturated NaCl solution [J]. ACTA PHYSICO-CHIMICA SINICA, 2010,26(09):2354-2360.

[2] C. Q. Li, R. E. Melchers. Time-dependent risk assessment of structural deterioration caused by reinforcement corrosion[J]. ACI STRUCT J, 2005,102(5):754.

[3] J. X. Gong, G. F. Zhao. Advances in the study of durability of reinforced concrete structures[J]. INDUSTRY BUILDING, 2000,30(5): 1-5.

[4] Y. P. Song, L. Y. Song, G. F. Zhao. Factors affecting corrosion and approaches for improving durability of ocean reinforced concrete structures[J]. OCEAN ENG, 2004,31(5/6):779-789.

[5] X. Shi, N. Xie, K. Fortune, et al. Durability of steel reinforced concrete in chloride environments: An overview[J]. CONSTR BUILD MATER, 2012(30):125-138.

[6] A. Pachón-Montano, J. Sánchez-Montero, C. Andrade, et al. Threshold concentration of chlorides in concrete for stainless steel reinforcement: Classic austenitic and new duplex stainless steel[J]. CONSTR BUILD MATER, 2018(186):495-502.

[7] H. W. Song, H. B. Shim, A. Petcherdchoo, et al. Service life prediction of repaired concrete structures under chloride environment using finite difference method[J]. CEMENT CONCRETE COMP, 2009,31(2):120-127.

[8] H. Yu, B. Da, H. Ma, et al. Service life prediction of coral aggregate concrete structure under island reef environment[J]. CONSTR BUILD MATER, 2020(246):118390.

[9] R. D. HOOTON, P. F. MCGRATH. Issues related to recent developments in service life specifications for concrete structures [C].Saint Remy Les Chev reuse: RILEM, 1997.

[10] Q. Yuan. Basic research on experimental methods for chloride transport in cementitious materials[D]. Central South University, 2009.

[11] Y. Gao, J. Zhang, S. Zhang, et al. Probability distribution of convection zone depth of chloride in concrete in a marine tidal environment[J]. CONSTR BUILD MATER, 2017(140): 485-495.

[12] J. Crack. The mathematics of diffusion, 2nd ed [D]. London: Oxford Univ. Press, 1975.

[13] M. Collepardi, A. Marcialis, R. Turriziani. Penetration of chloride ions into cement pastes and concretes[J]. J AM CERAM SOC, 1972,55(10):534-535.

[14] L. Tang, J. Gulikers. On the mathematics of time-dependent apparent chloride diffusion coefficient in concrete[J]. CEMENT CONCRETE RES, 2007,37(4):589-595.

[15] Martın-Pérez, Beatriz. Service life modelling of RC highway structures exposed to chlorides[D]. Ontario: University of Toronto, 1995.

[16] J. Li, J. Xiong, Z. Fan, et al. Mechanistic study of macrocell effect on corrosion initiation and propagation of reinforcement in submarine immersed tunnel[J]. CEMENT CONCRETE COMP, 2023(136):104890.

[17] J. Němeček, J. Kruis, T. Koudelka, et al. Simulation of chloride migration in reinforced concrete[J]. APPL MATH COMPUT, 2018(319):575-585.

[18] H. Chang. Chloride binding capacity of pastes influenced by carbonation under three conditions[J]. CEMENT CONCRETE COMP, 2017(84):1-9.

[19] P. Garcés, E. Saura, C. A. Zornoza. Influence of pH on the nitrite corrosion inhibition of reinforcing steel in simulated concrete pore solution[J]. CORROS SCI, 2011,53(12):10-15.
[20] J. Wei, J. H Dong, W. Ke. Corrosion resistant performance of a chemical quenched rebar in concrete[J]. CONSTR BUILD MATER, 2010,25(3):22-25.
[21] Sun Yisheng. Non-destructive quantitative detection test of internal reinforcement corrosion of bridge based on two-electrode potential by transient electromagnetic imaging[D]. Chongqing: Chongqing Jiaotong University, 2013.
[22] M. James, Gaidis. Chemistry of corrosion inhibitors[J]. CEMENT CONCRETE COMP, 2004,26(3):30-33.
[23] P. Ghods, O. B. Isgor, G. McRae, et al. The effect of concrete pore solution composition on the quality of passive oxide films on black steel reinforcement[J]. CEMENT CONCRETE COMP, 2008,31(1):15-18.
[24] Y. S. Ji, W. Si, M. Song, et al. Analysis of corrosion layer development and fine structure of steel reinforcement in concrete[J]. Journal of Building Structures, 2009,30(S2):303-308.
[25] T. U. Mohammed, H. Hamada, A. Hasnat, et al. Corrosion of steel bars in concrete with the variation of microstructure of steel-concrete interface[J]. J ADV CONCR TECHNOL, 2015,13(4):230-240.
[26] A. Nasser, A. Clément, S. Laurens, et al. Influence of steel–concrete interface condition on galvanic corrosion currents in carbonated concrete[J]. CORROS SCI, 2010,52(9):2878-2890.
[27] L. Shen, L. Struble, D. Lange. Modeling dynamic segregation of self-consolidating concrete[J]. ACI MATER J, 2009,106(4):375.
[28] L. Shen, L. Struble, D. Lange. Modeling static segregation of self-consolidating concrete[J]. ACI MATER J, 2009,106(4):367.
[29] Y. Cai, W. L. Zhang, L. W. Yu, et al. Characteristics of the steel-concrete interface and their effect on the corrosion of steel bars in concrete[J]. CONSTR BUILD MATER, 2020(253):119162.
[30] U. M. Angst, M. R. Geiker, A. Michel, et al. The steel-concrete interface[J]. MATER STRUCT, 2017,50(2):143-167.
[31] A. Kenny, A. Katz. Statistical relationship between mix properties and the interfacial transition zone around embedded rebar[J]. CEMENT CONCRETE COMP, 2015,(60):82-91.
[32] A. T. Horne, I. G. Richardson, R. M. D. Brydson. Quantitative analysis of the microstructure of interfaces in steel reinforced concrete[J]. CEMENT CONCRETE RES, 2007,37(12):1613-1623.
[33] Zhang Zhidong, Angst Ueli, Michel Alexander, Jensen Mads A. An image-based local homogenization method to model mass transport at the steel-concrete interface[C]. Leeds: Sixth International Conference on the Durability of Concrete Structures, 2018.
[34] D. Manmohan, P. K. Mehta. Study on blended portland cements containing santirin earth[J]. CEMENT CONCRETE RES, 1981,11(4):575-579.
[35] Y. Sakai. Relationship between pore structure and chloride diffusion in cementitious materials[J]. CONSTR BUILD MATER, 2019,229:116868.
[36] R. ZHAO, Z. Q. JIN, J. R. CAO, et al. Numercial simulation of chloride ions transportation considering temperature and humidity in marine environment. The Ocean Engineering, 2018,36(1):99-106.
[37] J. O. UKPATA, P. A. M. BASHEER, L BLACK. Slag hydration and chloride binding in slag cements exposed to a combined chloride-sulphate solution[J]. CONSTR BUILD MATER, 2019(195):238-248.
[38] D. K. PANESAR, S. E. CHIDIAC. Effect of cold temperature on the chloride-binding capacity of cement[J]. J COLD REG ENG, 2011,25(4):133-144.
[39] W. SHAO, D. D SHI, J. P. LI. Effect of environment temperature on chloride diffusion in RC pipe piles[J]. Journal of Civil and Environmental Engineering, 2019,41(2):12-19.
[40] H. S. SO, S. H. CHOI, K. S. SEO, et al. The properties of chloride ion diffusion of concrete under high temperature conditions, with implications for the storage of spent nuclear fuel in concrete casks[J]. KSCE J CIV ENG, 2014,18(7):2227-2233.
[41] M. Isteita, Y. P. Xi. The effect of temperature variation on chloride penetration in concrete[J]. CONSTR BUILD MATER, 2017(156):73-82.
[42] M. Zhou, J. C. Liao, L. An. Effect of multiple environmental factors on the adhesion and diffusion behaviors of chlorides in a bridge with coastal exposure:long-term experimental study[J]. J BRIDGE ENG, 2020,25(10):04020081.
[43] B. Chen, R. Ghani, A. Azaqpur. Exposure duration and sub-zero temperature effects on concrete chloride diffusion decay index and binding[J]. CONSTR BUILD MATER, 2021(313):125368.
[44] N. D. Pham, Y. Kuriyama, N. Y. Kasai, et al. A new analysis of wind on chloride deposition for long-term aerosol chloride deposition monitoring with weekly sampling frequency[J]. ATMOS ENVIRON, 2019(198):46-54.
[45] W. Bruch, J. Piazzola, H. Branger, et al. Sea-spray-generation dependence on wind and wave combinations:a laboratory study[J]. BOUND-LAY METEOROL, 2021,180(3):477-505.
[46] M. A. Thomas, A. Devasthale, M. Kahnert. Marine aerosol properties over the Southern Ocean in relation to the wintertime meteorological conditions[J]. ATMOS CHEM PHYS, 2022,22(1):119-137.
[47] T. K. Kim, S. J. Choi, J. H. Choi, et al. Prediction of chloride penetration depth rate and diffusion coefficient rate of concrete from curing condition variations due to climate change effect[J]. INT J CONCR STRUCT M, 2019,13(1):1-13.
[48] G. R. Meira, C. Andrade, C. Alonso, et al. Salinity of marine aerosols in a Brazilian coastal area-influence of wind regime[J]. ATMOS ENVIRON, 2007,41(38):8431-8441.
[49] I. S. Oslakovic, D. Bjegovic, D. Mikulic. Evaluation of service life design models on concrete structures exposed to

marine environment[J]. MATER STRUCT, 2010,43(10):1397-1412.
[50] M. E. R. Gustafsson, L. G. Franzen. Dry deposition and concentration of marine aerosols in a coastal area, SW Sweden[J]. ATMOS ENVIRON, 1996,30(6):977-989.
[51] R. J. Santucci, R. S. Davis, C. E. Sanders. Atmospheric corrosion severity and the precision of salt deposition measurements made by the wet candle method[J]. CORROS ENG SCI TECHN, 2022,57(2):147-158.
[52] R. Meirag, C. Andrade, I. J. Padaratz, et al. Chloride penetration into concrete structures in the marine atmosphere zone-Relationship between deposition of chlorides on the wet candle and chlorides accumulated into concrete[J]. CEMENT CONCRETE COMP, 2007,29(9):667-676.
[53] T. Uomoto, T. Ishibashi, Y. Npbuta, et al. Standard specifications for concrete structures—2007 by Japan society of civil engineers[J]. CONCR J, 2008,46(7):3-14.
[54] Z. J. Tang, K. X. Liao, X. L. Kong, et al. Diffusion of chloride ion into containment concrete under coastal environment[J]. CONCRETE, 2015(5):66-69.
[55] N. Nosratzehi, M. Miri. Experimental investigation on chloride diffusion coefficient of self-compacting concrete in the Oman Sea[J]. PERIOD POLYTECH-CIV, 2020(11):647-657.
[56] Rasheeduzzafar, S. S. Al-Saadoun, A. S. Al-Fahtani, et al. Effect of tricalcium alumina content of cement on corrosion of reinforcing steel in concrete[J]. CEMENT CONCRETE RES, 1990,20(5):723-738.
[57] G. Blunk, P. Gunkel, H. G Smolczyk. On the distribution of chloride between the hardening cement pastes and its pore solutions. Proceedings of the 8th international congress on the chemistry of cement[J]. MATERIA-BRAZIL, 1986(4):85-90.
[58] C. Arya, N. R. Buenfeld, J. B. Newman. Factors influencing chloride binding in concrete[J]. CEMENT CONCRETE RES, 1990,20(2):291-300.
[59] Rasheeduzzafar. Influence of cement composition on concrete durability[J]. ACI MATER J, 1992,89(6):574-585.
[60] A. K. Suryavanshi, J. D. Scantlebury, S. B. Lyon. The binding of chloride ions by sulphate resistant cement[J]. CEMENT CONCRETE RES, 1995,25(3):581-592.
[61] Zibara Hassan. Binding of external chloride by cement pastes[D]. Department of building materials Ontario:University of Toronto,2001.
[62] A. K. Suryavanshi, J. D. Scantlebury, S. B. Lyon. Mechanism of Friedel's salt formation in cements rich in tri-calcium aluminate[J]. CEMENT CONCRETE RES, 1996,26(5):717-727.
[63] H. Justnes. A review of chloride binding in cementitious systems[J]. NORD CONCR RES, 2000(21):1-16.
[64] V. S. Ramachandran. Possible states of chloride in the hydration of tricalcium silicate in the presence of calcium chloride[J]. MATER STRUCT, 1971,4(1),3-12.
[65] L. Tang, L. O. Nilsson. Chloride binding capacity and binding isotherms of OPC pastes and mortars[J]. CEMENT CONCRETE RES, 1993,23(2):247-253.
[66] J. J. Beaudoin, V. S. Ramachandran, R. F. Feldman. Interaction of chloride and C-S-H[J]. CEMENT CONCRETE RES, 1990,20(6):875-883.
[67] P. Lambert, C. L. Page, N. R. Short. Pore solution chemistry of the hydrated system tricalcium silicate/sodium chloride/water[J]. CEMENT CONCRETE RES, 1985(15):675-680.
[68] Cui Ling. Invasion mechanism and distribution development of chloride ions in concrete structures under marine environment[D]. Qingdao: Qingdao Technological University, 2010.
[69] Y. S. Ji. Whole life processes and projections for reinforced concrete[D]. Beijing:China Railway Press, 2011.
[70] K. Venu, K. Balakrishnan, K. S Rajagopalan. A potentiokinetic polarization study of the behaviour of steel in NaOH - NaCl system[J]. CORROS SCI, 1965(5):59-69.
[71] P. Ghods, O B Isgor, G. McRae, et al. The effect of concrete pore solution composition on the quality of passive oxide films on black steel reinforcement[J]. CEMENT CONCRETE COMP, 2009,31(1):2-11.
[72] L. Li, A. A. Sagüés. Chloride corrosion threshold of reinforcing steel in alkaline solutions- open-circuit immersion tests[J]. CORROSION-US, 2001(57):19-28.
[73] Y. T. Tan, S. L. Wijesinghe, D. J. Blackwood. The inhibitive effect of bicarbonate and carbonate ions on carbon steel in simulated concrete pore solution[J]. CORROS SCI, 2014(88):152-160.
[74] R. B. Figueira, A. Sadovski, A. P. Melo, et al. Chloride threshold value to initiate reinforcement corrosion in simulated concrete pore solutions: The influence of surface finishing and pH[J]. CONSTR BUILD MATER, 2017(141):183-200.
[75] Q. Q. Zhang, W. Sun, J. P. Liu. Analysis of factors affecting critical chloride ion concentration in concrete simulation fluids[J]. Journal of Southeast University, 2010,40:177-181.

Viser Technology Pte. Ltd.
Research and Application of Materials Science
DOI: 10.33142/rams.v6i2.14583

Research Article Open Access

Characterization of a Bonding Method for High Borosilicate Glass to Kovar Alloy Sealing by Laser Welding

Changjun CHEN[1, 2], Jiaqi SHAO[1], Min ZHANG[1*]

1. Laser Processing Research Center, School of Mechanical and Electric Engineering, Soochow University, Suzhou, Jiangsu, 215131,China
2. State Key Laboratory of Advanced Welding and Joining, Harbin Institute of Technology, Harbin, Heilongjiang, 150001, China

Correspondence: Min ZHANG, E-mail: 63606536@qq.com

Abstract

Glass to metal sealings have many excellent properties and they are extensively used in various industries. Applications for laser glass tube for carbon dioxide laser requires hermetic and mechanically strong seals. With the purpose of fully utilize its effectiveness of glass and metal sealings' properties and enlarge their applications, bond the glass to metal is an important method. Hermetic seals between kovar alloy and borosilicate glass can be produced using a novel laser sealing method when compared to bonding method based on glass pressing at temperatures around the softening point. This paper presents investigation results for the shear tensile bond strength and the waterproof resistance depending on the manufacturing process parameters. The shear bond strength of the glass to metal sealing was amounted to only 9.84 MPa when using traditional high temperature holding process. The maximum shear bond strength can be amounted to 43.68 MPa when sealed by laser welding process. And good adherence with a very high waterproof resistance can ben obtained. The bonding mechanisms was revealed by SEM methods to analyze the interface.

Keywords: glass to metal sealing; laser welding; shear strength

1 Introduction

With the rapid development of industrial fields, glass to metal sealings are extensively used in the fields which can create vacuum-tight electrical connectors, feedthroughs or optical windows and lenses in electrons or electronic system to meet requirements for harsh environments and high performance. Glass to metal sealings are widely used in industrials such as encapsulated electrical components and systems, semiconductors, electro-chemicals, pyrotechnics, or other substances [1-7]. Glass-to-metal sealing plays a very important role in electronic packaging. Glass to metal sealing can meet a wide variety of specific requirements such as airtight, hermetic packaging applications, whose performance, safety, and durability are very crucial [1-7]. The quite different properties exist between glass and metal, hermetic and reliable bonding between glass and metal is a big challenge for us. Hermetic sealing quality of glass to metal sealings are engineered to deliver uncompromised reliability. Given that the glass material and the metal alloy are quite different materials in physical and chemical properties, the hermetic bonding between glass and metal will be a big challenge when they are used in our actual industrial areas.

Laser functional and electronic devices such as laser glass tube for carbon dioxide laser are encapsulated with the purpose of protecting the specific gases from leakage and activated into powerful Kovar alloys combine mechanical strength with similar coefficient of thermal expansion (CTE) to borosilicate glass, making them the material of candidate for most high performance containing electronic systems. Figure 1 demonstrates a laser glass tube for carbon dioxide laser electronic system, which is a typical application of borosilicate glass to kovar alloy sealing. Optical windows having function of optical diagnosis systems are other applications for this type glass to metal sealing. High-quality clear-transparent borosilicate glasses offers excellent and uniform optical transmission from the visible to the infrared spectrum and has remarkable thermal capabilities, and retains its mechanical strength. What's more, the hermetic kovar alloy and the glass sealing is a very important component part of the carbon dioxide laser system, as shown in Figure 1 (a).

Bonding of glass and metal is an old technology and has a rich history. What's more, glass-to-metal seals have now been in use for over a hundred years dating back to ancient times. At that time, then on metal surfaces, decorative glass coatings were manufactured. First glass melting and then wetting of the metal surface is the process of this ancient coating technology, and

Received on September 13, 2024; Accepted on October 20, 2024

later, it is called as enameling. Light bulbs and enameled cookware are most industrial applications in our daily life. And they are manufactured by the enameling process, in which using high temperatures to melt the glass, allowing it to wet the metal surface [1]. And the construction of vacuum tubes, electric discharge tubes, semiconductor diodes, reed switches, and pressure-tight glass-to-metal windows are the other common use. The basic process is sealed in a temperature-controlled oven, and the assembly is heated to the appropriate temperature for the particular variety of glass to melt and fill the space between the pin and the metal package. Hermetic sealing of glass and metal to meet the requirement of electronics industry is still challenging and is a hotspot in the current days. And researchers pay much attention to study this research area [8-9]. The shortcomings of this method is the high temperature heating and long time holding, it will cost large energy and high temperature treatment also may harm the functional properties of glass and/or metals. And it is not easy to achieve automatic production.

Due to the shortcomings of the traditional glass to metal sealing process used high temperature heating process, other low temperature process used for glass to metal sealing have been introduced by many researchers [10]. The anodic bonding process is a typical example [10]. During this bonding process, the glass remains in its solid state and the glass-to-metal interface is created by static electric fields. In the microfluidics industry, this sealing methods is already get applied [11].

With the purpose of trying to find an alternative solution, low temperature heat process used for glass-to-metal bonding technology was once introduced in refences [12-19], has emerged as an important research in advancing welding technology. Laser welding technology has the advantages that has low process temperature and also it can be operated under atmosphere.

The interface created at highly focused laser energy and formed on localize zone, which allows an interim transitional zone contained both glass and metal. The main research objectives of the present paper is to investigate the laser process parameters on the sealing quality of the glass to metal sealing.

Kovar alloy, a nickel-cobalt-ferrous alloy, is one of the most commonly used glass sealing alloys. While borosilicate glass has constitutions of silicon oxide, boron oxide, and sodium oxide [20], which has outstanding properties such as low CTE, good thermal stability, high mechanical property. Due to borosilicate glass's excellent properties, it is widely used in nuclear filed, electronic devices and electronics, optical window, vacuum-tight electric connectors and so on [21].

Success bonding between Kovar alloy and borosilicate glass was achieved by Satoru Nishikawa and Makoto Takahashi [22] using anodic bonding. In their study, the authors attempted to study the influence of voltage on the sealing joint and they analyzed the element distribution feature on the bond surface. And it can be inferred that the remaining contact area will be influenced by changing the bonding temperature. The mechanical properties and the microstructure characteristics of the joint between borosilicate glass and stainless steel once reported by authors Li et al. [21]. They analyzed the influence factors of shear strength of joint, such as bonding temperature, surface pretreatment, and reaction time were analyzed in their study. The maximum shear strength 27 MPs can be obtained at the conditions of holding at 1050 ℃ for 45 min, and the 304 SS was pre-oxidized.

The present study examined the quality of glass to metal sealing by a modern laser welding technology. First, the Kovar alloy was underwent high-temperature pre-oxidization treatment with the purpose to producing an oxide layer with a certain thickness and adhesion on kovar alloy surface. Previous research recommended that the optimum oxide layer formed and the alloy surface, which can be bonded with a high quality junction is about several μms [23]. According to the published literature and the authors previous published paper [1,23], the optimum oxidizing temperature and holding time is easily determined in the present paper. Then the glass to metal sealing is sealed by laser welding technology. The interface structure is examined and the shear tension strength and leakage properties are determined.

2 Expermiental Procedure

2.1 Preparation of samples

The laser bonding of kovar alloy and borosilicate glass, as an alternative sealing methods is used in the present study. Kovar alloy has a composition of 29% Nickel, 17% Cobalt, Balance Iron (in wt %) and its Coefficient of Thermal Expansion (CET) is 50 $\times 10^{-7}$ / ℃. High borosilicate glass has excellent chemical stability, thermal stability and good mechanical properties, and has been widely used in instrument glass, fireproof glass, flat panel display and solar cells and other fields.

The high borosilicate glass chosen for the present investigation has a coefficient of thermal expansion (10.3×10^{-6} K^{-1}). It is similar to the coefficient of thermal expansion of kovar allloy (50 x 10^{-7} / ℃). It has a composition of SiO_2 (80.4%), B_2O_3 (12.7%), Al_2O_3 (2.4), Na_2O and K_2O (4.2%), others BaO (0.3%), all in weight percent.

2.2 Preoxidation treatment

The Kovar samples are flat shapes with dimensions 10mm×10mm×3mm. Filled with atmospheric air, the samples are heated in a muffle furnace at a heating rate of 40 ℃ min^{-1} to three different temperatures, i.e 700, 800 and 900 ℃, for seven different isothermal holding periods of 0, 3, 5, 10, 15, 30 and 60 min. After heat

treatment, all the samples are cooled to room temperature by cooling at 20 ℃ min^{-1}. According to previous published papers [1, 23], the optimal process parameters was selected as following: 800 ℃ and holding 5 minutes.

2.3 Bonding process: laser welding

The experimental setup for laser transmission bonding and weld strength measurement was shown in Figure 2. And Figure 2 (a) illustrates the welding process and Figure 2 (c) shows a picture of the real clamp for welding sample. Laser processing parameters are selected as following: 150 W, 200 W, 250 W, 300 W, 350 W and scan speed 0.3 mm/min. The focus distance are selected as 0 mm, 0.5 mm (focus beam is located in the glass) and -0.5 mm (focus beam is located below the metal surface). The pulse width is set as 2.8 ms and the laser frequency is selected as 10 Hz.

The Glass to metal welding experiment was conducted using an MD-Focus 500 NdYAG pulsed laser. This type of laser has wavelength of 1064 nm and it has a maximum average power of 500 W. This laser also has a maximum frequency of 500 Hz and its pulse width can be varied from 0.1 to 20 ms. A lap joint form was used for the glass to metal welding as shown in Figure 1(c). A fixture was designed to provide pre-tightening force to reduce the gap between the glass to metal, as shown in Figure 2 (c). Figure 2(a) shows the schematic diagram of the fixture and Figure 2 (b) demonstrate the welding state during laser welding process. Glass to metal sealing samples are laid on the fixture's workbench.

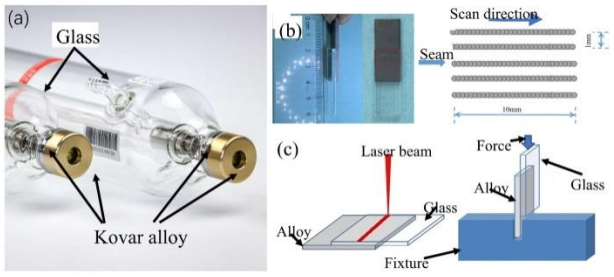

Figure 1 Laser glass tube for carbon dioxide laser (a), glass to metal sealing samples formed by laser welding (left sample) and its scan direction (right picture), a typical example for glass to metal sealing (b), and schematic illustration of the glass to metal sealing sample welded by laser welding process (left picture) and the shear test (right picture) (c) (drawings not to scale)

2.4 Microscopic observation and measurement of tensile strength and waterproof test

The glass to metal sealing samples are cross-sectioned, mounted and then they are polished into mirror surface and etched using 10% Nital (10% nitric acid +90% alcohol). Samples (joint interface and oxide layer formed on metal surface) for microstructure observation are then observed using optical microscope and scanning electron microscope (SEM, JOEL, JSM-7000F).

The shear strength of the obtained glass to metal sealing is indicated by modified the traditional tensile test machine. The shear tensile testing machine used in the present study was the QC-548M2F-Computerized Tensile/Compression Testing from Cometech Testing Machines Co., in a line rate of 20 N/s up to 1000 N and capable of applying a maximum tensile force of 5 kN and with a feeding speed ranging from 0.0002 to 3 mm/min. During the sample separation process, recorded the load as a function of position with an accuracy of 0.001% was recorded the load by a digital dynamometer. And the shear strength is calculated by the applied load to the sample weld seam area. Figure 1(c) shows the schematic diagram of the shear tests.

The sealed samples were directly subjected to water bath furnace, heating at a higher temperature 150 ℃ holding for 30 minutes. And they were taken from the bath, cooled to room temperature. And after cleaning and dried by hot wind, the samples were tested by PET Colorant to see there exists obvious crack or not by naked eyes.

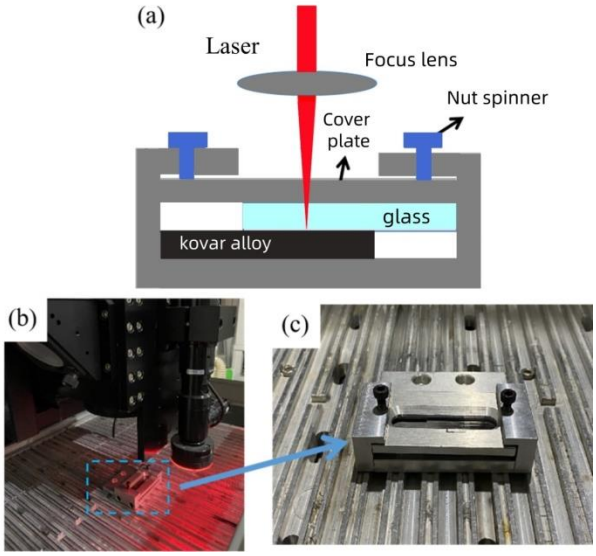

Figure 2 Schematic diagram of the picture shown the welding: schematic diagram of laser welding with a clamp, (b)real welding photo and (c)its real clamp (drawings not to scale)

3 Results and discussion

3.1 Tensile bond strength and waterproof resistance

The shear strength plays a critical role in determining the quality of glass to metal sealing. During laser welding process, laser processing energy is one of the most important processing parameters, which can significantly affect the final joint quality. Figure 3 demonstrates the shear strength (SS) as a function of laser power for three different focal plane positions. The laser power was varied by adjusting the laser output

power ranged from 100 W to 350 W, i.e, 100 W, 150 W, 200 W, 250 W, 300 W and 350 W. The three focal plane positions were negative (0.5 mm below the interface, i.e below the metal surface), at the interface, and positive (0.5 mm above the interface, i.e in the glass), respectively. During laser welding processing, a fixed sample jig clamping force of 60 N was applied to provide pressure assistance and ensure the close contact.

Traditional glass to metal sealing strength once was reported that the shear strength value can be reached 9.84 MPa [1,24]. So the present study achieved higher strength when compared to tradition furnace sealing process. During the present study, the shear strength is shown in Figure 3. It can be seen that the strength is increased first. When it is amounted to maximum value and then decreased. Strength results showed that the focus plane and laser power have significant effects on the seal strength. Maximum strength can be reached to 43.68 MPa when the laser power is 250 W under the conditions of the focus plane was set as -0.5 mm. And it can be seen that all the strength results obtained under -0.5mm are higher than that those obtained under 0 mm and + 0.5 mm focus plane.

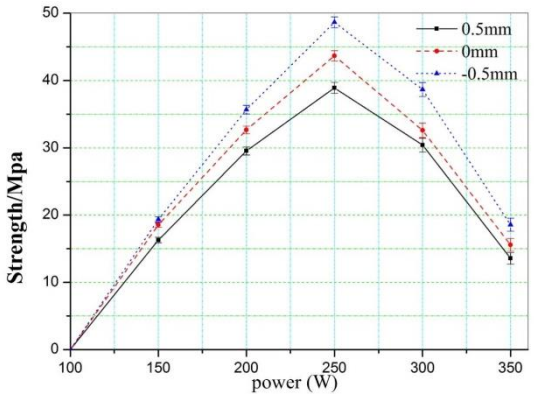

Figure 3 Experimental results demonstrating the variation of shear strength with incident laser pulse energy varied from 100 W to 350 W under three different laser focus plane

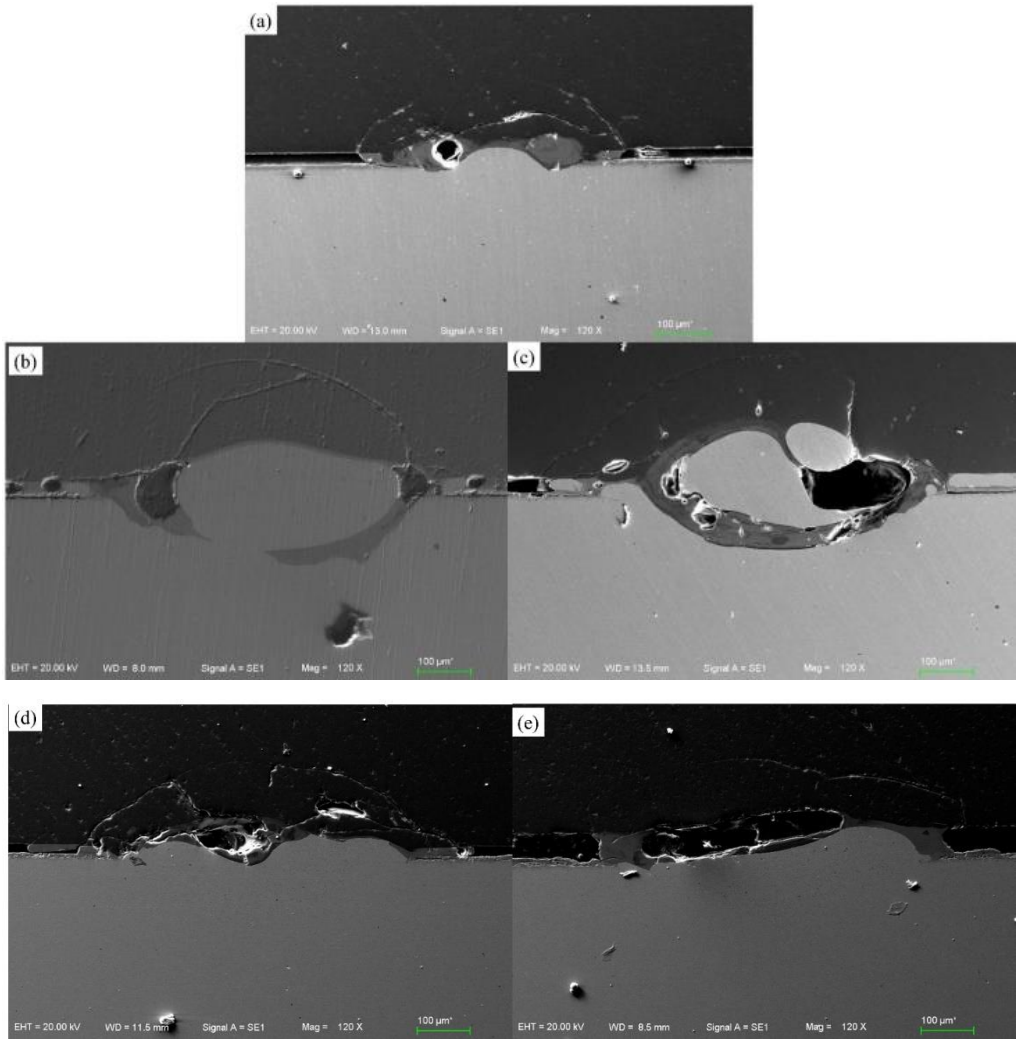

Figure 4 Cross-sectional SEM pictures showing the cross-section interface between glass to kovar sealing under different laser process parameters: (a); 150 W; (b)200 W; (c)250 W; (d) 300 W; (e)350 W;

And according to the waterproof testing results, the waterproof level can be reached to IPX7. After PET Colorant test, there exists no obvious crack by naked eyes.

Five of the glass to kovar alloy sealing samples with chosen laser processing parameters were cross-sectioned perpendicular to the glass to metal sealings interface, then they were mounted, grounded, polished for the preparation of microscope observation by SEM. Figure 4 demonstrates the SEM pictures for the selected laser process parameters observed for the interface. These images depict the internal structure of the welds before separation. These images depict the internal structure of the welds before separation. And it can be clearly seen the bonding zone between glass and kovar alloy.

3.2 Bonding mechanism

Glass to metal sealing mechanism can be roughly divided into mechanical bonding and metallurgical adhesion [25]. And interlocking is the base for the mechanical bonding. In mechanical bonding, one material will fill voids, pores of the another material. While, metallurgical bonding interface successfully forms through electrostatic and molecular forces. And the commons forms are chemical forces or van der Waals forces.

The oxide layer was obtained by pre-oxidation of Kovar alloy and then the sealing of the glass to the pre-oxidized metal can be obtained. For mechanical and hermetic sealing also requirements were comprised of an adequate wetting of the pre-oxidized alloy surface by the glass and an appropriate dissolution of the surficial metal oxide in the glass, without formation of detrimental crystal phases [1, 24]. These requirements were shown to depend on the values of temperature, time and atmosphere of sealing under optimized with the values mentioned above.

In general, optimal oxide film formed on the kovar alloy surface and proper laser processing parameters are the fundament reasons to obtain both good shear strength and hermetic seal quality defined by waterproof test.

In the SEM images in Figure 4, the materials are bonded together after laser welding. And no visible gap between the glass to metal sealing interface can be clearly seen under the present magnification. The observed seal quality is verified by the high shear strength and high waterproof measured in samples produced with the same process parameters. Accordingly, the measured waterproof is high. However, the parameter combination resulted in a relatively high shear strength amounted to 43.68 N.

The SEM images in Figure 4 show that the shapes are spherical cavities in the glass sample that were exposed during the preparation of the SEM samples. Due to the fact that not all the sample have cavities, it can be inferred that they must be formed during the bonding process. Gas is the main reason for the formation of cavities. And there are two main sources of gas formation, i.e., one comes from already existed gas and the another originates from chemical reaction during the laser welding process at higher temperatures. Till to now, such phenomenon were not reported in the literature references. And the higher strength can be obtained by -0.5 mm focus plane means that the bonding is achieved by melted metal alloy surface first and then mixed with glass.

4 Conclusion and Outlook

Results with high shear strength and high waterproof resistance glass to metal sealing occur under optimal proxidation kovar alloy and laser processing parameters. Good mechanical joint can be obtained and the maximum shear strength can be amounted to as high as 43.68 MPa in the present study.

Bubble formation at the interface can be seen in some laser process parameters. Shear strength can be amounted to 43.68 MPa. And selected parameters can be selected by analyzed the glass to metal sealing interface using SEM.

It is very important that deep understanding the bonding mechanisms to obtain a better sealing performance with the optimal process parameters.

What's more, finite element method can be used and studied on the stress evolution and forming to obtain process parameter optimization.

Fund Projects: We would like to appreciate Jiangsu Province Key Research and Development Program (Grant No. BE2021049), the Open Fund for State Key Laboratory of Advanced Welding and Joining, Harbin Institute of Technology [Grant No. AWJ-23Z01], and the Open Fund for National Key Laboratory for Remanufactury [Grant No.xxx].

References

[1] Donald I, Mallinson P, Metcalfe B, et al. Recent developments in the preparation, characterization and applications of glass-and glass-ceramic-to-metal seals and coatings[J]. Journal of Materials Science, 2011(46):1975–2000.

[2] Song S. New glass-ceramic sealants for Na/S battery[J]. Journal of Solid State Electrochemistry, 2010, 14(9):S1735–S1740.

[3] Gomez-Vega J , J. M. Gomez-Vega, A. Hozumi, et al. Bioactive glass-mesoporous silica coatings on Ti6Al4V through enameling and triblock-copolymer-templated sol-gel processing[J]. Journal of Biomedical Materials Research Part A, 2001(3):56:307–459.

[4] Yi R., Chen, C., Li, Y. et al. The bonding between glass and metal [J]. International Journal of Advanced manufacturing

technology, 2020(111):963–983.
[5] Zhang LX, Wu LZ, Liu D, et al. Interface microstructure and mechanical properties of the brazed SiO2 glass ceramic and 30Cr3 high-tensile steel joint[J]. Materials Science and Engineering A, 2008, 496(1–2):393–398.
[6] Smeacetto F, Salvo M, Ferraris M, et al. Glass–ceramic seal to join Crofer 22 APU alloy to YSZ ceramic in planar SOFCs [J]. Journal of European Ceramic Society, 2008,28(1):61–68.
[7] Guedesa APA, Vieira M, Viana F. The effect of brazing temperature on the titanium glass-ceramic bonding [J]. Journal of Materials Processing Technology, 1999(92-93):102–106.
[8] Donald I.W. Preparation, properties and chemistry of glass- and glass-ceramic-to-metal seals and coatings[J]. Journal of Materiasl Science, 1993(28):2841–2886.
[9] A. Pazo, E. Saiz, A. P. Tomsia. Silicate glass coatings on Ti-based implants [J]. Acta Materialia, 1998, 46(7):2551-2558.
[10] Kuckert H, Born C, Wagner G, et al. Helium-tight sealing of glass with metal by ultrasonic welding[J]. Advanced Engineering Materials, 2001(3)3:903–905.
[11] Khandan O, Stark D, Chang A, et al. Wafer-scale titanium anodic bonding for microfluidic applications[J]. Sens Actuators B Chem, 2014(205):244–248.
[12] Harinarayana V., Shin Y.C. Experimental and numerical investigation on laser transmission welding of stainless steel 304 L and borosilicate glass[J]. International Journal of Advanced Manufacturing Technology, 2024(132):2661–2675.
[13] Xu M., Chen, C., Shao J. et al. Effect of High-Temperature Oxidation on Laser Transmission Welding of High Borosilicate Glass and TC4 Titanium Alloy[J]. Journal of Materials Engineering and Performance, 2024(130):1-11.
[14] Nguyen H., Lin CK., Tung PC. et al. Characterizations of laser transmission welding of glass and copper using nanosecond pulsed laser[J]. International Journal of Advanced Manufacturing Technology, 2024(130):2755–2770.
[15] Ji Ch., Huang, Yj., Chen, X. et al. Direct microwelding of dissimilar glass and Kovar alloy without optical contact using femtosecond laser pulses[J]. Journal of Centre. South University, 2022(29):3422–3435.
[16] Min Z., Yufei C., Changjun, C. et al. A new sealing technology for ultra-thin glass to aluminum alloy by laser transmission welding method[J]. International Journal of Advanced Manufacturing Technology, 2021(115):2017–2035.
[17] Lipat'eva, T.O., Fedotov, et al. Precision Laser Welding of Silica Glass with Iron-Nickel Alloy[J]. Glass Ceram 77, 2021(77):435–437.
[18] Chenyun Tian, Haodong Ren, Hong Shen .The connection of glass and metal with a large gap by combining laser soldering and ultrafast laser welding[J]. Journal of Manufacturing Processes, 2023(102):528-534.
[19]Lei Li, Changjun Chen, Chunlei Li, et al. The influence of anodization on laser transmission welding between high borosilicate glass and TC4 titanium alloy [J]. Optics & Laser Technology, 2025(181):111590.
[20] Peng HB, Sun ML, Yang KJ, et al. Effect of irradiation on hardness of borosilicate glass[J].journal of Non-crystalline Solids, 2016(443):143–147.
[21] Li S, Hu K, Hui W, et al. Shear strength and interfacial characterization of borosilicate glass-to-metal seals[J]. Journal of Alloys& Compounds, 2020(827):154275.
[22] Nishikawa S, Takahashi M. (2019) Effect of application of opposite polarity voltage on interface separation of anodically bonded kovar alloy–borosilicate glass joints[J]. Sensors Actuators A Physics, 2019(296):367–374.
[23] Tsann-Shyi Chern, Hsien-Lung Tsai.Wetting and sealing of interface between 7056 Glass and Kovar alloy[J]. Materials Chemistry and Physics. 2007,104(2-3):472-478.
[24] Seyed Sadegh Khayat Ardestani, Valiollah Dashtizad, Ali Kaflou. Experimental investigations on time, temperature and atmosphere influence on microstructure and mechanical properties of borosilicate glass to Kovar-alloy seals[J]. Materials Characterization, 2021(171):110805.
[25] Bischof C, Possart W. Adhäsion: theoretische und experimentelle Grundlagen[M]. Berlin:Akademie-Verlag Berlin, 1983.

Viser Technology Pte. Ltd.
Research and Application of Materials Science
DOI: 10.33142/rams.v6i2.14584

Research Article Open Access

Based on Orthogonal Experimental Analysis: Effects of Formulation Systems on the Mechanical, Heat Resistance, and Aesthetic Properties of High-Gloss Black PMMA/ASA Alloys

Lulin WANG, Yeming XIAN*, Wentao YU, Juean DENG, Lin CHEN

Super-Dragon Engneering Plastics Co., Ltd, Guangzhou, Guangdong, 510945, China

*Corresponding Author: Yeming XIAN, E-mail: yeming_xian@qq.com

Abstract

High gloss and heat resisting PMMA/ASA is applied in many fields such as automotive materials. There are many researches focusing on single properties but no comprehensive quantitative evaluation. In this work, we used orthogonal experiments and variance methods, along with a custom Python program, to conduct in-depth experimental analysis and provide a comprehensive evaluation of the performance of each component in the material system. The results demonstrate that this analysis method can appropriately assess the enhancements that each functional component contributes to corresponding performances. Additionally, it was observed that the strategy of blending high and low melt flow index PMMA affects the overall performance, as the application of high and low melt flow index PMMA changes the distribution and gradient of the functional components, significantly enhancing performance for certain surface or gradient-sensitive properties.

Keywords: PMMA/ASA alloy; Orthogonal Experimental Analysis; classroom teaching

1 Introduction

Poly (methyl methacrylate) (PMMA), is one of the most common non-crystalline, highly transparent engineering plastics. It is widely used in optical devices [1], consumer electronics[2-3], aerospace[4-5], automotive materials[6-7], and other fields[8]. In addition, the high transparency of PMMA allows it to achieve high gloss and high brightness effects, enabling aesthetic finishes such as high-gloss black and piano black [7, 9-10]. However, PMMA typically exhibits certain brittleness and insufficient heat resistance, often requiring the introduction of acrylonitrile-styrene-acrylate (ASA) copolymer to form PMMA/ASA alloys in order to improve its heat resistance and impact toughness[9, 11]. ASA resins offer better resistance to environmental stress cracking, improved processing performance, and excellent compatibility with PMMA and PC, making them widely used in modified plastic products[12- 13].

Current researches on PMMA/ASA alloys usually focuses on evaluating individual formulation components[7, 14-15]. Based on these studies, the general effects of different formulation systems on alloy properties can be assessed. However, there is still a lack of comprehensive and systematic evaluations of the reliability of these formulation systems. This paper will use orthogonal experiments and hypothesis testing methods to quantitatively evaluate the impact of various formulation systems on the performance and appearance of high-gloss black PMMA/ASA alloys.

2 Experimental

2.1 Materials

The materials used in this work are listed as below:

High melt index PMMA: CM 211, purchased from Chi Mei Corporation;

Low melt index PMMA: CM 205, purchased from Chi Mei Corporation;

Toughening agent: LP2068, purchased from Guangzhou Entropy Energy;

MABS: 758, purchased from Chi Mei Corporation;

MABS: 920, purchased from Toray Malaysia.

Antioxidants: 1076, 168, purchased from BASF.

2.2 Sample Preparation

According to the mixing-level orthogonal experiment, the materials were prepared based on the experimental formulation. After thorough mixing, the mixture was granulated using an twin screw extruder (CTE-35, Nanjing Ruiya). The temperature settings for each section of the extruder were 240 ℃, 250 ℃, 260 ℃, 270 ℃, 260 ℃, 250 ℃, 250 ℃, 250 ℃. The die

Received on September 6th, 2024; Accepted on October 11, 2024

temperature was set to 275 ℃, and the screw speed was 400 rpm. After granulation, the material was left to rest at 80 ℃ for 24 hours, then injection molded into tensile, impact test specimens and flat plates for further testing.

Table 1 Formula of PMMA/ASA used in this work

PMMA211 ratio	LP2068	MABS	1550F	1076	168
-	phr	phr	phr		
0.2	15	10 (758)	36	0.1	0.4
0.2	20	10 (920)	29	0.1	0.2
0.2	25	0	22	0.2	0.4
0.2	30	5 (758)	15	0.2	0.2
0.3	15	10 (920)	22	0.2	0.2
0.3	20	10 (758)	15	0.2	0.4
0.3	25	5 (758)	36	0.1	0.2
0.3	30	0	29	0.1	0.4
0.2	15	10 (758)	36	0.1	0.4
0.2	20	10 (920)	29	0.1	0.2
0.2	25	0	22	0.2	0.4
0.2	30	5 (758)	15	0.2	0.2
0.3	15	10 (920)	22	0.2	0.2
0.3	20	10 (758)	15	0.2	0.4
0.3	25	5 (758)	36	0.1	0.2
0.3	30	0	29	0.1	0.4

2.3 Testing

Mechanical properties testing: The tensile tests were conducted by a tensile tester (ZBC8400B) according to the standards GB/T 1042-2006 and GB/T 1843-2008, with the tensile test performed at a speed of 50 mm/min. The impact tests were conducted by a impact tester (GT-7045-MDL).

Heat resistance: The heat deflection temperature (HDT, 1.8 MPa) and Vicat softening temperature (VST, B50) were tested by.

Appearance properties: A color difference meter (X-RITE 7600) was used to analyze the color changes of the flat plates.

2.4 Data analysis:

The experimental data were analyzed using a Python program developed by the team, with the Pandas, scipy, and numpy libraries imported. The experimental results were evaluated in terms of the impact of each component on performance using range analysis and variance analysis.

Range analysis was performed by subtracting the minimum value from the maximum value in the data sample. The result, denoted as R in the figures, indicates that the larger the R value, the greater the influence of the factor on the performance. Variance analysis was performed using the following four-step procedure [16]:

(1) Calculate the total sum of squares of deviations:

$$SST = \sum(y_i - \bar{y})^2 \quad (1)$$

where SST is the sum of squares of deviations, yi represents the data points, and $\bar{y}$ is the mean value of the data set.

(2) Calculate the sum of squares of deviations for each factor:

$$SSA = \sum_{i=1}^{n} n_i(\overline{T_i} - \bar{y})^2 \quad (2)$$

$$MSA = \frac{SSA}{n-1} \quad (3)$$

where SSA is the sum of squares of deviations for factor A, and MSA is the mean square for the factor. n represents the number of levels of the factor, ni is the number of experiments at the i-th level, and $\overline{T_i}$ is the mean of the data at the ii-th level.

(3) Calculate the error sum of squares: The error sum of squares (SSE) and mean square error (MSE) are obtained by taking the minimum value from step (2).

(4) Calculate the F-value:

$$FA = \frac{MSA}{MSE} \quad (4)$$

(5) Calculate the P-value from the F-distribution:

$$PA = P(F > FA) \quad (5)$$

This analysis was conducted using Python's scipy library. In the figures of this paper, each orthogonal analysis includes a P-value. When $P < 0.05$, it indicates that the P-value is smaller than the significance level, allowing for the rejection of the null hypothesis, which suggests that the conclusions drawn from the graph are statistically significant. In engineering practice, it is also generally accepted that when $0.05 < P < 0.1$, the factors are weakly correlated or marginally significant.

3 Results and Discussion

3.1 Mechanical Properties

The introduction of heat stabilizers and toughening agents is expected to affect the mechanical properties of the material. As shown in Figure 1, after the incorporation of various additives, the mechanical properties of the material system changed to varying degrees. LP2068, an ASA-type toughening agent, has a fine and uniform rubber phase, which causes the material's tensile strength to decrease from 63.3 MPa at 15 phr to 51.3 MPa at 30 phr (P=0.002), while the impact strength increases from 3.99 MPa at 15 phr to 8.04 MPa at 30 phr (P=0.002). MABS 758 and MABS 920 are two types of transparent ABS, and the experimental results show that both slightly decrease the tensile strength (P=0.014). The heat stabilizer 1550F has no effect on the mechanical properties of the material system ($P > 0.1$). It can be said that the changes in mechanical properties generally follow the pattern predicted by the mixing law.

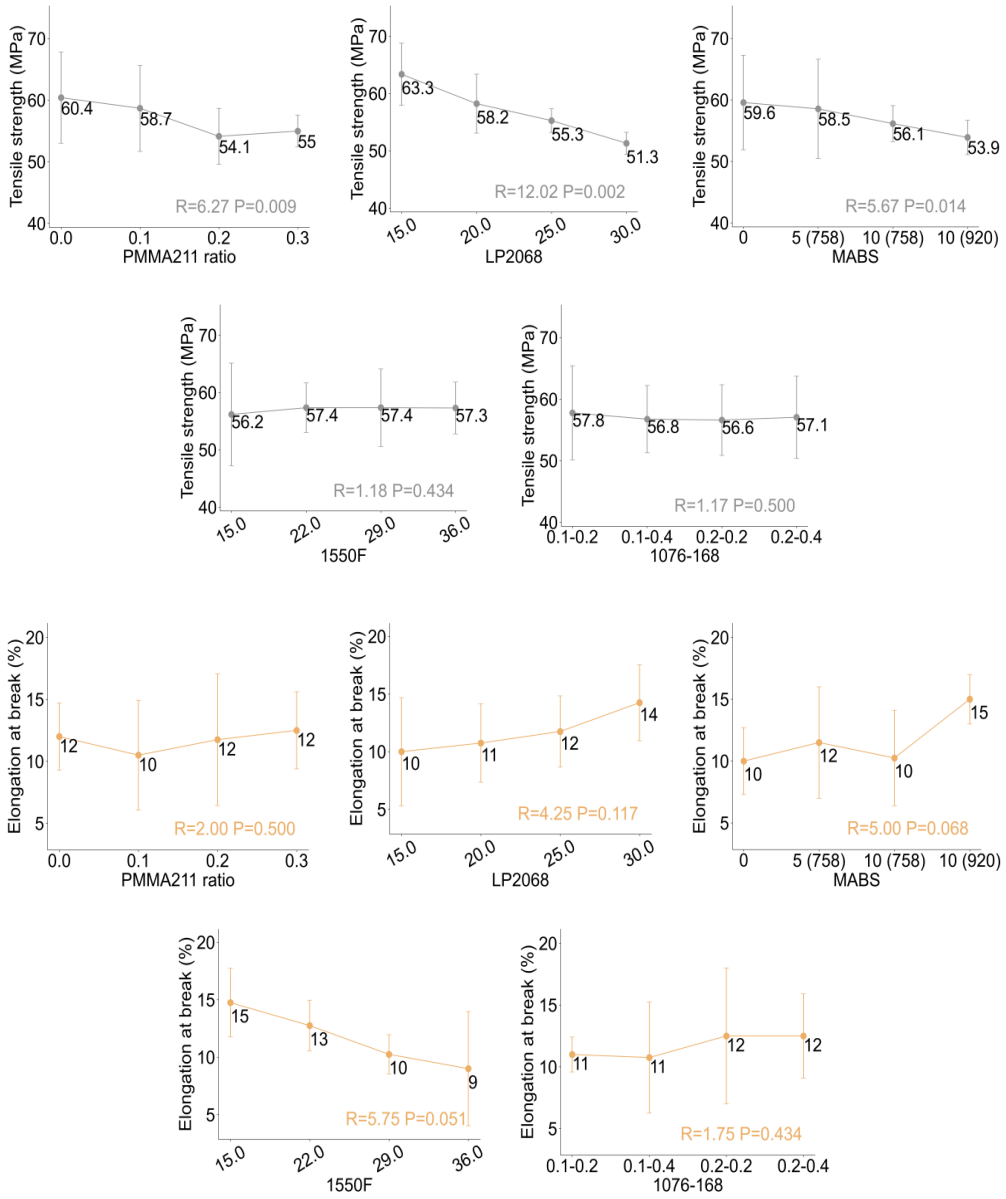

Figure 1 The formula vs. tensile properties

A significant conclusion arises from the addition of high-flow PMMA 211 to the system for PMMA-based materials, which has a notable impact on mechanical properties. When PMMA 211 was added at a proportion of 20%, the tensile strength decreased from 60.4 MPa to 54.1 MPa (P=0.009), while the impact strength increased from 4.64 to 7.24 (P=0.003). Compared to the slight decrease in tensile strength, the substantial improvement in toughness is undoubtedly a positive result.

To explore the true reason of this phenomenon, we conducted further verification experiments, as shown in Figure 3. We replaced the PMMA substrate with higher melt-flow PMMA 211 in both toughened and non-toughened systems. On one hand, the high-melt-flow PMMA substrate brought lower molecular weight segments, further leading to a decrease in the tensile properties of the substrate. However, when the replacement proportion was not high (ranging from 0 to 30%), this change was not significant. On the other hand, in terms of impact strength, there was almost no change in the non-toughened system, while in the toughened system, a similar trend to that shown in Figure 2 was observed. The impact strength increased from 2.54 to 3.04 kJ/m ²and then dropped back to 2.57 kJ/m ².

The difference in the high and low melt-flow ratio strategy in both toughened and non-toughened systems suggests that the toughening effect is likely due to the improved processability brought by a broader molecular chain range, which leads to more thorough plasticization and more uniform distribution of the toughening agent in the matrix. Essentially, this is a synergistic effect between the toughening agent and the matrix.

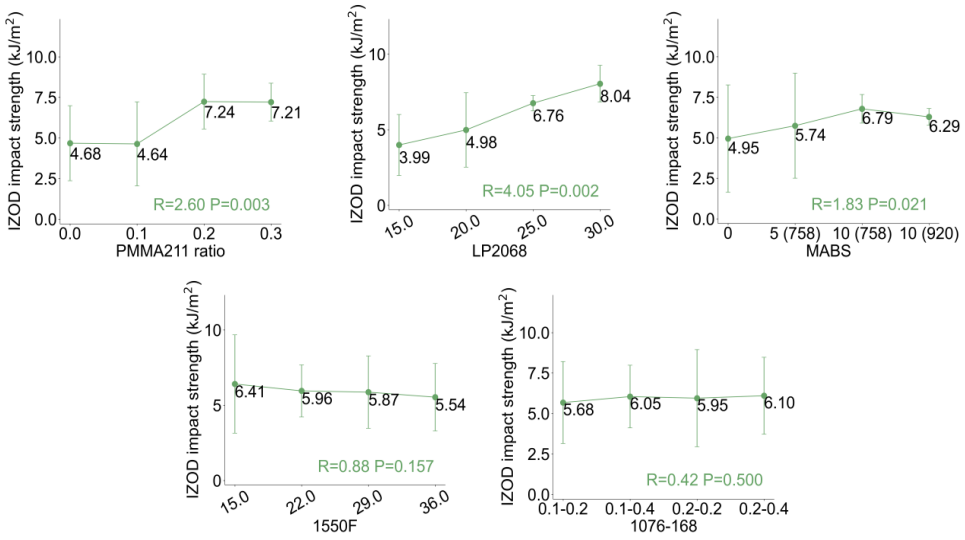

Figure 2 The formula vs. impact properties

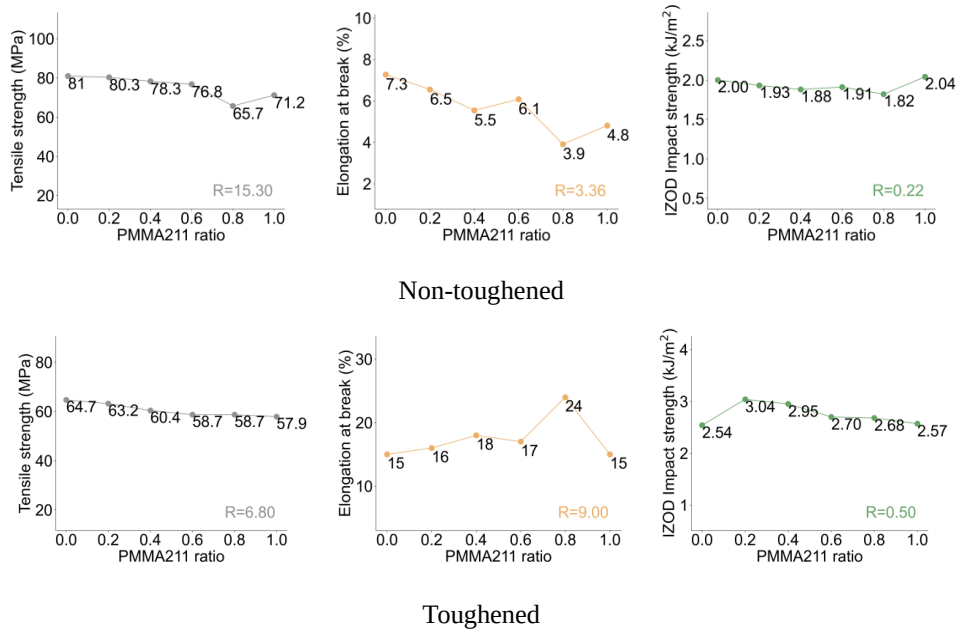

Figure 3 High MFR PMMA vs. mechanical properties in toughened/ normal materials systems

3.2 Appearance

In terms of appearance, the impact of each formulation system on the material's visual characteristics is relatively minor. Here, we use the Lab color model for analysis. The model evaluates color in three dimensions: L represents brightness, where a higher L value indicates a brighter color; a represents the red-green axis, where a higher a value indicates more red, and a lower a value indicates more green; b represents the yellow-blue axis, where a higher b value indicates more yellow, and a lower b value indicates more blue.

Regarding the L value, apart from the proportion of PMMA211, other components in the formulation have minimal effect on the L value. As described in Section 2.1, the proportion of PMMA211 not only affects the L value but also shows similar trends in all color dimensions, reflecting the same changes as observed in mechanical properties. This further suggests that the high and low melt-flow PMMA strategy is beneficial not only for toughening agents but also for improving the uniformity and dispersion of colorants.

Additionally, due to the influence of the inherent color of the materials, other components also have some effect on the color of the material system. LP2068 increases both the a and b values, which is attributed to the conjugated structure of the rubber phase's double bonds. The addition of MABS slightly reduces the a and

b values, as the conjugated structure of the styrene segments causes π-electron delocalization throughout the molecule, resulting in a slight blue shift. The addition of 1550F causes a significant decrease in the b value, which is due to the nitrogen-containing functional groups in the heat stabilizer.

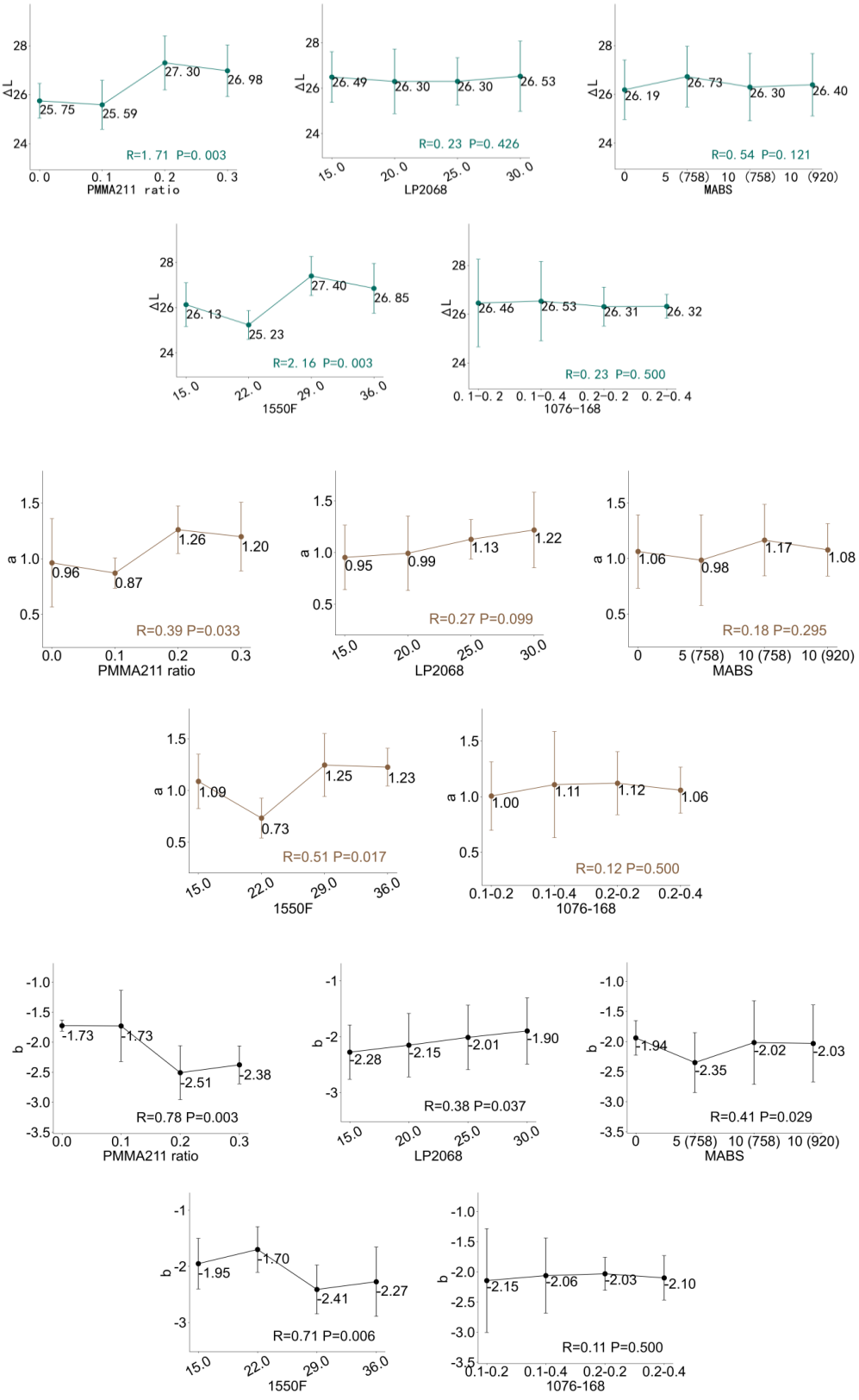

Figure 4 The formula vs. Color

3.3 Heat resisting properties

The heat resistance of the material system is evaluated using the HDT and VST. HDT focuses on assessing the material's serviceability under load, while VST is used to evaluate the material's thermal softening behavior and processing performance. The subtle differences between these two properties lead to slight variations in their response to the formulation system. LP2068 has a weak influence on both HDT and VST (P-values of 0.072 and 0.100, respectively). MABS has no effect on either property ($P > 0.1$). As a heat stabilizer, 1550F significantly influences both HDT and VST, which is expected (P-values of 0.002 and 0.026, respectively).

It is worth noting that when the amount of 1550F is between 15 and 22 parts, there is a plateau in the increase of VST, whereas HDT does not show this plateau. This is because, under load conditions, HDT reflects the overall thermal state of the material, and its failure depends on the overall failure of the specimen, directly related to the total content of the heat-resistant component. However, VST is measured by a needle penetration test, which is more sensitive to the surface condition of the material. Specifically, when the amount of 1550F increases from 15 to 22 parts, the VST shows little change, indicating that the distribution of 1550F within the matrix is not uniform. With fewer components, 1550F tends to accumulate on the surface rather than within the matrix. When the heat stabilizer is added in larger amounts, it affects the interior of the matrix, and the VST starts to rise gradually once the critical concentration is reached.

This distinction in heat resistance performance also suggests the mechanism of the PMMA211 proportion. The proportion of PMMA211 has no impact on HDT (P=0.500), but in the more surface-sensitive VST, a noticeable decrease occurs at a 0.2 ratio, which mirrors the trend observed in mechanical properties and color changes (P=0.040). Clearly, we can infer that for surface-sensitive properties, such as mechanical performance, surface color, and VST, the high-low melt-flow blend strategy has a significant impact. However, for properties less sensitive to surface conditions, such as HDT, this strategy has little effect. The reason might be that during the injection molding process, the differences in flowability cause high melt-flow components to be more likely to be affected by fountain flow, moving to the surface. These high-flow components often carry more functionalized ingredients, further influencing the material's surface condition. Based on these findings, guidance can be provided for designing the surface characteristics of formulation systems.

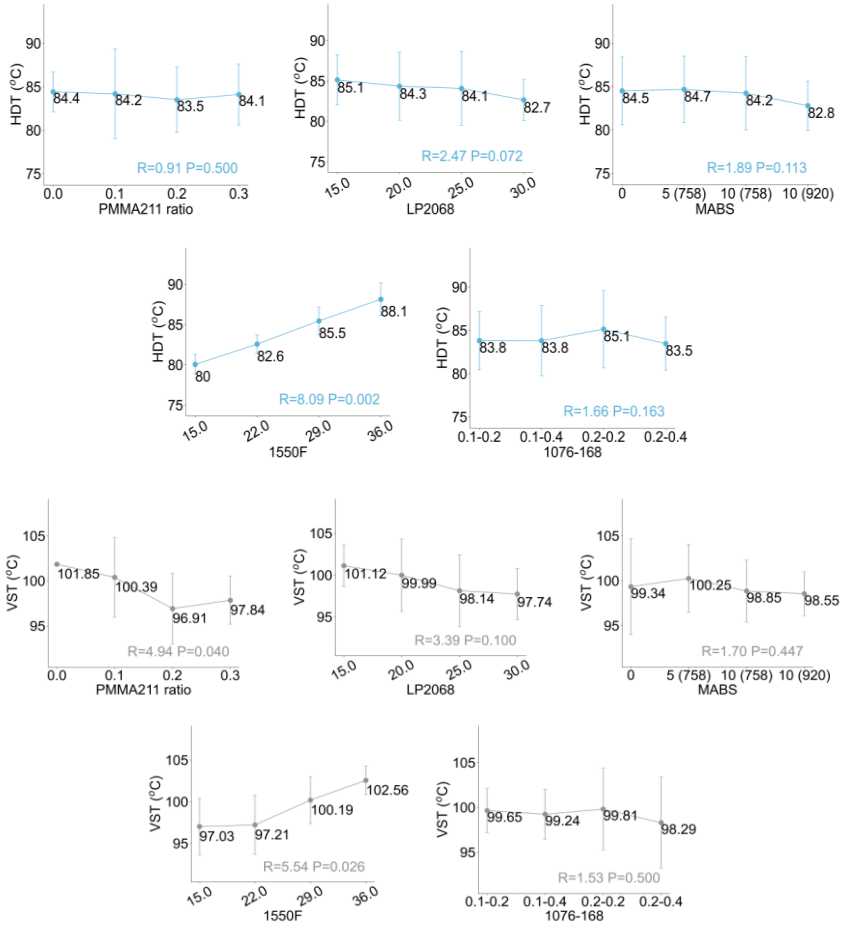

Figure 5 The formula vs. heat resistance properties

4 Conclusion

Orthogonal experiments were conducted to explore the impact of various formulation components on the overall performance of high-gloss black PMMA/ASA alloys. Hypothesis testing methods were used to assess the reliability of the experimental observations, and the following conclusions were drawn:

(1) Effect of Toughening Agents and Heat Stabilizers on Mechanical Properties: The introduction of toughening agents and heat stabilizers had different effects on the material's mechanical properties. LP2068, an ASA-based toughening agent, improved the impact strength by enhancing the uniformity of the rubber phase but caused a slight decrease in tensile performance. MABS 758 and MABS 920 had little impact on impact performance, but when added at higher ratios, they led to a decline in performance. The heat stabilizer 1550F had no effect on mechanical properties.

(2) Effect of PMMA211 on Mechanical Properties: PMMA211, as a high-flow material, had a significant impact on mechanical properties at a 20% ratio. While tensile performance slightly decreased, the impact strength significantly improved. Further verification experiments showed that PMMA211 improved the gradient distribution of the material, making the toughening agent distribution more uniform, which in turn enhanced toughness.

(3) Effect of Formulation on Appearance: The effect of the formulation on the material's appearance was minimal. Apart from the proportion of PMMA211, other components had little effect on the L value. The addition of PMMA211 aligned with the changes in mechanical properties, indicating that it not only improved toughness but also enhanced the uniformity and dispersion of colorants. Different additives had different effects on color: LP2068 increased both the a and b values, MABS lowered both a and b values, while 1550F significantly reduced the b value.

(4) Effect of Formulation on Heat Resistance: The formulation system had different effects on heat resistance, as measured by heat deflection temperature (HDT) and Vicat softening temperature (VST). LP2068 had a slight effect on both properties, while MABS had little to no effect. The heat stabilizer 1550F significantly improved both HDT and VST, particularly in the range of 15 to 22 parts, where a plateau in the VST was observed.

Effect of PMMA211 on Vicat Softening Temperature: PMMA211 had a notable effect on VST, especially at low ratios, causing a decrease in temperature. This change was consistent with the variations in mechanical properties and color. This phenomenon suggests a difference in the sensitivity of various properties to surface conditions. The high-low melt-flow blending strategy has a significant impact on surface properties but a minimal effect on intrinsic properties.

These findings highlight the importance of formulation components in tuning the surface and bulk properties of PMMA/ASA alloys, providing useful guidance for designing material systems with tailored performance characteristics.

References

[1] Wang X, Wu Y, Wen X, et al. Composite structure of Au film/PMMA grating coated with Au nanocubes for SERS substrate[J]. Optical Materials, 2021,121:111536.

[2] Darowicki K, Szocinski M, Schaefer K, et al. Investigation of morphological and electrical properties of the PMMA coating upon exposure to UV irradiation based on AFM studies[J]. Progress in Organic Coatings, 2011, 71(1):65-71.

[3] Forte M A, Silva R M, Tavares C J, et al. Is Poly(methyl methacrylate) (PMMA) a Suitable Substrate for ALD?: A Review[J]. Polymers, 2021, 13(8):1346.

[4] Lin Y, Liu Y, Zhang D, et al. Radiation resistance of poly(methyl methacrylate)/reduced graphene oxide nanocomposites fabricated through latex mixing and in situ reduction[J]. Chemical Engineering Journal, 2017, 315:516-526.

[5] Wang J F, Shi S Q, Liu Y Z, et al. Multiscale simulation of temperature- and pressure-dependent nonlinear dynamics of PMMA/CNT composite plates[J]. Nonlinear Dynamics, 2022, 109(3):1517-1550.

[6] Liu A, Huang R K, Meng T. Application of improved PMMA/ASA alloy materials in automotive exterior parts[J]. Shanghai Automobile, 2021(8):56-62.

[7] Meng Z, Sun Z Y, He F, et al. Advance in Research of ABS/PMMA Alloy with High-Gloss and Free-Spraying[J]. Engineering Plastics Application, 2016, 44(2):134-139.

[8] Xu J J, Zhou J H, Zhang Y H, et al. Study on Rubber-like ABS Toughened PMMA[J]. China Plastics Industry, 2023,51(12):43-47.

[9] Xu H Q, Li L P, Wang L. Preparation and Properties of High Toughness and High Gloss PMMA Composites[J]. Plastics Science and Technology, 2021, 49(4):39-42.

[10] Zhao Y, Liu S W, Zhang X L, et al. Characteristics and application of exterior spray-free high-gloss piano black materials[J]. Shanghai Automobile, 2018(3):51-55.

[11] Wang H, Zheng F H, Gu Z H, et al. Modification and process optimization of PMMA/ASA alloy materials[J]. China Plastics Industry, 2024,52(10):43-49.

[12] Yildirim F F, Sezer Hicyilmaz A, Yildirim K. The effects of the weathering methods on the properties of the ABS, ASA and PMMA polymers[J]. Polymer Testing, 2022,107:107484.

[13] Cocco D R, de Carvalho F P, Felisberti M I. Structures and morphologies of in situ polymerized blends of PMMA and ASA[J]. Journal of Applied Polymer Science, 2013,130(1):654-664.

[14] Lin M H, Zheng B, Guo J B, et al. Effects of SMA contents on properties of PMMA/ASA/SMA ternary alloy materials[J]. Engineering Plastics Application, 2024, 52(9):149-153.

[15] Liu W. Influences of ABS-g-MAH, PMMA and CNTs on Properties of PC/ASA Alloy [J]. Engineering Plastics Application, 2015, 43(10):32-35.

[16] Liu W Q. Design of Experiments [M]. Beijing: Tsinghua University Press, 2005.

Viser Technology Pte. Ltd.
Research and Application of Materials Science
DOI: 10.33142/rams.v6i2.14585

Research Article Open Access

Preparation of Slurry for Tape Casting of AlN Ceramic Substrates

Shen ZHANG, Yulong WANG, Zeyu WANG, Xue SHEN, Tengyu DU, Zhigang YANG*, Gang YU

Hebei Provincial Engineering Research Center of Metamaterial and Micro-device, School of Materials Science and Engineering, Shijiazhuang Tiedao University, Shijiazhuang, Hebei, 050043, China

*Corresponding Author: Zhigang YANG, Email: yangzhigang@stdu.edu.cn

Abstract

AlN ceramics are employed in a multitude of applications including large-scale integrated circuit (LIC) packaging substrates, electrostatic chucks, and transparent ceramics due to their excellent thermal conductivity, insulation and dielectric properties, robust corrosion resistance, and thermal expansion coefficient nearly identical to that of silicon. Tape casting is the optimal methodology for the fabrication of large-area, thin, and flat ceramics and components. However, the well-dispersed slurry with high solid loading is required to obtained the ceramic substrates with excellent properties by tape casting. Therefore, in this study, the effects of dispersant content, first ball milling time, binder content, and R value (plasticizer/binder) on the rheological properties of aluminum nitride slurry and casted sheet qualities were investigated. The results indicated that the optimal dispersant formulation was 1.1 wt%, the binder formulation was 2 wt%, the R value was 1.5, and the solid content was 60 wt%. The utilization of the aforementioned organic system enabled the preparation of AlN sheet exhibiting favorable morphology, high solid content, and flexibility.

Keywords: Tape casting; AlN; Slurry; Solid loading; Rheological property

1 Introduction

As the microelectronics and integrated circuit manufacturing field continue to higher integration, miniaturization, and higher reliability, the unit volume of the integrated block of electronic components work on the heat generated by a sharp increase in excessive heat emitting will inevitably produce irreversible damage to the electronic components on the substrate, or even lead to the burnt out of integrated block. Therefore, higher requirements on the thermal conductivity of electronic packaging substrates are put forwarded [1-2]. Researchers have attempted to address this challenge by exploring emerging materials such as AlN [3], SiC [4], BeO [5] and Si_3N_4 [6]. Among them, aluminum nitride (AlN) is an emerging ceramic material with a number of desirable properties, including high thermal conductivity, low dielectric constant and dielectric loss, high volume resistivity, good mechanical properties at room and elevated temperatures, and a coefficient of thermal expansion similar to that of silicon. Among these properties, the theoretical thermal conductivity of single-crystal AlN is up to 320 $W \cdot m^{-1} \cdot K^{-1}$, which is several times higher than that of Al_2O_3 as the traditional substrate material for electronic packages [7]. Additionally, AlN is chemically stable and nontoxic compared with the highly toxic nature of BeO, which has attracted a wide range of attention [8].

As the demand for electronic devices continues to evolve, the size and thickness of aluminum nitride substrates are becoming increasingly challenging. Consequently, the urgent need of a suitable casting method to accelerate the large-scale production of silicon nitride substrate materials has become apparent. Currently for the ceramic substrate casting preparation, there are mainly the following types, including dry pressure, injection, gel injection molding and tape casting [9]. The use of dry pressure molding and injection molding is only suitable for thickness greater than 1mm thick pieces. For large size, thin-walled pieces, these two methods are difficult to avoid uneven material density due to uneven casting pressure, so the parts in the sintering process is very easy to deformation, or even cracking, leading to low production efficiency. For gel injection of ceramic substrates, although it can solve the problem of deformation and cracking in the sintering process of the blank, the gel injection of the blank needs a slow drying and debinding process. Therefore, this method is inefficient and unsuitable for mass production.

Received on August 11, 2024; Accepted on September 15th, 2024

While tape casting is the best way to prepare large-area, thin, flat ceramics and components, it is more suitable for industrialized production owing to the degree of automation and high efficiency [10].

Tape casting is a forming process for preparing the ceramic substrates that offers numerous advantages. It is highly automated, requires minimal equipment, and can be operated continuously. Based on the type of solvent used, tape casting can be divided into two categories: water-based tape casting and organic-based tape casting[11]. The organic-based tape casting, also known as the traditional casting process, has been studied and applied for a longer period of time than the water-based system. Additionally, the application of ceramic substrate preparation has been relatively mature in the case of the organic-based tape casting system. The most commonly used solvents are toluene, xylene, ethanol, and trichloroethylene. Binary azeotropic solvents such as ethanol/toluene and ethanol/trichloroethylene are also commonly used in actual production [12]. The organic-based tape casting offers numerous advantages due to its compatibility, volatility, low latent heat of evaporation, low surface tension, and ability to prevent the hydration of ceramic powders. These advantages include a wide range of additives, fast solvent volatilization, short drying times, and the ability to obtain ceramic sheets with uniform structures, small green body defects, high strengths, and good flexibility.

In recent years, tape casting has been employed with increasing frequency in new research fields such as biomaterials, supercapacitors, and metals. The expansion of tape casting, especially in the aforementioned fields, will become one of the most promising areas of researches in the coming years [13]. The tape casting process was proposed by Howattg [14] in 1947. The process involves the mixing and stirring of ball-milled raw materials with binder and plasticizer to create a uniform slurry. And then a uniform thickness sheet is formed, which is discharged and sintered to obtain the final product. The quality of the casting sheet produced by tape casting is largely contingent upon the characteristics of the slurry. This is because the slurry comprises a multitude of components, including powders, solvents, plasticizers, binders, and dispersants. Any alteration to the composition of the slurry will result in a corresponding change in viscosity and physical rheology. Furthermore, the individual components of the slurry will also exert an influence on one another [15-16]. T. Chattier, E. Streicher, and colleagues [17-19] prepared AlN substrates using the casting method and investigated the effects of organic components (binders, plasticizers) and their dosages on slurry and green body machinery. W. Yin et al. [20, 22] conducted research on the preparation of AlN substrates by tape casting and discussed the primary factors influencing the viscosity of casting slurry. Their findings indicated that the viscosity of the slurry decreased as the solvent ratio increased, while it increased as the plasticizer ratio decreased. Yao et al. [23] conducted a study on the types of solvents, specifically xylene, butanol, isopropanol, n-propanol, and mixtures thereof (e.g., xylene + butanol, xylene + isopropanol, n-propanol + butanol, xylene + n-propanol, xylene + n-propanol). The results demonstrated that the mixed solvent xylene/isopropanol exhibited the most favorable wettability for AlN powder, while the slurry displayed the most optimal rheological properties, rendering it well-suited for tape casting. Liang et al. [24, 25] prepared an AlN ceramic slurry using absolute ethanol as a solvent, polyvinyl butyral ester (PVB) as a binder, oleic acid as a dispersant, and glycerol as a plasticizer. Huang et al. [26, 27] used an azeotropic mixture of dibutyl ketone and ethanol, while polyvinyl butyral ester (PVB) and butyl benzyl phthalate (BBP) were employed as binders and plasticizers, respectively, in the preparation of AlN slurries.

In addition to the individual formulations, the ball milling of the mixing process and the characterization of the fluid are also of great importance for the ceramic substrates. For systems with more wear-resistant components, the slurry is generally prepared by ball milling, and if there are special requirements, inert atmosphere or vacuum conditions may be required. However, vigorous agitation may disrupt the polymer chain of the binder, and both the binder and the dispersant need to be adsorbed on the surface of the ceramic powder, which is competitive [28]. Therefore, the ball milling process needs to be divided into two steps. The purpose of the first step is to make the agglomeration of powder particles open and fully dispersed, and only powder particles, solvents and dispersants are included in the slurry, so that the dispersant can be fully adsorbed on the surface of powder particles. The second step is to add other additives to the slurry ball mill with the aim of homogenizing the slurry composition. After the ball mill is completed, there will also be a small amount of air and residue in the slurry, which requires degassing and filtration before it can be used for subsequent molding.

Fluids can be divided into several categories according to their viscosity as a function of the shear rate [29]. The viscosity of pseudoplastic fluid decreases with the increase of shear rate, and the viscosity of plastic fluid increases with the increase of shear rate. In order to keep the thickness of the cast film with a smooth surface and a homogeneous microstructure, the slurry used for tape casting should be a pseudoplastic fluid. After the casting, the scraper will exert a shear stress on the slurry, and the viscosity of the slurry decreases under the action of shear stress, so that a uniform film can be formed on the substrate. When the scraper passes through the slurry, the shear stress disappears, the viscosity rises to the initial state, and the fluidity of the slurry becomes poor. And the composition of the casting film is kept uniform. In order to avoid the slurry remaining in a low viscosity state for a long time after the scraper has passed, the slurry should

not be thixotropic, i.e., the viscosity increases immediately after the stress is withdrawn.

The composition of casting slurries includes the used raw powders, solvents, dispersants, binders, plasticizers, and other additives. Each of these components exerts a important influence on the performance of the slurry, and the interactions among the individual components within the slurry are also significant. The complexity presents a significant challenge to the study of tape casting slurries. Consequently, it is essential to conduct further in-depth research and exploration of tape casting technology. In this study, aluminum nitride was used as the main raw material, and toluene and anhydrous ethanol were used as the binary solvents. Toluene was able to dissolve all the solutes and reduced the drying speed, which could reduce the volatilization, decrease the viscosity and increase the solid content. Fish oil, polyvinyl butyral and dibutyl phthalate were used as dispersants, binders and plasticizers, respectively, for the preparation of aluminum nitride ceramic substrates.

2 Experimental

2.1 Starting materials

Aluminum nitride powders (average particle size: 1μm), calcium fluoride powder and yttrium oxide powder were used as sintering additives, and toluene and absolute ethanol were selected as solvent systems. Herring oil (Cas:8002-5-4,Shanghai Macklin Biochemical Co., Ltd., China) was used as a dispersant, and polyvinyl butyral (PVB, Cas:63148-65-2, Shanghai Macklin Biochemical Co., Ltd., China) and dibutyl phthalate (DBP, Cas:84-74-2,Shanghai Macklin Biochemical Co., Ltd., China) were used as binders and plasticizers, respectively.

2.2 Experimental process

The preparation method of AlN slurries was as follows. Firstly, mixed powders were prepared according to the molar ratio of AlN, CaF_2 and Y_2O_3 of 92:3:5. Toluene and absolute ethanol were used to prepare non-aqueous solvents according to the mass ratio of 1/1. Then, the mixed powders were added into the solvent, and they were ball-milled for 1-4 h. Dispersant, binder (PVB) and plasticizer (DBP) were added to further be milled for 12 h. The height of the scraper was controlled at 200 ～ 300 μm. The casting speed was 0.3 $cm \cdot s^{-1}$. The tape sheets were dried at 27.5 ℃ for 12 h to obtain the final samples.

2.3 Characterization

The viscosity of the slurries was quantified using a viscometer (NDJ-8S), and the dispersibility of the slurries was evaluated through the sedimentation method. Prior to the addition of the binder PVB, it is necessary to prepare a precast colloid with toluene and absolute ethanol solvent in advance, which show a colorless, transparent, and clear solution at 90 ℃ in an oil bath before using.

3 Results & Discussion

In the tape casting process, the viscosity of the slurries is a crucial parameter influencing the quality of the tape sheet. And it, as an essential rheological property, is a quantifiable characteristic that reflects the friction or viscosity within the slurry [30]. The viscosities are affected synergistically by multiple factors, including powder particle properties, slurry composition, mixed ball mill dispersion time, temperature, etc. The R-value (ratio of plasticizer to binder) is an indicator that reflecting the effect of these factors on the dispersion or viscosity of AlN slurries.

3.1 Effect of dispersant content on the properties of AlN slurries

Figure 1 shows the viscosity of the slurries with different contents of dispersant (0～2.6 wt%) after the first ball milling for 3h, in which the solid content of slurries is 57.8 wt%.The viscosity of slurries decreases with the increase of dispersant content. Since the dispersant is adsorbed on the surface of the particles, the spatial stability hinders the agglomeration among the particles and enhances the fluidity of the slurries [30]. As the dispersant content increases from 0 to 2.6 wt%, the viscosity of slurries first decreases and then increases.

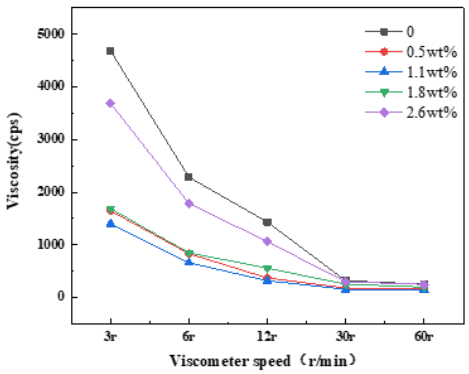

Figure 1 Effect of dispersant content on suspension viscosity

When the content is 1.1wt%, the viscosity has a lowest value. It is found that the excess dispersant content undergoes a cross-linking reaction among the particles, reducing the dispersion of the particles[31]. Therefore, it is determined that 1.1 wt% dispersant is the optimal content.

3.2 Effect of ball milling time on the properties of AlN slurries

Figure 2 shows the viscosity of AlN slurries with different ball milling time at the dispersant content of 1.1wt%. It is found that the viscosity of the slurries

increases with the increase of ball milling time. The viscosity of the slurries increases because of the volatilization of the solvent in 0～4h. Meanwhile, it is seen that the viscosity of the slurries decreases with the increase of the shear rate, meaning that the prepared slurries exhibit typical pseudoplastic fluid characteristics[32]. In the tape casting process, the scraper function is like a shearing process, and the shear thinning characteristics of the pseudoplastic fluid are very advantageous in the tape casting process. When the slurry passes through the scraper, the viscosity becomes small, which is conducive to the slurry passing through the scrape. After that, the shear rate becomes small and the viscosity of the slurry increases rapidly, which is beneficial for the forming of taped green sheets.

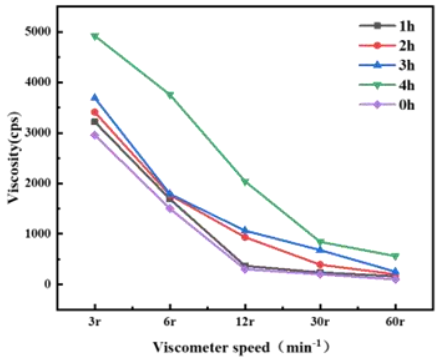

Figure 2 Changes in viscosity of slurries at different ball milling times

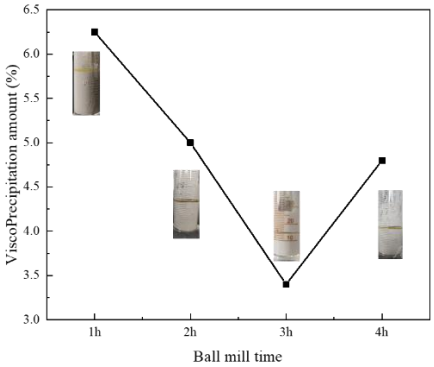

Figure 3 Comparison in the height of the upper precipitated liquid after standing for 1 h at different ball milling times

As shown in Figure 3, when the rotational speed of the planetary mill is 300r/min, as ball milling time increases from 1h to 3h, the height of the upper yellow liquid after resting 1h gradually decreases. At ball milling of 3h, the upper yellow liquid after resting 1h is least height. However, with the further increase of ball milling time, the precipitate height increases. These results show that too long ball milling time causes the instability of slurries. Therefore, appropriate ball milling time is required to obtain slurries with high performance.

3.3 Effect of binder content on AlN slurries w

In the manufacturing of ceramic green sheets, binders are probably the most important additives in the overall system [31].

Fig. 4 shows the viscosity variation of AlN slurries with different binder content, in which the solid content of the slurry is 46 wt.%, the dispersant content is 1.1 wt.%, the binder content ranges from (1.2～3.6) wt.%, and the mass ratio of plasticizer to binder is 1. With the increase of binder content, the viscosity of the slurry increases gradually. In order to obtain the maximum solid content, the binder should be selected as little as possible under the condition of maintaining a certain strength. Meanwhile, it is found that when the binder content is located at 1～1.5wt%, it has been demonstrated that the formed film exists micropores. When the binder content is 2.5wt%, the surface of the formed film is smooth. And when the binder content is 3.7wt%, the formed film is not easy to control the thickness, meanwhile, the high viscosity is not conducive to the subsequent increase of solid content. Therefore, the binder content of 2wt% is used for the preparation of slurries.

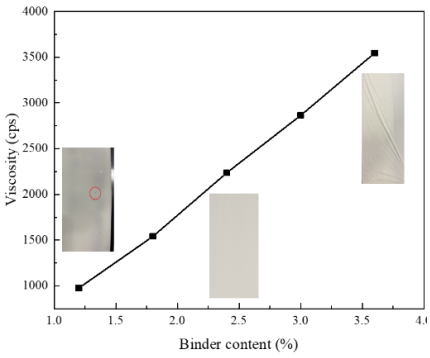

Figure 4 Effect of binder content on viscosity of AlN slurries

3.4 Effect of R-value on properties of AlN slurries

The R-value, i.e., the ratio of plasticizer to binder, is an important factor influencing the rheological properties of cast slurry and the properties of cast green materials. both of which

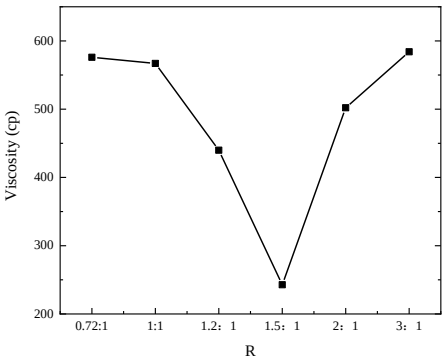

Figure 5 Effect of R value on the viscosity of AlN slurries

Make the cast sheets more flexible. In Figure 5, at the solid loading of 43wt%, binder content of 2wt%, and dispersant content of 1.1wt%, with the increase of R value from 0.72 to 1.5, the viscosity of slurries gradually

decreases. When the R value is 1.5, the lowest viscosity of slurries is obtained. With further increase of R, oppositely, the viscosity increases.

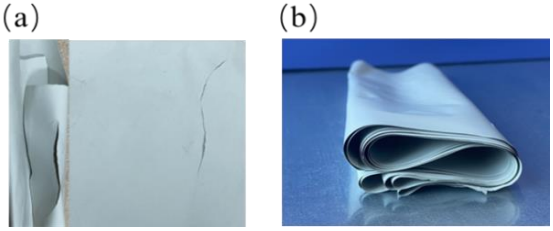

Figure 6 The photo images of formed tape sheets at the R value of (a) 0.72 and 1, (b) 1.5

In Figure 6a, when the R value is 0.72 and 1, the flexibility of the formed tape sheet is insufficient, causing it susceptible to cracking during the drying process. An appropriate R-value can reduce the viscosity of the slurry, thereby facilitating the forming of desired flexibility. As illustrated in Figure 6b, at an R-value of 1.5, the AlN green sheets exhibits optimal flexibility and a smooth surface. Accordingly, the R-value of 1.5 is selected for the subsequent experiments.3.5 Effect of solids content on rheological properties of AlN slurries

The solid content of AlN slurries is crucial for the preparation of high density AlN ceramics. Therefore, it is necessary to prepare the slurries with high solid content as much as possible while ensuring the dispersion stability and low viscosity. As shown in Fig. 7, when the solid loading increases from 42 to 57wt.%, the viscosity of the slurry increases gradually. However, when the solid phase increases from 57 to 62wt.%, the viscosity value increase sharply, and the fluidity of the slurry become weak, which can not form the green film. The higher the solid content of the AlN slurry, higher density of the AlN ceramics can be obtained. Therefore, AlN, slurries with solid loading of 60wt.% are selected to prepare the AlN ceramics.

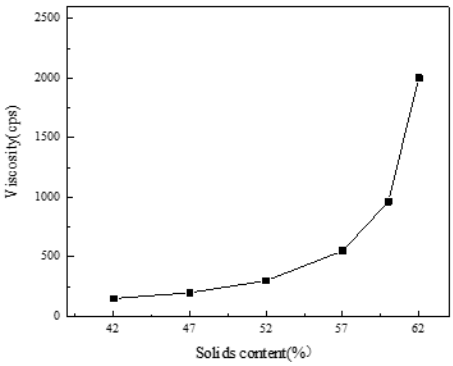

Figure 7 Effect of solids content on viscosity of AlN slurries

4 conclusions

In this paper, the effects of the dispersant, ball milling time, binder, plasticizer, and solid loading on the properties of AlN ceramic slurries were researched. A 1.1wt% of fish oil as a dispersant for the slurry could yield a dispersion of AlN with good dispersion stability and low viscosity. The ball milling time of 3h was beneficial for the AlN slurry with best dispersion and low viscosity. Additionally, the binder content of 2wt% was used to prepare AlN slurries with high solid loading. Meanwhile, the viscosity of the slurry decreases first and then increases with the increase of the R value (plasticizer/binder), and the viscosity of the slurry reaches the lowest value when R=1.5. Finally, the slurries with the solid loading of 60wt% were chose to prepared the AlN ceramic sheets in future research.

References

[1] R. Plieninger, M. Dittes, K. Pressel. Modern IC packaging trends and their reliability implications[J]. Microelectronics Reliability, 2006,46(9):1868-1873.

[2] J. Baffett. Electronic systems packaging: future reliability challenges[J]. Microelectronics Reliability, 1998(38):1277-1286.

[3] Hongjun N, Wei N, Libin M, et al.Research status and development trend of preparation technologies for high thermal conductivity AlN ceramic substrates [J]. Modern Chemical Industry, 2017, 37(07): 45-48.

[4] Eom J H, Seo Y K, Kim Y W. Mechanical and thermal properties of pressureless sintered silicon carbide ceramics with Alumina-Yttria-Calcia[J]. Journal of the American Ceramic Society, 2016,99(5):1735-1741.

[5] Akishin P G, Turnaev K S, Vaispapir Y V, et al. Composition of beryllium oxide ceramics [J]. Refractories and Industrial Ceramics, 2011,51(5):377-381.

[6] Zhou Y, Hyuga H, Kusano D, et al. A Tough Silicon Nitride Ceramic with High Thermal Conductivity[J]. Advanced Materials, 2011,23(39):45-48.

[7] Chung L S, Tsai I T, Huang C S. High Thermal Conductivity Ceramics from Combustion Synthesized AlN Powder through Microwave Sintering and Reheating [J]. International Journal of Self-Propagating High-Temperature Synthesis, 2012,21(1):45-50.

[8] Sunil C Joshi, Y.C Lam, F.Y.C Boey & A.I.Y Tok. Power law fluids and Bingham plastics flow models for ceramic tape casting[J]. Journal of Materials Processing Tech, 2002(1-3),215-225.

[9] Alain D. Moriana & Shujun Zhang. Lead-free textured piezoceramics using tape casting: A review[J]. Journal of Materiomics, 2018(4):277-303.

[10] Qingdong H, Xudong L, Zhipeng X, et al. Development of the Environmental Friendly Non-Aqueous Tape Casting Process for High-Quality Si_3N_4 Ceramic Substrates[J]. IOP Conference Series: Materials Science and Engineering, 2019(678):012042-012042.

[11] Zhao Pengbo, Zhao Xiaotong & Wang Hailong. Processing and Properties of Laminated ZrB_2-Mo_5SiB_2 Ceramic Composites Fabricated by Tape Casting and Hot Pressing Sintering[J]. IOP Conference Series: Materials Science and

Engineering, 2019(10):012072-012072.
[12] MORENO R. The role of slip additives in tape-casting technology. I: Solvents and dispersants[J]. American Ceramic Society Bulletin, 1992,71(10),1521−1531.
[13] Hou Qingdong, Luo Xudong, Xie Zhipeng, et al. Development of the Environmental Friendly Non-Aqueous Tape Casting Process for High-Quality Si_3N_4 Ceramic Substrates[J]. IOP Conference Series: Materials Science and Engineering, 2019(15):012042-012042.
[14] Jabbari M., Bulatova R., Tok A. I. Y., et al. Ceramic tape casting:A review of current methods and trends with emphasis on rheological behaviour and flow analysis[J]. Mater.Sci.Eng.B, 2016(212):39-61.
[15] MESSING G L, FULLER E R, HAUSNER H. Ceramic powder science[M]. Columbus: American Ceramic Society, 1988.
[16] ZHOU Jian-min, WANG Ya-dong, WANG Shuang-xi et al. Tape Casting Process for Fabricating Electronic Ceramic Substrate [J]. Bulletin of the Chinese Ceramic Society, 2010,29(5):1114−1118.
[17] DESCAMPSM, MOREAU G, MASCART M, et al. Processing of aluminium nitride powder by the tape-casting process[J]. Journal of the European Ceramic Society, 1994,13(3):221-228.
[18] STREICHER E, CHARTIER T, BOCH P. Influence of organic components on properties of tape-cast aluminum nitride substrates [J]. Ceramics International, 1990,16(4):247-252.
[19] CHARTIER T, STREIHER E, BOCH P. Preparation and characterization of tape cast aluminum nitride substrates[J]. Journal of the European Ceramic Society, 1992,9(3):231-242.
[20] WU Y, ZHOU H P, LIAO W G. Process of casting to make AlN ceramic substrates[J]. Electronic Components and Materials, 1996,15(1):20-23.
[21] WU Y, LIAO W G. High thermal conductivity AlN substrates for low-temperature sintering were prepared by casting method[J]. Journal of Inorganic Materials, 1996,11(4):606-610.
[22] WU Y, LIAO W G. Study on the viscosity of cast slurry for AlN substrate[J]. Electronic Components and Materials, 1996,15(6):21-24.
[23] YAO Y J, QIU T. Study of cast forming pastes for aluminum nitride substrates[J]. Journal of Materials Science and Engineering, 2006,24(3):104-106.
[24] CAO J. Study on the preparation of AlN ceramic substrates by casting method[J]. Journal of Inorganic Materials, 2001,16(2):269-276.
[25] Liang Guangchuan, Liang Jinsheng, Liang Xiuhong, et al. A method for manufacturing aluminum nitride ceramic substrate with high thermal conductivity for integrated circuits using tape casting[P]. Tianjin:CN98125129.3,2002-07-03.
[26] DONG H, ZHAOBO T, WEI C, et al. Effects of Y_2O_3 and yttrium aluminates as sintering additives on the thermal conductivity of AlN ceramic substrates[J]. Ceramics International, 2018,44(16):20556-20559.
[27] HUANG D, LIU Z, HARRIS J, et al. High thermal conductive AlN substrate for heat dissipation in high-power LEDs [J]. Ceramics International, 2018,45(1):1412-1415.
[28] HESSELINK, F. Th. Theory of the stabilization of dispersions by adsorbed macromolecules. I. Statistics of the change of some configurational properties of adsorbed macromolecules on the approach of an impenetrable interface[J]. The Journal of Physical Chemistry, 1971,75(1):65-71
[29] Chartier T., Merle D., Besson J.L. Laminar ceramic composites[J]. J.Eur.Ceram.Soc. 1995,15(2):101–107.
[30] Struble L, Sun G K. Viscosity of Portland cement paste as a function of concentration[J]. Advanced Cement Based Materials, 1995,2(2):62-69.
[31] Bitterlich B., Jürgen G.H. Aqueous tape casting of silicon nitride[J]. J.Eur.Ceram.Soc, 2002,22(13):242 7-2434.
[32] F. P, M. A. A . Steady-state simulation of the film-casting process for Newtonian and viscoelastic fluids[J]. Journal of Non-Newtonian Fluid Mechanics, 2023(322):33-36.

Viser Technology Pte. Ltd.
Research and Application of Materials Science
DOI: 10.33142/rams.v6i2.14586

Research Article Open Access

Surface and Interfacial Bonding with Epoxy Adhesive of Flame Retardent Acrylonitrile-Butadiene-Styrene Copolymers (ABS)

Lulin WANG, Yeming XIAN, Juean DENG, Jianxin HAO, Yuanzeng HAO, Wentao YU*

Guangzhou Super-Dragon Engineering Plastics Co. Ltd, Guangzhou, Guangdong, 510945, China

***Corresponding Author:** Wentao YU, E-mail: wave_railgun@163.com*

Abstract

Flame retardants were widely used to expanding applications of acrylonitrile-butadiene-styrene copolymers (ABS) to daily life, heat generation, and energy storage. However, effect of flame retardants on surface properties such as wettability, adhesion and epoxy resins affinity were few studied. In this work, surface, epoxy resin adhesive as well as curing condition of ABS/ FRABS were investigated systematically. Results showed that processing temperature changing the ABS-flame retardant mixing from liquid-solid to liquid-liquid and affect the interface shear bonding strength. Best processing of rebonded ABS samples were curing under 0.7 kg, in 60 ℃ for 2 hours. Adhesion of epoxy to ABS/ FRABS remained for 90 days under soaking in 40 wt% sulfuric acid, showing the obvious chemical stability.

***Keywords:** ABS; Flame retardant; Epoxy resin; Surface adhesion*

1 Introduction

As a typical common amorphous plastics, acrylonitrile-butadiene-styrene co-polymers (ABS) was widely-used in automobile, electrical industry, decoration, biology, and aerospace as substrate or sealing materials, which requires tough and robust bonding with heterogeneous materials, including polymethyl methacrylate (PMMA)[1], nylon[2], epoxy resin, nickel[3], silver[4], copper[5], and so on. However, almost all ABS the researches were neat ABS containing few additives. For industrial application, ABS was not fabricated independently, but used as a major component mixed with several chemical agents especially flame retardants, fillers, or other polymers via solution or melting blending. One of the most important components was flame retardant. Flame retardant overcome the drawbacks ABS's burning behaviors to ensure the safety and reduce the risk of fire accidents. Recently, conventional flame retardant like Br-Sb_2O_3 flame retardant systems [6-8] and halogen-free flame retardant systems[9-12] were developed. For combining high properties of ABS, such as toughness, fluidity, heat stability, weatherability, stress crack resistance and heat-sealing adaptability, with flame retardancy, Br-Sb_2O_3 flame retardants were applied for ABS generally.

Therefore, the application of flame retardant ABS (FRABS) was expanded to battery as structural part, which required secondary sealing materials. Between ABS and secondary sealing materials are epoxy resins adhesive usually. As the consequence, the robustness of the battery is linked with the adhesion of ABS-epoxy adhesive and secondary sealing materials-epoxy adhesive intensively. Worse adhesion induces leakage of battery contents or contamination under real circumstances including collision and vibration. However, flame retardants affect the surface condition deeply. ABS commercially adaptable flame retardant contains Br element and aromatic/ heteroaromatic ring mainly. Nowadays, few works evaluated the effect of flame retardant onto the ABS surface, which limited the further applications. In this work, surface, epoxy resin adhesive as well as curing condition of ABS/ FRABS were investigated systematically.

2 Experimental

2.1 Materials

ABS (PA-757) were purchased from Qimei Co. Ltd., China (Taiwan). Tetrabromobisphenol A (FR-1524), was purchased from Dead Sea Mromine Co. Ltd.. Bromotriazine (FR-245) and Decabromodiphenylethane (DBDPE, 4010) were purchased from Albemarle Corporation, U.S.A.. Brominated Epoxy Resin

Received on September 6th, 2024; Accepted on October 16, 2024

(CXB-714C) was purchased from Woojin Copolymer Co., Ltd.. South Korea. Antioxidant 1010 and 168 were purchased from Ciba Specialty Chemicals, Co., Ltd.. Switzerland. Lubricant (EBS) were purchased from Nanjing Guochen Chemical Co., Ltd. China. Mineral oil (O-WO1) were purchased by Liaoning Oxiranchem Inc. China. Anti-dripping agent SN80-SA7 were purchased by Guangzhou Entropy Polymer Technology Co., Ltd.. ABS powder with high rubber (HR-181) were purchased from Kumho, Korea. Sb_2O_3 (S-05N) were purchased from Yunnan Muli Antimony Industry Co., Ltd. China. Epoxy adhesives (5212B) and the hardeners (5212H) were purchased from First Li-Bond (Wuxi), Co. Ltd., China.

ABS and FRABS were prepared via injection molding. First, 0.1 phr of antioxidant 1010, 0.2 phr of antioxidant 168, 0.3 phr of lubricants EBS-50, 0.2 phr of anti-dipping agent SN3306, 0.2 phr white oil were mixed by high speed mixer (Keda Machinery, China) and added with the others according to Table1 into a twin screw extruder (SHJ-30, Nanjing Ruiya, China) with the temperature between 180 to 210 ℃, main engine speed of 1020 r/min, feeding speed of 400 r/min. As-received ABS/ FRABS pellets were dried for 4 hours at 80 ℃. Standard testing samples were formed by an injection molding machine (Un90SK II-V, Yizumi, China).

2.3 Characterizations

Tensile strengths, bending properties, Izod impact strengths were tested according to GB/T 1040—2006, GB/T 9341—2006, GB/T 1843—2008, respectively.

Besides, the adhesive strength were conducted via a self-developed method: standard tensile samples were molded according to GB/T 1040.2-2022, with the thickness of 3.2 mm, the width of 12.7 mm in narrow part and 19.0 mm in wide part, the gauge length of 60 mm and the total length of 220 mm.

Evaluation of adhesive strength were conducted as below shown in Figure 1: After molding, ABS/ FRABS tensile samples were cut into two parts evenly and epoxy adhesives were coated onto the surface near the cutting sides. The two parts were rejointed and cured under heating. The prepared samples were tested with tensile strength (fracture). The adhesive strengths were defined as the tensile strength/ coated area. Contact angle were tested by a an optical contact angle meter (OCA35, Dataphysics) with water and diiodomethane. Besides, critical surface tensions were calculated by extrapolation method based on the contact angle results.

Anti-chemical properties were conducted as below: The re-bonded FRABS were cured under the load of 0.5 kg, after curing in an oven at 60 ℃ for 2 hours. After placing into standard environment 24 hours, the samples were transferred into a vessel containing 40% sulfuric acid solution. Then the vessel was placed in an oven at different temperatures for different aging time. A tensile test (5% tensile rate) was carried out after being cleaned and placed for 24 hours.

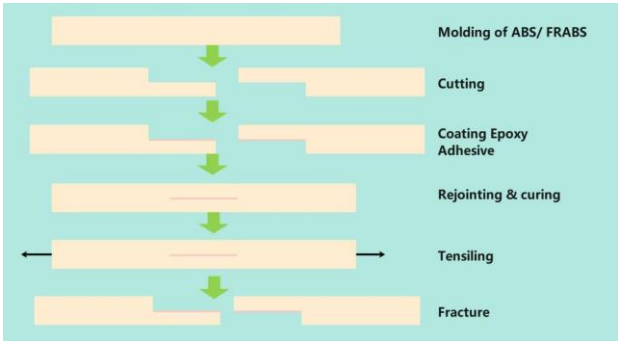

Figure 1 Illustration of the evaluation of adhesive strength

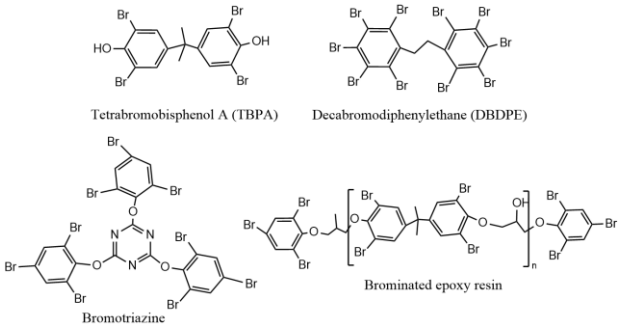

Figure 2 Chemical structure of flame retardants used in this work

Table 1 Major formula of prepared samples

	Content/ phr						
	ABS PA-757	HR-181	FR-1524	FR-714C	FR-245	FR-4010	S-05N
ABS	90	10					
TBPA	65	10	20				5
Br-Epoxy	65	10		20			5
Br-Triazine	65	10			20		5
10-Br	65	10				20	5

3 Results and Discussions

3.1 Surface adhesion of ABS/ FRABS onto epoxy adhesive

As Figure 3a showed, flame retardants affected the interfacial bonding deeply, for the interfacial shear binding strength of groups of Br-Triazine and 10-Br increased increased obviously white TBPA and Br-Epoxy not. Segments of ABS including were with middle polarities and providing hydrophilicity as well as adhesive capability, which were inferior to oxygen groups. There was a probable reason: Hydroxyl groups of TBPA and Br-epoxy existed. However, surface wettabilities and critical surface tensions displayed in Figure 3b showed that there were alomst no obvious differences between different FRABS; Therefore, the surface functional groups were not the dominant factors.

Another explanation was the gap of melting points of the four flame retardants: Br-epoxy (100～110 ℃ liquid in 200 ℃), TBPA (178～181 ℃ (Br-epoxy, liquid in 200 ℃), Br-Triazine (220～230 ℃, solid in 200 ℃), 10-Br (357 ℃, solid in 200 ℃), which resulted in the transformation of ABS-flame retardant surfaces from liquid-liquid to liquid-solid. As for ABS matrix, liquid-liquid interfaces improved the disaggregation and the effect of two-screw shearing undoubtedly. However, for surface, liquid-liquid interfaces formed smoother surface and molecular chains with higher density. What's more, liquid phase flame retardant occupied the space of electron-rich groups such as -C=C-, -Ar, and -C≡N. In another word, the introductions of Br flame retardant represented that the hydrogen atoms were replaced by the electrophilic bromine atoms, which were harmful for the adhesion from epoxy resins because of weaker Van der Waals force.

For solid-liquid surfaces, because of the internal force, the stress from tougher fillers promoted the relaxation of surface molecular segments. Many researches reported that introduced of fillers lowered the interfacial adhesion. Sb_2O_3 was existed in all the FRABS in this work, however, effect of Sb_2O_3 onto surfaces were limited by the differential of chemical structures between Sb_2O_3 and matrix. The differences of liquid-liquid and liquid-solid were also effected on the mechanical properties. As Figure 3c showed, toughness of FRABS with liquid-solid mixing were weak as the result of segregation and stress concentration. Therefore, for future researches, to realize liquid-solid mixing and avoid large segregation simultaneously were urgent to be solved.

3.2 Curing process

Curing of epoxy is a volume shrinking stage, which induces crosslinking and liquid-solid transformations. As a result, although epoxy net chains can infiltrate ABS/ FRABS, volume shrinking improved the separation of molecular chains from epoxy-ABS/ FRABS surfaces. Thus, there were a conflict tendency: epoxy with higher crosslinking density gave the epoxy resins higher strength but lowered the interfacial shearing strength and vice versa. On the other hand, applying pressures during all the curing stage were a common solution to improve interfacial bonding as well. Density of contact surface of epoxy net chains and ABS net chains was improved, vapor was extruded, separation tendency was restricted because of the pressures. Nevertheless, pressures will extruded epoxy, lowered the thickness of adhesive layers, and restricted the motion of epoxy resins net chains. Therefore, this section would discuss the optimal processes.

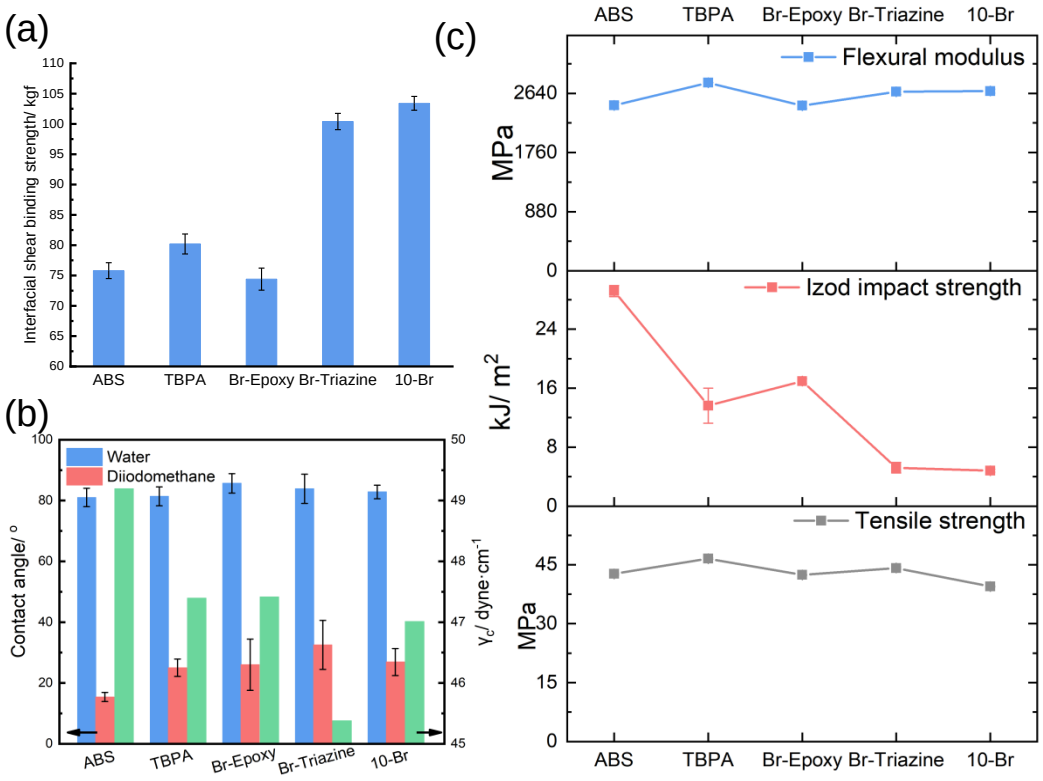

Figure 3 (a) Interfacial shear binding strength (Cured at 60 ℃ for 2 hours under 0.7 kg loading), (b) Water/ diiodomethane contact angle and critical surface tension (γc) (c) Mechanical properties of different ABS/ FRABS

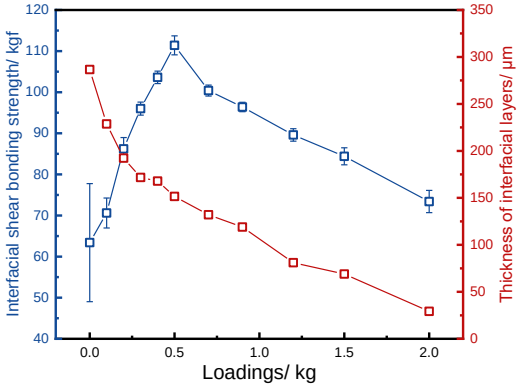

Figure 4 Interfacial shear binding strength and adhesive thickness of different curing load (Cured at 60 ℃ for 2 hours)

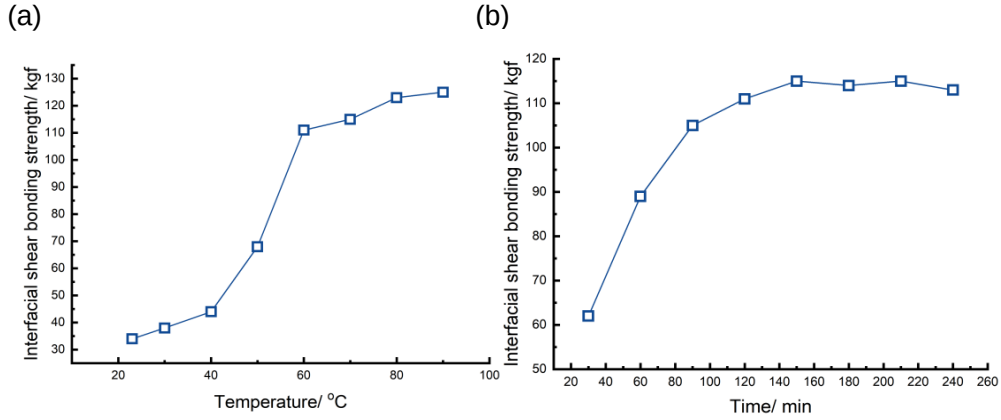

Figure 5 Interfacial tensile and shear binding strength of different curing (a) temperature and (b) time (Cured under 0.7 kg loading)

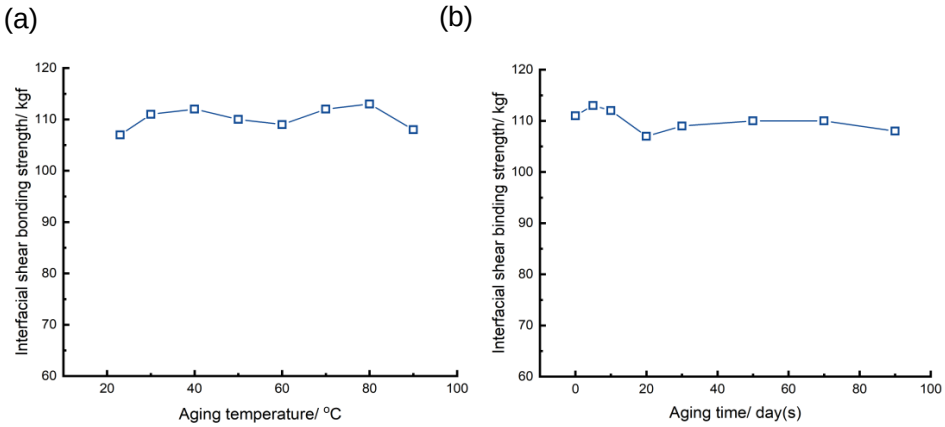

Figure 6 Interfacial tensile and shear bonding strength of different temperature and time under 40% sulfuric acid solution (Cured at 60 ℃ for 2 hours under 0.7 kg loading)

Figure 4 showed the relationships between loading, interfacial shear bonding strength and thickness of interfacial layers. As foresight, the increasements of loadings lowered the thickness of interfacial layers, but the tendency was separated by 0.5 kg into two stages: rapid declining and slow declining. Simultaneously, the interfacial shear bonding strength reached to the peak of 111.4 kgf. Rapid declining stages were attributed to the improvements of contact volumes of epoxy resins and ABS chains, increasing of epoxy crosslinking density and extruded of vapors. In slow declining stage, the extrusion of epoxy resin was the dominant factor.

3.3 Properties in acid environment

Anti-chemicals was the key properties for further applications, like batteries and sealing materials. All the samples were dipped into 40% sulfuric acid with different time and temperature. The results showed that the adhesion was stable even under 60 ℃ or for 90 days.

4 Conclusion

Adhesions of epoxy resins to ABS/ FRABS were evaluated and solid states flame retardant under processing temperature improved the interface shear bonding strength. The surface wettability were not influnced by flame retardant, but the surface distributinons of flame retardant were. Interface shear bonding strength and thickness of epoxy resins were related with pressure, curing time and temperature and the best processing were curing under 0.7 kg, in 60 ℃ for 2 hours. Adhesion remained for 90 days under soaking in 40 wt% sulfuric acid.

References

[1] Kahraman M V, Akdemir Z S, Kartal I, et al. Preparation of fluorine containing hybrid coatings: investigation of coating performance onto ABS and PMMA substrates [J]. Polym. Advan. Technol, 2011(22):981-986.

[2] Abbott A C, Tandon G P, Bradford R L, et al. Process-structure-property effects on ABS bond strength in fused filament fabrication [J]. Additive Manufacturing, 2018(19):29-38.

[3] Zhang H, Kang Z, Sang J, et al. Surface metallization of ABS plastics for nickel plating by molecules grafted method [J]. Surface and Coatings Technology, 2018(340):8-16.

[4] Chen D, Zhang Y, Bessho T, et al. Ag films with enhanced adhesion fabricated by solution process for solar reflector applications [J]. Sol. Energ. Mat. Sol. C, 2016(151):154-161.

[5] Han X, Wang G, He Y, et al. Surface modification of ABS with Cr6+ free etching process in the electroless plating [J]. J. Adhes. Sci. Technol, 2018(32):2481-2493.

[6] Altarawneh M, Saeed A, Al-Harahsheh M, et al. Thermal decomposition of brominated flame retardants (BFRs): Products and mechanisms [J]. Prog. Energ. Combust, 2019(70):212-259.

[7] Huang G, Huo S, Xu X, et al. Realizing simultaneous improvements in mechanical strength, flame retardancy and smoke suppression of ABS nanocomposites from multifunctional graphene [J]. Composites Part B: Engineering, 2019(177):107377.

[8] Zhan L, Zhao X, Ahmad Z, et al. Leaching behavior of Sb and Br from E-waste flame retardant plastics [J]. Chemosphere, 2020(245),125684.

[9] Xia Y, Liu S, Wang X, et al. The Analysis of Synergistic Effects of Zeolites applied in Intumescent Halogen-free Flame-retardant ABS Composites [J]. Polym-Plast. Technol, 2008(11):613-618.

[10] Martins P A , Valera T S , Tenório J A S , Estudo de sistemas retardantes de Chama sem Bromo para ABS [J]. Polímeros, 2014,24:572-578.

[11] Lu C, Chen T, Cai X, Halogen-free Intumescent Flame Retardant for ABS/PA6/SMA Alloys. Journal of macromolecular science [J]. Physics, 2009(48):651-662.

[12] Yi L, JiangsongY, Xufu C, Application of a novel halogen-free intumescent flame retardant for acrylonitrile-butadiene-styrene [J]. J. Appl. Polym. Sci, 2012(124):1475-1482.

Viser Technology Pte. Ltd.
Research and Application of Materials Science
DOI: 10.33142/rams.v6i2.14587

Research Article Open Access

Ordered Mesoporous Fe-Nx/C Materials as Highly Efficient Self-supporting Electrocatalysts for Oxygen Reduction

LianYan LIAO, YuXi ZHANG, Heng Qiang ZHANG, TongYin JIN*

College of Chemistry and Chemical engineering , Hebei Minzu Normal University, Chengde, Hebei, 067000, China

*Corresponding Author: Tongyin JIN, E-mail: tyjin0521@hbun.edu.cn

Abstract

A new mesostructured non-precious-metal catalyst (NPMC) was easily created using a straightforward nanocasting technique with 1,10-phenanthroline iron chelates as the sole precursor. The resulting Fe-Nx/C material, characterized by its Hexagonal mesostructures with an ordered arrangement, Extensive surface extent, expansive pore structure, and evenly Scattered Fe-Nx groups within Graphite-like carbon structures, Established to be an remarkable self-supporting cathode catalyst for the oxygen reduction reaction (ORR). It demonstrated superior specific oxygen reduction activity in 0.1M KOH alkaline solution compared to commercial Pt/C catalysts (20wt%Pt, JM), showing a more positive onset potential (0.0V vs Ag/AgCl), approximately 1.7 times the kinetic-limiting current density of Pt-C-JM, and higher current density across the entire potential range. Additionally, it exhibited an onset potential of 0.93V (vs RHE) for ORR and about 1.3 times the current density at 0.6V (4.9mA cm^{-2}) compared to the best NPMC materials reported in the literature, with a catalyst loading of 0.6mg cm^{-2} in 0.5M H_2SO_4 media (approximately 3.8mA cm^{-2}).

Keywords: Mesoporous; Oxygen reduction reaction; non-precious metal; self-supporting catalysts

1 Introduction

Proton exchange membrane fuel cells (PEMFCs) have Inspired significant attention in the past few decades as An eco-friendly technology. A major challenge for achieving efficient electrochemical energy conversion in PEMFCs is the slow oxygen reduction reaction (ORR) that is conducted at the cathodes. To enhance the ORR rate, catalysts made from platinum or platinum-based binary (Pt-Pd) or ternary (Pt-Ru-Co) materials are typically used, as they offer the best performance for electrode reactions and long-term stability. However, the high cost and limited availability of these precious metals Inhibit the widespread commercialization of PEMFCs[1-3]. Consequently, global research efforts have focused on finding cost-effective and High-efficiency, economical non-precious metal catalysts[3-6]. While nitrogen-doped carbon nanomaterials, such as nanotubes[7-8], graphene [9-10], and mesoporous carbons[11-12], have proven to be effective catalysts due to their high electrocatalytic activity and stability for the oxygen reduction reaction (ORR) in alkaline electrolytes, their performance in acidic electrolytes is significantly lower[13-15]. Among the various non-precious metal catalysts (NPMCs) being explored as candidates to platinum-based catalysts for ORR, nitrogen-coordinated transition metals within a carbon matrix (M-Nx/C), particularly Fe-Nx/C materials[2,5], show the most promise as noble-metal-free cathode catalysts. There has been considerable focus on enhancing their active site density to improve catalytic activity through various strategies [5-6,16]. Typically, Fe-N4 chelate complexes [19] or simple precursors made from iron salts and nitrogen sources supported on carbon are used to create Fe-Nx/C catalytic materials[23-28]. However, the precursors used in the production of these traditional Fe-Nx/C catalysts often struggle to penetrate the inner pores of carbon supports, leading to active sites being primarily located on the Exterior of the carbon supports, which results in inadequate Catalytic capability for ORR[19].

An alternative approach called "ordered mesoscopic structure control" has been suggested to improve the catalytic activity of Fe-Nx/C materials for the oxygen reduction reaction (ORR) [29-31]. This method focuses on effectively concentrating active sites at the inner edges of mesoporous structures with well-organized pore channels and a high surface area by choosing suitable precursors and preparation techniques. The heating of Fe-N4 macrocycle molecules in conjunction with some kinds of carbon sources Including formaldehyde[33], sucrose[35], and the thermolysis of Ferrous acetates[34] incorporated into mesoporous CNx under inert or ammonia-containing gases, leads to the creation of effective mesoporous Fe-N-C catalytic materials[33,35]. However, the inclusion of additional carbon precursors in these processes

Received on October 7th, 2024; Accepted on November 17, 2024

reduces the fraction of reactive nitrogen species in the final products, thus complicates the even Dispersion of active nitrogen-transition metal species within the mesoporous structures[33,35]. Furthermore, Heat treatment may lead to the emergence of non-active species like Fe or FeCx and generate the unequal dispersion of carbon, nitrogen, and iron precursors, potentially obstructing catalytic active site [5]. Additionally, The mentioned mesoporous Fe-Nx/C frameworks exhibit low graphitic structures, which can optimizes surface area and active site potential but also reduce the electron conductivity of these catalysts, presenting challenges for membrane electrode assembly. The use of costly macrocycle precursors, toxic ammonia gas, and complex synthesis methods also complicates mass production and increases costs. Thus, creating highly efficient Fe-Nx/C catalytic materials for ORR using inexpensive precursors while balancing ordered mesostructures, high surface area, high active site density, and high graphitic structures remains a significant challenge.

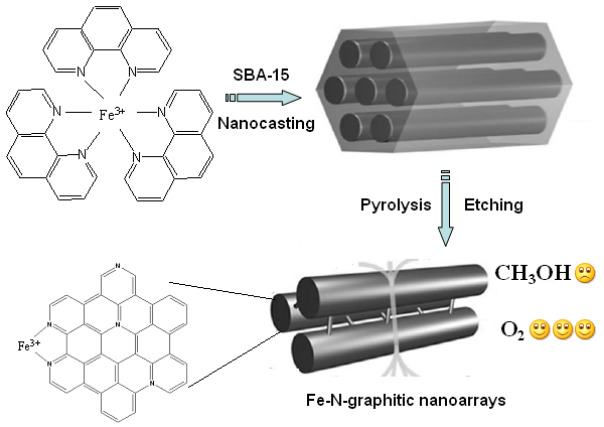

Figure 1 Synthesis of ordered mesopropus Fe-Nx/C materials as self-supporting NPMCs for ORR

In this research, we successfully synthesized ordered mesoporous Fe-Nx/C materials with desired characteristics using a standard nanocasting technique, employing Fe^{3+} phenanthroline chelates as the sole precursor (see Figure 1). Various techniques, including XRD, TEM, SEM, EDS-Mapping, BET, SAED, and XPS, confirm that the resulting materials exhibit ordered mesoporous structures, graphitic frameworks, a substantial specific surface area, and numerous active sites. The materials demonstrated highly efficient ORR catalytic activity, excellent methanol durability in electrocatalytic applications, and improved stability in both alkaline and acidic environments, demonstrated by cyclic voltammetry, current-time chronoamperometric response, and rotating-disk voltammetry measurements. Additionally, we propose potential explanations for the high activity of Fe-Nx/C materials based on the findings from electrocatalysis studies and the analysis of their active species in comparison to Fe(Co)-Nx/C, and Nx/C materials.

2 Experimental

2.1 Synthesis

In the kinetic energy theorem, students are trained to understand the relationship between kinetic energy and kinetic energy, so that students can grasp the concept of kinetic energy and gradually generate a certain concept of energy from kinetic energy. By deepening the understanding of the relationship between motion and energy, we can gradually grasp the kinetic energy theorem and learn to apply it to deal with relevant problems [2].

The goal of scientific thinking: to cultivate students' scientific thinking ability to carry out scientific experiments from the perspective of physics; Combining the analysis of experimental results with comprehensive logical reasoning to obtain conclusions; Cultivating students' ability to design experiments with scientific thinking; Through the analysis of the experimental results, the students' ability of scientific and logical reasoning, doubt and innovation is cultivated.

The objective of the experimental research is to cultivate students' ability to put forward physical problems and make scientific conjectures; Cultivating students' communication and cooperation ability through group experiments; The research is carried out by the method of controlling variables, so as to cultivate students' research thinking.

Scientific working attitude and responsibility goal: to correctly guide students to understand the relationship between kinetic energy and kinetic energy theorem and physical conditions in life, especially to let students realize that the application of kinetic energy is closely related to life, and to cultivate students' mentality of attaching importance to and loving physics. Adopt a positive attitude, train students to find problems, actively explore the concept, and cultivate students' spirit of cooperation in the search. Using kinetic energy theorem and its universal application in real life, cultivate students' sense of scientific responsibility. As the key quality of physics is an interrelated whole, it is necessary to cultivate not only students' research quality but also students' energy concept when guiding students to carry out working group research experiments; Scientific way of thinking; Scientific mentality and quality of responsibility. It can not only improve the teaching efficiency, but also enrich the teaching content.

The overall goal of classroom teaching in this competition class: Firstly, cultivate students' research quality through group experiments. Secondly, understand the concept of kinetic energy; Master the physical quantities that affect kinetic energy. Understand the application of kinetic energy expression; Let students feel the thinking process of dealing with new problems

with old knowledge through objective thinking, and learn this scientific way of thinking. Thirdly, understand the relationship between kinetic energy theorem and daily life and specific applications, so that students can feel the close relationship between physics and life and deal with problems in daily life with objective thinking.

Ordered mesoporous Fe-Nx/C materials were synthesized using three standard nanocasting methods [32], which include precursor filling, pyrolysis, and template etching. The regular preparation protocol is presented herein: 0.5g of dried SBA-15 samples, synthesized following prior publications, were combined with a 19mL alcohol solution containing 0.8g of 1,10-phenanthroline, 0.58g of $FeCl_6$ $3H_2O$ salts, and 1mL of water. The obtained mixture was stirred well, then the solvent was allowed to evaporate at ambient temperature. The derived powders were subsequently burned at about 900˚C for 120 minutes in a protective gas atmosphere, while the thermal ramp rate of 2˚C per minute initially. Finally, the products were acquired through etching the silica templates in a 20wt% HF solution for 12 hours, resulting in the formation of Fe-Nx/C.

For comparison, mesoporous cobalt-nitrogen-carbon materials (Co-Nx/C) and mesoporous nitrogen-doped carbon further synthesized by a similar preparatory technique, utilizing 0.8g of 10-phenanthroline and either 0.54g or 0g of $Co(Ac)_2$ $2H_2O$ as precursors.

2.2. Characterization

Powder X-ray diffraction patterns (XRD) were obtained using a Rigaku D/Max-2500 diffractometer operating at 40 kV and 40 mA with CuKα radiation. Transmission electron microscopy (TEM) images were captured with a JEM-2010 microscope at an acceleration voltage of 200 kV. Nitrogen adsorption and desorption measurements were conducted at 77 K using a Micromeritics Tristar 3000 analyzer. X-ray photoelectron spectroscopy (XPS) measurements were carried out on a Thermo ESCALAB 250 instrument using Al Kα radiation (1486.6 eV), with C 1s (284.6 eV) serving as a reference for binding energy correction.

2.3. Electrochemical measurment

Electrocatalytic capability of the synthesized catalysts for the oxygen reduction reaction (ORR) was assessed using cyclic voltammetry (CV) and rotating disk electrode (RDE) methods. A standard three-electrode setup was utilized, consisting of a glass carbon RDE as the working electrode, an Ag/AgCl, KCl (3 M) electrode as the reference, and a platinum wire as the counter electrode. The experiments in alkaline conditions were conducted in an O_2-saturated 0.1 M KOH solution, with the potential being cyclically scanned from -1.2 to +0.2 V at a scan rate of 10 mV/s at room temperature, following a 15-minute purging with O_2 or N_2 gas. The electrocatalytic activities for ORR in acidic conditions were explored in an O_2-saturated 0.5 M H_2SO_4 solution, with the potential scanned between 1.0 and -0.2 V (vs Ag/AgCl). The working electrode was prepared by dissolving 15 mg of mesoporous materials in 4 ml of a solvent mixture of Nafion (5%) and isopropanol (in a 1:9 volume ratio) through sonication. For comparative evaluation, a conventional catalyst consisting of 20 wt.% Pt on black carbon (JM, fuel cell grade) was also used, with a Pt-C suspension prepared using the same method. The catalyst suspension was applied to the polished glassy carbon electrode surface, which was then allowed to dry at ambient temperature before measurements, resulting in a catalyst loading of 30 μg/cm² for all working electrodes.

3. Results and Discussion

3.1 Synthesis

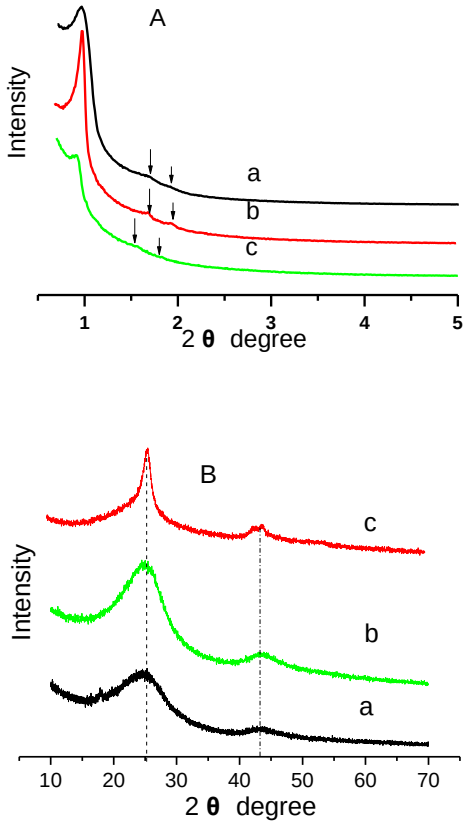

Figure 2 Low-angle (A) and high-angle (B) XRD patterns of N_x/C (a), Co-N_x/C(b) and Fe-N_x/C (c)

The structure, morphology, and textural properties of ordered mesoporous Fe-Nx/C, Co-Nx/C, and Nx/C materials have been analyzed by XRD, TEM, SEM, and N2-sorption techniques. The small-angle X-ray diffraction (XRD) patterns displayed three individual diffraction peaks corresponding to the (100), (110), and (200) reflections the hexagonal structures (Figure 2A), similar to those found in Arranged two-dimensional

mesoporous carbons of the CMK-3 type [36]. Transmission electron microscopy (TEM) images (Figure 3) demonstrated that mesostructures which assembled from rods bonded by smaller subsidiary branches, featuring quasi-cylindrical mesoscale pores with a mean size of approximately 4.0 nm. High-angle XRD patterns showed two peaks at 2θ=25 and 43˚, which correspond to (002) and (101) diffractions of graphitic carbon (Figure 2 B). The d (002) spacing of about 0.36 nm is slightly larger than that of graphite (0.34 nm). Selected-area electron diffraction (SAED) patterns (inset in Figure 3) exhibited clear diffraction rings, indicating the presence of a graphitic phase in the pore walls. High-resolution TEM images (Figure 3 b,d and f) clearly demonstrate the graphitic structure within the mesoporous frameworks of Fe-Nx/C, Co-Nx/C, and Nx/C materials. Unlike the disorganized or semi-crystalline carbon frameworks in prior research on mesoporous Fe-N-C materials [33-35], the well-crystalline graphitic frameworks of Fe-Nx/C, Co-Nx/C, and Nx/C materials are expected to enhance electron conductivity. It should be highlighted that the presence of metal species promotes the crystallization of metal-Nx/C materials, resulting in higher crystallinity compared to Nx/C produced from metal-free pyrolysis of phenanthroline under the same conditions, particularly for Co-Nx/C materials, which exhibit increased (002) diffraction intensity and narrower half-peak widths in C1s XPS peaks [10].

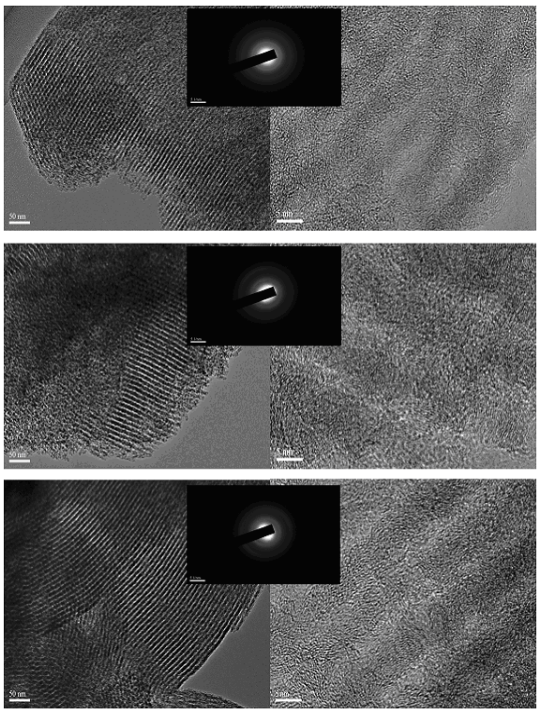

Figure 3 TEM images of Co-Nx/C (a,b), CNx(c,d), and Fe-Nx/C (e,f). Inset is the corresponding SAED image

The developed materials' gas adsorption isotherms (Figure 4A) were analyzed to examine their textural characteristics, all of which display typical IV type curves indicative of mesoporous materials. According to the BJH model derived from desorption tests, the mesopore radius distribution for all samples is centered around 3.8 nm. In comparison to the synthesized Nx/C materials, the Fe-Nx/C (0.70 cm^3/g) and Co-Nx/C (0.56 cm^3/g) showed reduced pore volumes. However, Fe-Nx/C has a BET surface extent (532 m^2/g) that is comparable to that of Nx/C materials, which is greater than that of prior studies on mesoporous Fe-N-C materials produced under inert gas environments [32]. The BET surface extent of Co-Nx/C is inferior to that of both Fe-Nx/C and Nx/C due to its highly graphitic pore walls. These structural and textural property data are sorted in Table 1. The morphologies of the synthesized three materials were also verified through their respective SEM images, which resemble the typical rod-like morphology of SBA-15 materials.

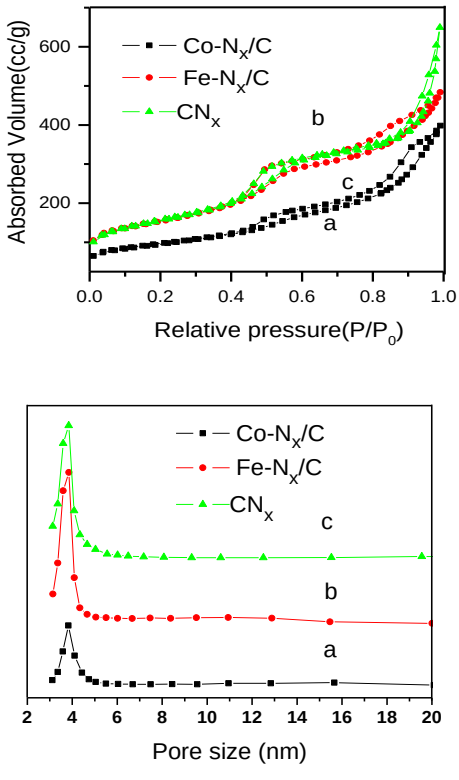

Figure 4 The N_2 sorption isotherms (A) and the corresponding pore size distribution curves (B)

Table 1 The physical and electrochemical parameters of mesoporous materials

Samples	Unit cell parameter (nm)	Surface extent (cm^2/g)	Pore size (nm)	Pore volume (cm^3/g)	Morphology
Co-N_x/C	8.4	330	3.8	0.56	rod
Fe-N_x/C	8.1	532	3.8	0.70	rod
N_x/C	8.1	538	3.8	0.91	rod

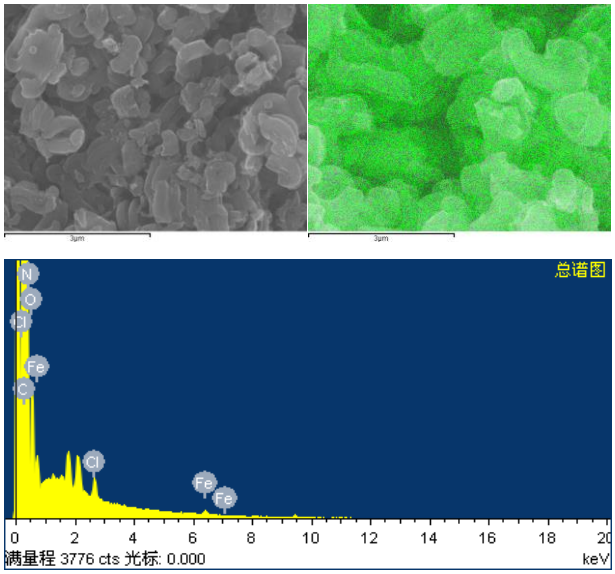

Figure 5 SEM images (A) , SEM-Mapping image(B) and EDS spectrum (C) of ordered mesoporous Fe-N_x/C material

The distribution control for metal and nitrogen active species is very important in the construction of Fe-N_x/C catalytic materials with high activity. The budget-friendly nitrogen precursors such as ethylenediamine, polyaniline, cyanamide, and NH_3do not spontaneously generate uniformly spread Fe-N_x sites prior to pyrolysis. As a result, large Fe or FeCx particles are often inevitably produced during the thermal treatment procedure, which could hinder the building of active sites in the preparation and block the active sites in catalysis. Profiting from the well-Dispersed Fe-N sites prior to pyrolysis in 1,10-phenanthroline iron chelates and the confinement effect of the SBA-15 mesochannels, the presenting Fe-N_x/C materials reveal the well-distributed Fe and N species on carbon frameworks in large domains, illustrated by the EDS-mapping technique. Different from mesoporous Fe-N-C materials prepared by heating formaldehyde resins mixed Fe-N_4 macrocycle molecules [33] and mesoporous CN_x-absorbed iron acetates in NH_3 [34], no any bulk Fe species were observed in this mesostructured Fe-N_x/C material, Consistent with the data of XRD and TEM. In comparison to the previous mesoporous Fe-N-C materials[32-34], the unique Fe-N_x/C materials were expected to facilitate the improving of active site density and the assembling in cathode catalyst layers and promote the rapid diffusion of O_2 molecules.

3.2 Electrocatalytic activity

The electrocatalytic characteristics of mesoporous Fe-Nx/C, Co-Nx/C, and Nx/C substances in a 0.1M KOH alkaline solution were examined using cyclic voltammetry (CV) and rotating disk electrode (RDE) methods. All potentials were referenced against Ag/AgCl, KCl (3 M) in 0.1M KOH for easier comparison. Significant decreases in current were observed as distinct cathodic peaks for all three substances, illustrating considerable electrocatalytic dynamics in oxygen reduction (see Figure 6 A and S3). As illustrated in Figure 6 B and D, the metal–N–C materials showed a significant enhancement in activity compared to mesoporous Nx-C, as evidenced by the notable positive shifts in the ORR cathodic peak potentials for Fe-Nx/C, Co-Nx/C, and Nx-C (-0.11, 0.18, and 0.22V in the CVs, respectively) and their corresponding onset potentials (0.02, -0.08, and -0.1 V in the polar curves at 1600rpm, respectively). Linear regressions based on the Koutecky–Levich equations confirmed that the combination of metal appreciably improved the electron-transfer kinetics (JK) and the measured current densities (J) (Figure 6F), particularly for Fe-Nx/C materials, which reached 16.0 mA cm^{-2} at -0.4V. In contrast to the benchmark Pt-C materials with an onset potential of -0.03V, the onset potential for mesoporous Fe-Nx/C showed a positive shift of 5mV. The JK value for Fe-Nx/C was significantly higher than that of commercial Pt–C (9.6mA cm^{-2}), and the current density (J) of Fe-Nx/C also surpassed that of Pt-C materials in both kinetic and diffusion potential ranges, indicating distinguished electrocatalytic activity for ORR. When contrasted with the highly effective mesoporous CNx developed by Klaus Müllen et al [11], mesoporous Fe-Nx/C exhibited more favorable onset and peak potentials, as well as larger JK and J values under similar measurement conditions, highlighting its enhanced catalytic activity for ORR in 0.1M KOH alkaline media.

The rotating-disk voltammetry profiles for Fe-Nx/C, Co-Nx/C, and Nx/C in O_2-saturated 0.1M KOH indicated that their current densities increased with higher rotation rates (ranging from 400 to 2500 rpm, as shown in Figure 6 C and S4). The Koutecky–Levich (K-L) plots for Fe-Nx/C materials between -0.4 and -0.8 V displayed strong linearity (Figure 6C), implying that the electron transfer numbers for oxygen reduction at various electrode potentials are consistent. The linearity and parallel nature of the plots typically suggest first-order reaction kinetics concerning the concentration of dissolved O_2. Based on the slope of the plots at -0.4V and the Koutecky–Levich equations ($B=0.62nFC_0(D_0)^{2/3}\nu^{1/6}$, $C_0=1.2\times10^{-3}$ mol L^{-1}, $D_0=1.9\times10^{-5}$ cm s^{-1}, $\nu=0.01$ cm^2 s^{-1}), the electron transfer number was turned out to be 4.1, indicating a four-electron transfer process for the mesoporous Fe-Nx/C material during oxygen reduction. In contrast, The incline of the K-L plots for Co-Nx/C and Nx/C between -0.4 and -0.8V differed from one another. The calculated electron transfer numbers at -0.4V were 3.1 for Co-Nx/C and 2.2 for Nx/C, respectively. The electrochemical reduction of O_2 on mesoporous Co-Nx/C involves a interrelation of four-electron and two-electron transfers, while Nx/C primarily follows a two-electron transfer process in the oxygen reduction reaction (ORR). The presence of metal species alters the oxygen reduction pathway for the resulting mesoporous materials, with Fe species promoting a four-electron transfer route.

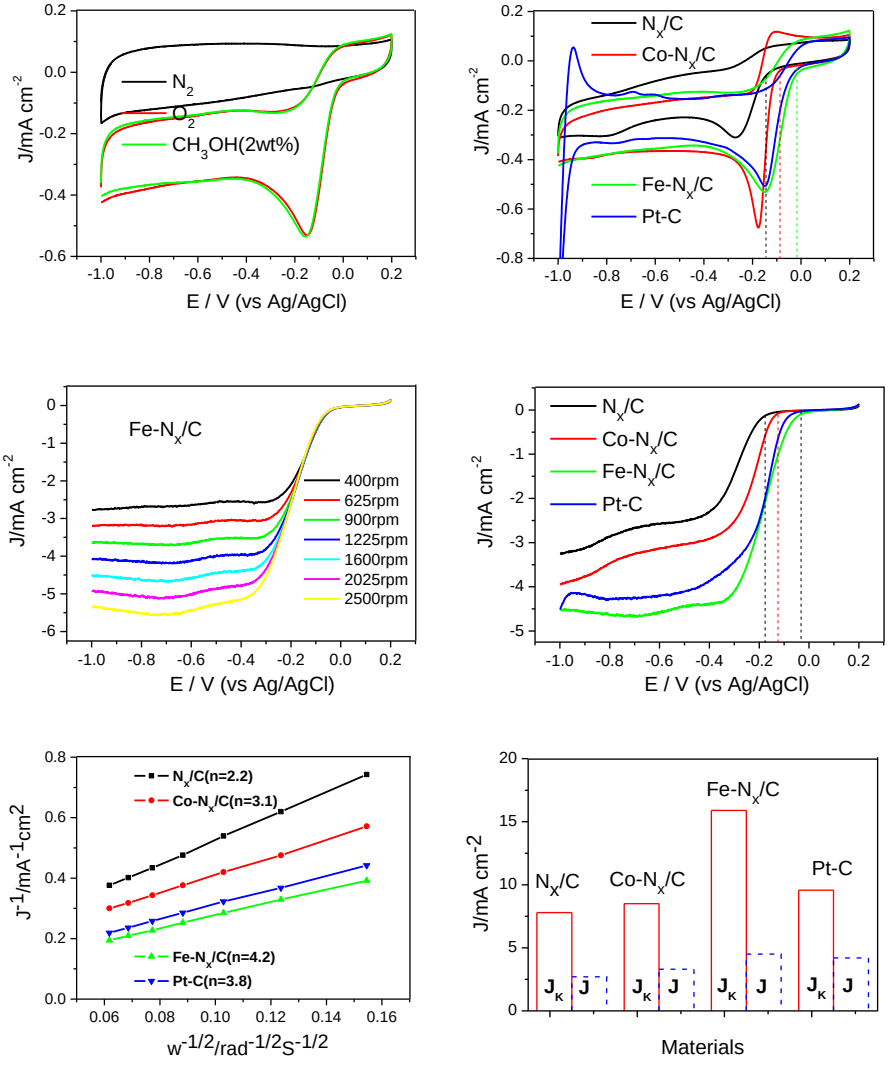

Figure 6 A) Cyclic voltammograms of mesoporous Fe-N_x/C in a 0.1M KOH solution at a scan rate of 10 mV s^{-1}. B) Cyclic voltammograms of diverse mesoporous substances and Pt-C in an O_2-saturated 0.1m solution of KOH at a scan rate of 10 mV s^{-1}. C) Rotating-disk voltammograms documented for mesoporus Fe-N_x/C substances at a range of rotation rates. D) RDE voltammograms of the series of mesoporus substances and Pt-C at a rotation rate of 1600 rpm. E). Koutecky–Levich plot of J_L^{-1} versus ω^{-1} at -0.4V (vs Ag/AgCl) of mesoporus substances and Pt-C at -0.4V(vs Ag/AgCl). F) Electrochemical activity given as the kinetic (J_K)- and diffusion(J_L) limiting current density at -0.4 V (vs Ag/AgCl) for the mesoporus substances and Pt-C.

The electrocatalytic characteristics of Fe-Nx/C, Co-Nx/C, and Nx/C for the oxygen reduction reaction (ORR) in 0.5M H_2SO_4 was examined. All potentials were calibrated against the reversible hydrogen electrode (RHE) in 0.5M H_2SO_4 solutions. The cyclic voltammograms (CVs) of mesoporous Fe-Nx/C and Co-Nx/C in O_2-saturated 0.5M H_2SO_4 showed significant oxygen reduction current peaks at approximately 0.70 and 0.67 V (vs RHE), respectively. In contrast, Nx/C exhibited only a minimal reduction current, suggesting its restricted catalytic efficiency towards the oxygen reduction reaction under acidic environments, consistent with earlier studies. The observed positive shift in the ORR onset potential, extracted from the polar diagrams at 900 rpm, was noted for Fe-Nx/C (0.87 V), Co-Nx/C (0.83 V), and Nx/C (0.70 V), mirroring results found in 0.1M KOH alkaline media. This suggests that mesoporous Fe-Nx/C demonstrates superior catalytic activity in acidic environments.

The onset potential of as-prepared Fe-N_x/C is slightly more negative than that of Pt-C-JM (0.91V) at the catalyst loading of 30ug cm^{-2}. However, it is should be noticed that the escalating catalyst loading of Fe-N_x/C from 30 to 600ug cm^{-2} resulted into the more positive onset-potential and strikingly increasing current density (Figure 7E and table S4), attributing to the superior mass transport ability and expeditious O_2 diffusion in mesoporous materials. The corresponding onset-potential and half-wave potential for the electrode with 600ug cm^{-2} Fe-N_x/C materials are 0.93 and 0.78V in RDE

testing. The difference of half-wave potential between Fe-N_x/C electrode with 600ug cm^{-2} and Pt/C electrode (TKK, 29wt%) with 29 ug Pt cm^{-2} (100ug cm^{-2} Pt-C) determined by polarization curve at 900rpm was only about 3 mV. In contrast, the difference of half-wave potential between PANI-Fe-C materials reported by Edward F. with 600ug cm^{-2} in 0.5M H_2SO_4 and Pt/C(E-TEK, 20wt%) with a loading of 20 ug Pt cm^{-2} in 0.1M $HClO_4$ is 43mV. Moreover, the current density value (2.1mA cm^{-2}) of Fe-N_x/C electrode at 0.8 V determined by polar curves at 900rpm is higher than that of the PANI-Fe-C electrode[29] at the similar testing conditions with 600ug cm^{-2} catalyst loading (about 2.1mA cm^{-2} at 0.8V). This current density value (4.9mA cm^{-2}) of Fe-N_x/C at diffusion region of 0.6V is much higher than the values of Pt-C-JM (3.4mA cm^{-2}), Pt-C-TKK(4.2mA cm^{-2}) and PANI-Fe-C electrode(3.8mA cm^{-2}). Mesoporous Fe-N_x/C materials in testing show the state-of-the-art catalytic activity among the reported NMPCs. In addition, a four electron route in oxygen reduction for Fe-N_x/C is confirmed by the slope of the plots at 0.3V based on of the Koutecky–Levich equations ($B=0.62nFC_0(D_0)^{2/3}\nu^{1/6}$, $C_0=1.13\times10^{-3}$ mol L^{-1}, $D_o=1.83\times10^{-5}$ cm s^{-1}, ν= 0.01 cm^2 s^{-1}) (Figure 7C). The calculated electron number of Co-N_x/C in ORR is 2.5, suggesting a mainly two-process reaction process for ORR. The resultant mesoporous materials with different metal precursors possess the different ORR route in acidic media, similar to the conclusion obtained in alkaline media.

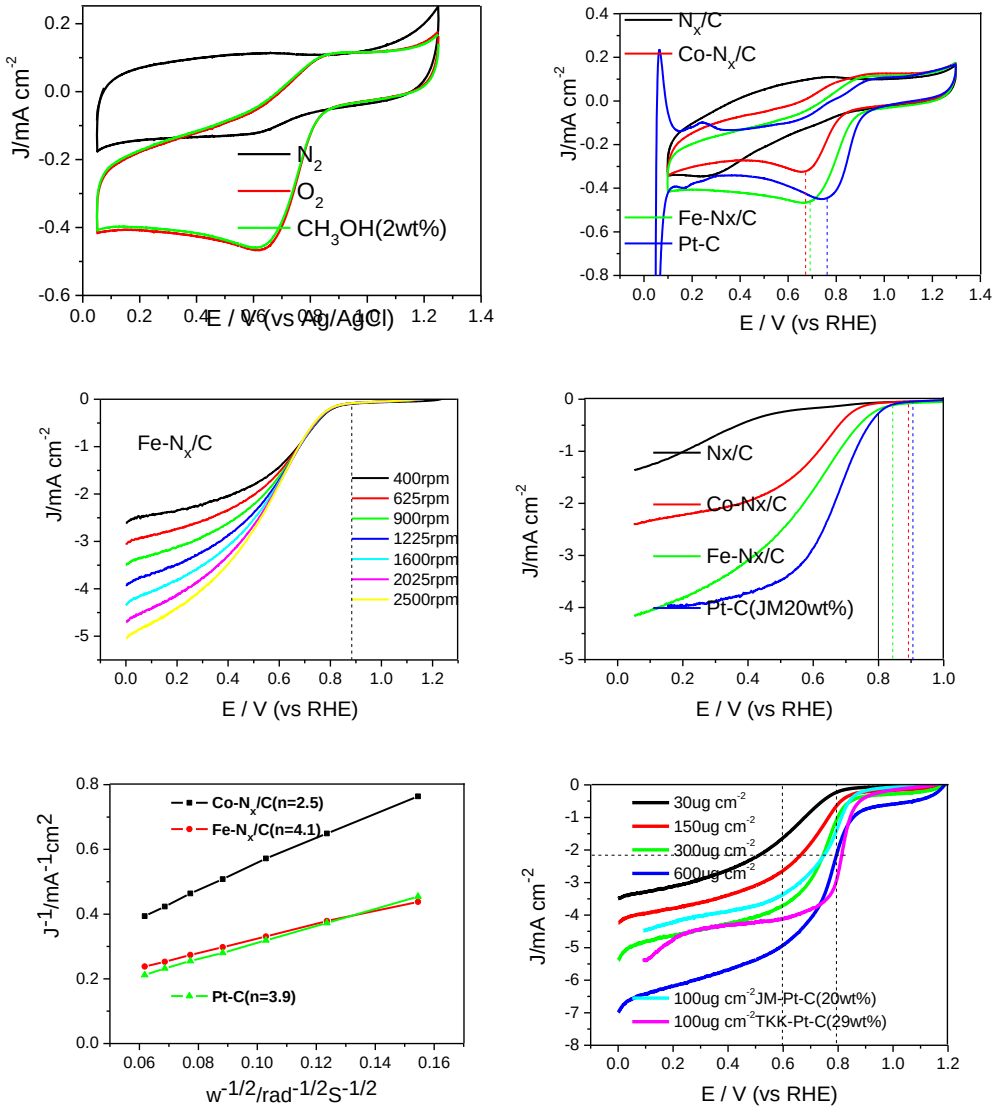

Figure 7 A) Cyclic voltammograms of mesoporous Fe-Nx/C in an O_2-saturated 0.5M solution of H_2SO_4 at a scan rate of 10 mV s^{-1}. B) Cyclic voltammograms of different mesoporous substances and Pt-C in an O_2-saturated 0.5M solution of H_2SO_4 at a scan rate of 10 mV s-1. C) RDE voltammograms of the series of mesoporus substances and Pt-C at a rotation rate of 900 rpm. D) Electrochemical activity given as the kinetic (JK)- and diffusion(JL) limiting current density at 0.0 V (vs RHE) for the mesoporus substances and Pt-C.

3.3 The composition and surface species analysis

As discussed earlier, there was a noticeable increase in catalytic capability for the oxygen reduction reaction (ORR) when comparing Nx/C to Co-Nx/C and Fe-Nx/C in both alkaline and acidic environments. Given their similar mesostructure, morphology, and the higher surface area of Nx/C, the significant discrepancies in ORR activity among these materials can be ascribed to the quantity and type of nitrogen-containing active species present on their surfaces. The nitrogen concentration on the surface layers of these specimens, as measured by X-ray photoelectron spectroscopy (XPS), decreases from Fe-Nx/C (2.6 mol%) to Co-Nx/C (2.1 mol%) and finally to Nx/C (1.7 mol%), which aligns with their decreasing activity. Regarding the types of nitrogen active species, there is a general consensus that nitrogen plays a crucial role.

Table 2 Toutlines the makeup and surface characteristics of mesoporous materials

Samples	C (mol%)	N (mol%)	O (mol%)	Metal[c] (mol%)	N_{N-O} (%)	N_{Pyr} (%)	N_q (%)	N_{N-H} (%)
N_x/C	80.2	1.7	18.1	-	49.8	8.4	18.2	23.6
Co-N_x/C	84.9	2.1	12.6	0.24	15.4	34.0	34.4	16.2
Fe-N_x/C	87.4	2.6	9.8	0.16	12.7	52.7	14.6	19.9

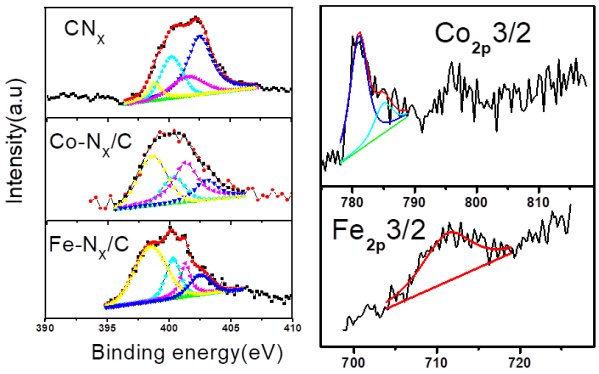

Figure 8 The N1s spectra (B) of Fe-N_x/C, Co-N_x/C and CN_x. (C) is the corresponding $Co_{2p}^{3/2}$ and $Fe_{2p}^{3/2}$ XPS spectra

Incorporating nitrogen into the graphite matrix, particularly for creating pyridine-like nitrogen atoms at the edges of the graphite plane, is essential for developing a highly effective carbon-based catalytic material that is either non-precious metal or metal-free. The nitrogen concentration in Fe-Nx/C, Co-Nx/C, and Nx/C substances was analyzed using N 1s XPS spectra (Figure 8B), which can be broken down into four categories based on binding energy: pyridine-like (398.4 eV), graphite-like (401.3 eV), pyrrollic-like (～400 eV), and pyridine N-oxides (402-404.0 eV). A notable observation is that the metal species in the precursors significantly enhance the amount of pyridine-like nitrogen in M-Nx/C substances, as evidenced by the deconvoluted N1s spectra showing Nx/C (8.4%), Co-Nx/C (34.0%), and Fe-Nx/C (52.7%). Literature suggests that metal species act as catalysts for the formation of pyridine-like nitrogen [38-39]. This study proposes a new role for metal species as protective agents to account for this observation. The proportion of pyridine-N-oxides in the nitrogen species of Co-Nx/C (15.4%) and Fe-Nx/C (12.7%) is significantly lower than that in Nx/C (49.8%), as determined by XPS. The presence of metal ions appears to inhibit the oxidation of pyridine-like nitrogen during pyrolysis, reducing the formation of inactive pyridine-N-oxides in the final products, likely lead to the coordination effect between transition metals and nitrogen.

The role of N-binding metal species and N atoms in CNx as catalytic sites for M-Nx/C catalysts remains a topic of discussion in the literature [1-6]. Our research indicates that mesoporous Nx/C materials exhibit strong catalytic activity in 0.1M KOH alkaline solutions, suggesting that N atoms in carbon, particularly pyridine-N atoms, work as active sites for the oxygen reduction reaction (ORR) in this medium. The enhanced ORR activity observed in Fe-Nx/C and Co-Nx/C can likely be attributed to an increase in pyridine-like nitrogen species on their surfaces. However, the significant difference in ORR activity between mesoporous Fe-Nx/C and Nx/C substances in 0.5M H_2SO_4 acidic solutions is puzzling if N atoms in carbon are the primary active sites, as the mesoporous Nx/C materials still contain approximately 8.4% pyridine-N species on their surface. XPS analysis reveals that Approximately 0.24 mol % Fe and 0.16 mol % Co are present on the external strata of the M-Nx/C materials. The affinity energies of the Fe^{2p} (711.3 eV) and Co^{2p} (781.8 eV) peaks, as determined by XPS, indicate that the predominant metal categories in Fe-Nx/C and Co-Nx/C materials are N-coordinated metals, consistent with earlier research [38,39]. Additionally, pyridine- and pyrrolic-like nitrogen species located at the edges of graphitic structures can also act as metal coordination sites due to their electron-donating characteristics. Therefore, it is believed that both N-binding metal species and N atoms in CNx can serve as active sites for ORR, with M-Nx moieties within the carbon matrix enhancing the catalytic capability of M-Nx/C materials, especially in acidic environments. Overall, the increased surface nitrogen content, particularly with a high proportion of pyridine-like nitrogen and abundant Fe-Nx moieties in the carbon structure, contributes to the exceptional catalytic performance of Fe-Nx/C materials for ORR.

3.4 Methanol-tolerate property and durability

The methanol tolerance of cathode catalysts is a significant issue in direct-methanol fuel cells. To investigate potential crossover effects, we assessed the electrocatalytic selectivity of mesoporous Fe-Nx/C and Pt-C-JM in O_2-saturated 0.1M KOH with 2wt% methanol. In the CV curve for Pt-C-JM, we observed two peaks at -0.35 and -0.20 V (vs Ag/AgCl) corresponding to methanol oxidation,

while the cathodic current maximum for the oxygen reduction reaction (ORR) disappeared. In contrast, mesoporous Fe-Nx/C showed no significant change in the oxygen-reduction current under the same conditions (Figure 6 A). Similar results were noted for both mesoporous Fe-Nx/C and Pt-C-JM in 0.5M H_2SO_4, where the addition of 2wt% CH_3OH in O_2-saturated 0.5M H_2SO_4 had minimal impact on the oxygen reduction current peak and onset potential of Fe-Nx/C in CV measurements (Figure 7A). Additionally, we tested the durability of Fe-Nx/C materials at a constant voltage for 20,000 seconds in O_2-saturated 0.1M KOH or 0.5M H_2SO_4 solutions at a turning velocity of 1600 rpm (Figure 9). The current-time (i-t) chronoamperometric response of Fe-Nx/C showed a relatively moderate reduction, maintaining a significant relative current of 74% in 0.1M KOH and 76% in 0.5M H_2SO_4 after 20,000 seconds. In comparison, the Pt-C-JM electrode with the same catalyst loading (30 μg cm^{-2}) exhibited a current drop to about 58.0% in 0.1M KOH and 50% in 0.5M H_2SO_4 after 20,000 seconds. Overall, the durability and selectivity of Fe-Nx/C materials for ORR outperform those of the Pt-C-JM catalyst in both alkaline and acidic environments.

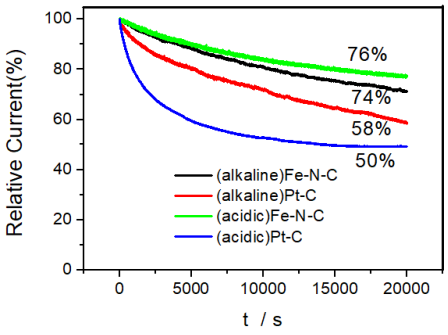

Figure 9 Current–time (i–t) chronoamperometric response of mesoporus Fe-Nx/C and Pt–C (JM, 20wt%) at -0.4 V(vs Ag/AgCl) in O_2-saturated 0.1mKOH at a rotation rate of 1600 rpm (A) and at 0.25 V(vs RHE) in O_2-saturated 0.5M H_2SO_4 at a rotation rate of 1600 rpm with the catalyst loading of 30ug cm^{-2}

4 Conclusions

In conclusion, we have successfully constructed an ordered mesoporous Fe-N_x/C materials with outstanding ORR performance by a novel metal chelate pyrolysis nanocasting approach using low-cost Fe phenanthroline chelates as the precursors. As compared to customary Pt-C catalysts and the reported NPMCs, this novel self-supporting catalyst exhibits the conspicuous ORR catalytic activity in term of the ORR current density and onset potential in both alkaline media and acidic media. The ordered mesostructure with high surface area, nitrogen-enriched graphitic backbones, and the abundant pyridine-like nitrogen and Fe-N_x moieties within carbons contributed to the excellent catalytic activity of Fe-N_x/C for ORR. The mesoporous Fe-N_x/C materials prepared by this novel synthesis method may be used as the practically promising substitute for the expensive noble metal catalysts in PEMFCs.

Fund Projects: The author gratefully acknowledges financial support from the Research project of Hebei Normal University for nationalities (No. STZD2023001) and Research on the Key Technologies for Collaborative Development of Clean Energy Development and Ecological Protection in Chengde (No. 202305B100); Research project of Hebei Minzu Normal University (No. DR2023001).

References

[1] A. Brouzgou, S.Q. Song, Panagiotis E. Tsiakaras. Low and non-platinum electrocatalysts for PEMFCs: Current status, challenges and prospects [J]. Applied Catalysis B: Environmental, 2012(127):371–388.

[2] Rapidah Othman, Andrew L. Dicks, Zhonghua Zhu. Non precious metal catalysts for the PEM fuel cell cathode [J]. international journal of hydrogen energy, 2012(37):357-372.

[3] Cicero W. B. Bezerra, Lei Zhang, Kunchan Lee, et,al. A review of Fe-N/C and Co-N/C catalysts for the oxygen reduction reaction [J]. Electrochimica Acta, 2008(53):4937–4951.

[4] Adina Morozan, Bruno Jousselme and Serge Palacin. Electrochemical performance of annealed cobalt – benzotriazole/CNTs catalysts towards the oxygen reduction reaction [J]. Energy & Environmental Science, 2011(4):1238–1254.

[5] Zhongwei Chen, Drew Higgins, Aiping Yu, et,al. A review on non-precious metal electrocatalysts for PEM fuel cells [J]. Energy & Environmental Science, 2011(4):3167–3192.

[6] Frédéric Jaouen, Eric Proietti, Michel Lefèvre, et al. Recent advances in non-precious metal catalysis for oxygen-reduction reaction in polymer electrolyte fuel cells [J]. Energy & Environmental Science, 2011,4(1):114-130.

[7] Kuanping Gong, Feng Du, Zhenhai Xia, et al. Nitrogen-doped carbon nanotube arrays with high electrocatalytic activity for oxygen reduction[J]. science, 2009,323(5915):760-764.

[8] Zhijian Wang, Rongrong Jia, Jianfeng Zheng, et al. Nitrogen-promoted self-assembly of N-doped carbon nanotubes and their intrinsic catalysis for oxygen reduction in fuel cells[J]. Acs Nano, 2011,5(3):1677-1684.

[9] Liangti Qu, Yong Liu, Jong-Beom Baek, et al. Nitrogen-doped graphene as efficient metal-free electrocatalyst for oxygen reduction in fuel cells [J]. ACS nano, 2010,4(3):1321-1326.

[10] Ziyin Lin, Min-kyu Song, Yong Ding, et al. Facile preparation of nitrogen-doped graphene as a metal-free catalyst for oxygen reduction reaction [J]. Physical Chemistry Chemical Physics, 2012,14(10):3381-3387.

[11] Ruili Liu, Dongqing Wu, Xinliang Feng, et al. Nitrogen-doped ordered mesoporous graphitic arrays with high electrocatalytic activity for oxygen reduction [J]. Angewandte Chemie International Edition, 2010,14(49):2565-2569.

[12] Wen Yang, Tim-Patrick Fellinger, and Markus Antonietti. Efficient metal-free oxygen reduction in alkaline medium on high-surface-area mesoporous nitrogen-doped carbons

made from ionic liquids and nucleobases [J]. Journal of the American Chemical Society, 2011,133(2):206-209.
[13] Xiqing Wang, Je Seung Lee, Qing Zhu, et al. Ammonia-treated ordered mesoporous carbons as catalytic materials for oxygen reduction reaction [J]. Chemistry of Materials, 2010,22(7):2178-2180.
[14] Ki Rak Lee, Kye Ung Lee, Jong Wook Lee, et al. Electrochemical oxygen reduction on nitrogen doped graphene sheets in acid media[J]. Electrochemistry Communications, 2010,12(8):1052-1055.
[15] Dingshan Yu, Qiang Zhang, Liming Dai, Highly efficient metal-free growth of nitrogen-doped single-walled carbon nanotubes on plasma-etched substrates for oxygen reduction [J]. Journal of the American Chemical Society, 2010,132(43):15127-15129.
[16] Michel Lefèvre, Eric Proietti, Frédéric Jaouen, et al. Iron-based catalysts with improved oxygen reduction activity in polymer electrolyte fuel cells [J]. science, 2009,324(5923):71-74.
[17] Hansan Liu, Zheng Shi, Jianlu Zhang, et al. Ultrasonic spray pyrolyzed iron-polypyrrole mesoporous spheres for fuel celloxygen reduction electrocatalysts [J]. Journal of Materials Chemistry, 2009,19(4):468-470.
[18] Thorsten Schillinga, Michael Bronb, Oxygen reduction at Fe–N-modified multi-walled carbon nanotubes in acidic electrolyte [J]. Electrochimica Acta, 2008,53(16):5379-5385.
[19] Robert L. Arechederra, Kateryna Artyushkova, Plamen Atanassov, et al. Growth of phthalocyanine doped and undoped nanotubes using mild synthesis conditions for development of novel oxygen reduction catalysts [J]. ACS applied materials & interfaces, 2010,2(11):3295-3302.
[20] Ulrike I. Koslowski, Irmgard Abs-Wurmbach, Sebastian Fiechter, et al. Nature of the catalytic centers of porphyrin-based electrocatalysts for the ORR: a correlation of kinetic current density with the site density of Fe− N4 centers [J]. The Journal of Physical Chemistry C, 2008,112(39):15356-15366.
[21] Médard C., Lefèvre M., Dodelet J. P., et al. Oxygen reduction by Fe-based catalysts in PEM fuel cell conditions: activity and selectivity of the catalysts obtained with two Fe precursors and various carbon supports [J]. Electrochimica Acta, 2006,51(16):3202-3213.
[22] Xin Wang, Wenzhen Li, Zhongwei Chen, et al. Durability investigation of carbon nanotube as catalyst support for proton exchange membrane fuel cell [J]. Journal of Power Sources, 2006,158(1):154-159.
[23] Cicero W. B. Bezerra,Lei Zhang,Kunchan Lee, et al. Novel carbon-supported Fe-N electrocatalysts synthesized through heat treatment of iron tripyridyl triazine complexes for the PEM fuel cell oxygen reduction reaction [J]. Electrochimica Acta, 2008,53(26):7703-7710.
[24] Hansan Liu, Zheng Shi, Jianlu Zhang, et al. Ultrasonic spray pyrolyzed iron-polypyrrole mesoporous spheres for fuel celloxygen reduction electrocatalysts [J]. Journal of Materials Chemistry, 2009,19(4):468-470.
[25] Ja-Yeon Choi, Drew Higgins, Zhongwei Chen. Highly durable graphene nanosheet supported iron catalyst for oxygen reduction reaction in PEM fuel cells [J]. Journal of the Electrochemical Society, 2011,159(1):B86−B90.
[26] Ja-Yeon Choi, Ryan Hsu, Zhongwei Chen. Nanoporous carbon-supported Fe/Co-N electrocatalyst for oxygen reduction reaction in PEM fuel cells [J]. ECS Transactions, 2010,28(23):101-112.
[27] Ja-Yeon Choi, Ryan S. Hsu, Zhongwei Chen. Highly active porous carbon-supported nonprecious metal− N electrocatalyst for oxygen reduction reaction in PEM fuel cells [J]. The Journal of Physical Chemistry C, 2010,114(17):8048-8053.
[28] Ryan S. Hsu, Zhongwei Chen. Improved Synthesis Method for a Cyanamide Derived Non-Precious ORR Catalyst for PEFCs [J]. ECS Transactions, 2010,28(23):39−46.
[29] Edward F. Holby, Gang Wu, Piotr Zelenay, et al. Structure of Fe-Nx-C defects in oxygen reduction reaction catalysts from first-principles modeling [J]. The Journal of Physical Chemistry C, 2014,118(26):14388-14393.
[30] Shayna Brocato, Alexey Serov, Plamen Atanassov, pH dependence of catalytic activity for ORR of the non-PGM catalyst derived from heat-treated Fe–phenanthroline [J]. Electrochimica acta, 2013(87):361-365.
[31] Xiufang Chen, Young-Si Jun, Kazuhiro Takanabe, et al. Ordered mesoporous SBA-15 type graphitic carbon nitride: a semiconductor host structure for photocatalytic hydrogen evolution with visible light [J]. Chemistry of Materials, 2009,21(18):4093-4095.
[32] Lei M., Li P. G., Li. L. H., et al. A highly ordered Fe-N-C nanoarray as a non-precious oxygen-reduction catalyst for proton exchange membrane fuel cells [J]. Journal of Power Sources, 2011,196(7):3548-3552.
[33] Gang Liu, Xuguang Li, Prabhu Ganesan, et al. Development of non-precious metal oxygen-reduction catalysts for PEM fuel cells based on N-doped ordered porous carbon [J]. Applied Catalysis B: Environmental, 2009,93(1-2):156-165.
[34] Xu J. B., Zhao* T. S., Zeng L. Covalent hybrid of hemin and mesoporous carbon as a high performance electrocatalyst for oxygen reduction [J]. international journal of hydrogen energy, 2012,37(21):15976-15982.
[35] Shinae Jun, Sang Hoon Joo, Ryong Ryoo, et al. Synthesis of new, nanoporous carbon with hexagonally ordered mesostructure [J]. Journal of the American chemical society, 2000,122(43):10712-10713.
[36] Yuta Nabae, Shogo Moriya, Katsuyuki Matsubayashi, et al. The role of Fe species in the pyrolysis of Fe phthalocyanine and phenolic resin for preparation of carbon-based cathode catalysts [J]. CARBON, 2010(10):2613-2624.
[37] Maldonado, Stephen, Keith J. Stevenson. Influence of Nitrogen Doping on Oxygen Reduction Electrocatalysis at Carbon Nanofiber Electrodes [J]. The Journal of Physical Chemistry B,2005,109(10):4707-4716.
[38] Nalini P. Subramanian, Xuguang Li, Vijayadurda Nallathambi, et al. Nitrogen-modified carbon-based catalysts for oxygen reduction reaction in polymer electrolyte membrane fuel cells [J]. Journal of Power Sources, 2009,188(1):38-44.
[39] Vijayadurga Nallathambi, Jong-Won Lee, Swaminatha P. Kumaraguru, et al. Development of high performance carbon composite catalyst for oxygen reduction reaction in PEM Proton Exchange Membrane fuel cells [J]. Journal of Power Sources, 2008,183(1):34-42.

Viser Technology Pte. Ltd.
Research and Application of Materials Science
DOI: 10.33142/rams.v6i2.14588

Research Article Open Access

Testing Method of Ion Corrosion of Reinforced Concrete and its Interface Optimization in the Marine Environment

Lei FAN[1, 2*], Jinhao ZHENG[1, 2], Chengtao WU[1, 2]

1. School of Civil Engineering and Architecture, Zhejiang University of Science & Technology, Hangzhou, Zhejiang, 310023, China
2. Zhejiang- Singapore Joint Laboratory for Urban Renewal and Future City, Hangzhou, Zhejiang, 310023, China

Corresponding Author: Lei FAN, E-mail: fanleigl@foxmail.com

Abstract

With the continuous improvement of the strategic position of marine resources in the world, improving the durability of marine engineering and increasing its service life has become an unavoidable topic. In the future, the development of protection optimization methods should be more diversified and integrated. In this paper, the testing method of ion corrosion of reinforced concrete and its interface optimization in the marine environment were investigated. It provides more possibilities for scientific research and technological innovation.

Keywords: Ionic erosion; Testing method; Marine Environments; interface optimization; Reinforced concrete

1 Introduction

If the chloride ion content exceeds the standard, the steel bars in concrete will be easily corroded, which will reduce the chemical corrosion resistance, wear resistance and strength of concrete, affect the durability of concrete, and thus lead to the decline of concrete quality. The detection of chloride ion penetration resistance is an important test to evaluate the durability of concrete, which is mainly used to determine the resistance of concrete to chloride ion penetration.

2 Physical Test Research Methods

2.1 Accelerated carbonization method

As carbon dioxide gradually penetrates into the concrete, it reacts chemically with the alkaline substances in it, lowering the pH of the concrete pore fluid, causing the steel passivation film to be destroyed and corroded. We call this process the carbonization of concrete. The accelerated carbonization method is to speed up the carbonization process of concrete, so that the steel bar corrodes quickly and shortens the test time. Alonso et al [1] used the accelerated carbonization method to measure the corrosion process of steel bars in concrete. It was found that there was a strong correlation between the corrosion rate of steel bars and the resistance of concrete. Although the accelerated carbonization method can cause steel corrosion in a short time and effectively shorten the test time, the simulated corrosion process is not consistent with the real situation. This method is more suitable for studying the steel corrosion caused by concrete carbonization, but cannot consider the steel corrosion problem in concrete eroded by chloride ions.

2.2 Chloride ion doping method

The internal chloride method (internal doping) is often used to study the corrosion rate of steel bars in concrete. Yalcyn and Ergun [2] used an internal doping method to study the effects of chloride ions and acetate ions on the corrosion of steel bars in concrete. The results show that chloride ion and acetate ion can significantly increase the initial corrosion rate of steel bars in concrete, and it is found that the corrosion rate of steel bars decreases exponentially with time. Although the internal doping method can effectively shorten the test time, this method is more likely to cause uniform corrosion of steel bars, which is different from the actual local corrosion. In addition, the internal doping method will affect the formation of passivation film on the surface of the steel bar, which will inevitably have a certain impact on the corrosion process of the steel bar. As a result, not many of the more recent studies have adopted this method.

2.3 Galvanostatic method

In order to accelerate the corrosion of steel bars in concrete, the galvanostatic method is also a commonly used test method. This method is to directly connect the steel bar to be corroded in the concrete to the DC power

Received on September 24, 2024; Accepted on October 31, 2024

supply, so that the steel bar corrodes quickly under the action of electric current. The test results show [3] that the corrosion rate of the steel bar increases with the increase of the crack width of the concrete, and the corrosion rate of the steel bar is inversely proportional to the concrete resistivity regardless of whether there is a crack in the concrete specimen. In addition, a prediction model of steel corrosion rate for reinforced concrete structures with cracks in tidal zone was established, and the effects of crack width, concrete protective layer thickness and concrete performance on steel corrosion rate were revealed [0]. Nossoni et al [0] used galvanostatic method to explore the relationship between the corrosion rate and corrosion products of steel bars and the pressure of reinforced concrete. An electrochemical-mechanical model of concrete protective layer cracking caused by chloride ion erosion was established. It can be seen that the galvanostatic method is mostly used to explore the problem of steel corrosion in cracked concrete.

2.4 Indoor natural diffusion method

In order to more realistically simulate the corrosion process of steel reinforcement in concrete components in the chloride salt environment, scholars have tried to conduct laboratory experiments by exposing reinforced concrete specimens to the simulated environment and waiting for chloride ions to naturally diffuse to the surface of steel bars and induce corrosion. We call this method the natural diffusion method. The effects of the relative humidity, chloride concentration, diameter of the reinforcement, the water-cement ratio of the concrete and the exposure time on the polarization curve of the reinforcement corrosion were discussed[0], and the prediction model of the reinforcement corrosion rate was proposed, and the correctness of the proposed model was verified by comparing and analyzing the measured data of the reinforcement corrosion rate with other studies. The calcium aluminate cement mortar specimens were immersed in NaCl solutions at concentrations of 0.5 mol/L and 1.5 mol/L for up to five years[0]. The effects of environmental factors (temperature and chloride ion concentration) and mortar specimen parameters (water-cement ratio) on the corrosion process of steel bars were studied, and the relationship between the corrosion rate of steel bars and the resistivity of mortar specimens was established. It can be seen that compared with the accelerated test method, the indoor natural diffusion test can simulate the corrosion process of steel bars relatively realistically, but the test time is longer.

2.5 Outdoor exposure test

Scholars have carried out outdoor exposure tests to monitor the corrosion law of reinforced concrete specimens or real structures in outdoor exposure environments. Different concentrations of NaCl solution were mixed into the simulated reinforced concrete bridge slab specimens and exposed to the outdoor environment for 5 years[0]. The corrosion rate of steel bars was monitored, and the effects of chloride ion concentration, ambient temperature, concrete resistance and corrosion time on the corrosion rate of steel bars were explored. Through nonlinear fitting, a long-term prediction model of steel corrosion rate was established. In addition, the exterior walls and terraces of two buildings in an inland and coastal area of Finland were selected as the research objects, and the corrosion rate of steel bars in the structure was continuously monitored within 25 months 22 years after the completion of the two buildings, and the effects of temperature, relative humidity, wind and rain, solar radiation, etc. on the corrosion rate of steel bars were discussed, and a prediction model of steel corrosion rate considering the influence of environmental factors was established[0]. Although outdoor exposure tests are more conducive to monitoring the corrosion of steel bars in concrete in real exposed environments, such tests tend to last for a long time and require a lot of manpower and material resources. At the same time, the outdoor exposure environment is relatively complex, and the test conditions cannot be controlled, so it is impossible to carry out systematic research on a certain influencing factor.

3 Interface Optimization Methods and Strategies

3.1 Concrete protective layer

Many tests have shown that even with the lowest water-cement ratio and high-quality concrete, the chloride ion content in the 12mm depth of the concrete surface is much higher than that in the 25～50mm depth range when exposed to the presence of chloride salts[0]. Therefore, in the project of chloride salt environment, the thickness of the concrete protective layer should not be less than 38mm, and preferably not less than 50mm. Considering the construction deviation, the thickness of the design protective layer should be selected as 65mm.

3.2 Rust inhibitors

The development of rust inhibitors began in the 70s of the 20th century, and has been applied and promoted in Japan, United States, the former Soviet Union and other countries. Rust inhibitor is a mixture or mixtures, generally acting on the metal surface, which can prevent or delay the destruction of chloride ions on the passivation film of steel bars, while maintaining the original properties of metal materials. The use of rust inhibitors should be accompanied by the use of low-permeability concrete to prevent the loss of rust inhibitors, and the addition of rust inhibitors is considered to be a more economical and effective measure. Commonly used rust inhibitors can be divided into inorganic rust inhibitors and organic rust inhibitors.

3.2.1 Inorganic rust inhibitors

Inorganic rust inhibitors are generally nitrite

corrosion inhibitors, and NO_2 and Cl have been found. The ratio of the rust inhibitor directly affects the rust inhibition efficiency of the rust inhibitor. When the value is higher than 0.5～0.6, nitrite rust inhibitors have a good rust inhibitor effect[0]. Howl [0] discussed the permeability and corrosion resistance of $Ca(NO_2)_2$ in concrete. It was found that it had good permeability in concrete with high water-cement ratio, and had a good protective effect on steel bars under low chloride salt corrosion, but poor protection against steel bars under high chloride salt environment. The experimental results of Page [0] on sulfite are similar to those of Ngala. It is proposed that a layer of cement mortar mixed with nitrite should be added to the surface of the nitride-coated concrete in the process of use. Thereafter, Na_2PO_3F was developed and came out, which once attracted widespread attention. Alonso [0] studied the corrosion inhibition effect of Na_2PO_3F in reinforced concrete. The results showed that a certain concentration of Na_2PO_3F could significantly change the reinforcement potential in concrete, make it move forward, increase the impedance value, and reduce the electric flux. Hasson [0] confirmed that Na_2PO_3F can increase the compactness of concrete, thereby reducing Cl^- of erosion infiltration. Ngala [0] pointed out that the permeability of Na_2PO_3F in concrete is poor, and it can only penetrate to a depth of 5mm below the concrete surface to effectively protect the steel bar.

3.2.2 Organic rust inhibitors

Organic rust inhibitors have little toxic effect and are more friendly to the environment, so they have been vigorously developed, and organic rust inhibitors migrate to the surface of steel bars through penetration and diffusion to form a dense protective film, because they usually carry hydrophobic groups, which can not only Cl^- and other harmful ions, which also have a shielding effect on H_2O and O_2, thereby slowing down the electrochemical reaction rate of steel corrosion and achieving the purpose of rust inhibition. In the 90s of the 20th centuries, the United States Cortec company developed an organic rust inhibitor whose main component is amino carboxylate, which can change the previous passive penetration, can actively migrate to the surface of the steel bar to form a film, inhibit corrosion, so it is also called migratory rust inhibitor (MCI, Migrating corrosion inhibitor). The corrosion inhibitor with alkylamine ethanol as the main component was studied by Morris et al[0]. It was found that the rust inhibitor also had a certain migration ability, and it was also effective against the low chloride salt environment ($[Cl^-]$ ＜0.2%). Jamil et al. [0] studied the alcohol amine organic rust inhibitor, which showed that it would form a protective film on the surface of steel bar after infiltrating into concrete. The electrochemical results show that the film resistance and charge transfer resistance are much higher. In the process of studying amino alcohol rust inhibitors, secondary ion mass spectrometry was used to prove the particles and Cl^- of these rust inhibitors[0]. There is a competitive adsorption situation, which can displace the Cl^- on the surface of the steel bar, and form a dense and stable protective film. The diffusion properties of amino ethanol organic rust inhibitors in concrete were discussed by Tritthart et al [0]. The results showed that the rust inhibitors could not only migrate through the pore fluid in concrete, but also spread in the vapor phase through microcracks in concrete.

3.3 Cathodic protection

The formation of yin and yang on the surface of the steel bar is a prerequisite for the occurrence of electrochemical corrosion, where the cathode is cementite and the anode is ferrite. Anodizing forms an oxide film on the surface of the rebar to prevent the generation of galvanic corrosion. On the basis of electrochemistry, the cathodic protection method has also been developed to keep the steel bar in the cathode state and thus reduce the corrosion of the steel bar. The principle of cathodic protection is that the critical concentration of chloride ions decreases as the electrochemical potential of the steel bar decreases. The penetration of chloride ions in the protective layer is inhibited, thereby reducing the diffusion rate of chloride ions, thus ensuring the durability of the concrete structure [0]. Engineering practice has shown that the use of cathodic protection in concrete structures can effectively prevent chloride ion erosion, thereby preventing corrosion of steel bars. Commonly used cathodic protection methods include impressed current method and sacrificial anode method.

3.3.1 Impressed current method

The impressed current method refers to the cathodic protection effect by providing cathodic protection current through an external constant current power supply or potentiostat, which is released through the auxiliary anode and flows from seawater to the protected structure. The advantages of an impressed current include: (1) the protection effect is better and no pollution; (2) No consumption of non-ferrous metals; (3) The later maintenance cost is low. However, the upfront investment cost is high.

In 2002, Li Yan et al. [22] put forward the related ideas of cathodic protection for offshore platforms, including sacrificial anode cathodic protection method and impressed current emergency protection method. In 2003, Xiong [23] put forward a self-developed cathodic protection monitoring system, which provided valuable experience for the continuous improvement and innovation of the cathodic protection monitoring and detection system. It also proposed a dual-electrode potential detection probe with strong impact and vibration resistance, which was more helpful for measuring the platform potential. In 2006, Wu Lie et al. [24] put forward a new technology of impressed current cathodic protection with central suspension at the 14th Asia-Pacific Corrosion Control Conference. It provided a

new idea for cathodic protection design of bridges, docks, platforms and other facilities. Since 2010, impressed current cathodic protection technologies for different types of offshore platforms have been put forward continuously, among which Yin's impressed current cathodic protection technology for jacket platforms in 2012 and Luan's impressed current cathodic protection technology for jack-up platforms in 2015 have both developed a complete set of impressed current cathodic protection technologies from the aspects of impressed current system materials, equipment, design and installation technology [25-26]. In 2017, Huang successfully applied the first self-developed ICCP impressed current cathodic protection life extension system for offshore jacket structures on the platform of CNOOC Lufeng 13-2WHP.

3.3.2 Sacrificial anode method

In 1823, Humphrey Davy[27], an Englishman, found that connecting zinc with the copper skin wrapped on a wooden boat could effectively prevent the copper skin from rusting. In more and more subsequent practical use, people noticed that with the increase of corrosion products attached to the anode surface, the protective ability of the anode was also weakened[28]. Since the 20th century, the cathodic protection of sacrificial anode has been paid more and more attention. In 1913, the Metal Society held in Geneva officially named the cathodic protection of sacrificial anode as "electrochemical protection"[29]. Since then, the research on sacrificial anodes has been carried out all over the world, and the main research directions focus on exploring the protection mechanism of sacrificial anodes, discussing the corrosion behavior of materials protected by sacrificial anodes in different environments, and developing high-efficiency and low-cost anode materials. Beccaria [30-31] et al. put several metals and alloys in the deep-sea environment of the Gulf of Mexico from 1083 to 1945 m, and investigated the performance of materials as protected cathodes. The results showed that the sea area, depth and time in the sea would affect the size of the protection current required by the metal, in general, the deeper the sea, the smaller the protection current required by the material as a cathode. Robin [0] studied the corrosion of low carbon steel and stainless steel protected by sacrificial anode in their own simulated 2500m deep sea environment. On the one hand, in the high-pressure environment, the low carbon steel does not appear "hydrogen embrittlement", but there are a large number of mixtures containing Ca^{2+} and Mg^{2+} deposited on the surface. It requires a large protective current to resist rust. On the other hand, the surface finish of carbon steel has a great impact on the difficulty of corrosion, the smoother the surface, the easier it is to corrode, and the stainless-steel shows "pitting" in the same period. It is analyzed that this is due to the local failure of the surface passivation film, which is independent of the deposit, indicating that the cathodic protection current required by stainless steel at high and atmospheric pressure is similar. Funahashi [33] explored the cathodic protection performance of different sacrificial anode materials. The results show that the protection current provided by the poor anode material is uneven. It will produce acidic substances on the surface of the anode concrete. The research also shows that the anode material coated with titanium metal oxide have better protective effect.

3.4 High-performance concrete

In generally, reinforced concrete structures, chloride ions must penetrate through concrete of different thicknesses to reach the surface of the reinforcement, so improving the durability of reinforced concrete structures can also be achieved by enhancing the erosion resistance of the concrete matrix. There are two main technical ways to improve the resistance of concrete matrix to medium erosion: On the one hand, the incorporation of auxiliary cementitious materials (SCMs) can reduce permeability; On the other hand, the incorporation of erosion inhibition materials inhibits water transport and reduces the chloride permeability of concrete. As technology advances, new erosion inhibition materials are being developed and applied to concrete to improve the durability of reinforced concrete.

Nanotechnology provides new opportunities for mankind to study concrete materials, and concrete research itself is a multidisciplinary system, using nanotechnology to change the structure and properties of C-S-H gels, one of the mechanisms is the lack of tetrahedral grafting polymers on the C-S-H silicon chain [34] or the use of organic matter to form a bond between the C-S-H layers, such as layered di-hydroxides, carbon nanomaterials, nanoparticles, etc., to optimize the properties of concrete.

3.4.1 Graphene nanomaterials

Graphene oxide (GO) contains many oxygen-containing functional groups, including -OH, -COOH, C=O, CH(O)CH-, etc. Graphene and its oxides can not only react with hydration products, affect pore structure, etc., but also change the transport properties of cement-based materials.

Du et al. [35-36] improved the chloride ion permeability resistance of cement-based materials through graphene nanosheets. When adding 1.5% graphene nanosheets, the water penetration depth, chloride ion diffusion coefficient and chloride ion migration coefficient decreased by 80%, 80% and 37% respectively. The result showed that more than 50% of the reduction effect was achieved by increasing the tortuosity of the cement slurry, and the other effect was to improve the pore structure of the cement slurry. Graphene nanosheets are well distributed in cement matrix and can improve the performance of cement-based materials. After adding 2.5% graphene nanosheets, the most acceptable pore size of cement-based materials is reduced by 30%, and the effect

of graphene nanosheets will not be further improved if the graphene nanosheets are further increased, and the effect of reducing water transport by more than 20% is contributed by the increase of the tortuosity of the transmission path, and the decrease of chloride diffusion coefficient is almost all caused by the change of tortuosity. After the content of graphene nanosheets exceeded 7.5%, the inhibitory ion transport effect of the nanomaterials began to weaken due to the agglomeration of the nanomaterials. The graphene oxide nanomaterials were prepared by in-situ polymerization by Gao Ruijun [37]. It is found that the graphene oxide nanomaterials had good dispersion in the aqueous solution and the centrifugal solution of the cement slurry. The graphene oxide nanomaterials formed graphene oxide end-caps on the surface of the hydration products, which improved the compactness of the matrix, could block chloride ion transport and improve the chloride ion permeability of concrete, and the electric flux of concrete mixed with 0.15% graphene oxide decreased by 40%.

3.4.2 Nano-silica

Said et al. [38] found that the strength of concrete mixed with nano silica was improved, and the total porosity, maximum pore size and electric flux of 2% nano silica 0.4 were reduced by 33%, 40% and 49% respectively compared with the benchmark group, and the nano silica could improve the chloride ion permeability of concrete, mainly due to the reaction of nano silica with calcium hydroxide to generate more C-S-H and the filler effect of nano silica. Feng et al. [39] added pre-dispersed silica into cement-based materials, which can greatly improve their properties. The addition of 6% silica and 0.2% ball mill pre-dispersed silica can significantly reduce the chloride content in the 0-4mm surface of concrete, which is only 60% of the benchmark group, thanks to the formation of a denser structure and more gel. Chen et al. [40] added hydrophobic modified nano-silica into cement paste, which can react with calcium hydroxide generated by cement hydration to form substances containing hydrophobic groups, and finally can reduce the most probable pore size and water absorption. Wang et al. [41] hydrolyzed ultrafine silica oligomer and then used it to treat the surface of cement-based materials. It was found that the water absorption could be reduced by 46.4%, but the silica oligomer needed to be hydrolyzed under the condition of pH 4.0, and acidic conditions would destroy cement-based materials to some extent. Li [42] used nano-SiO_2 to improve the performance of concrete. Adding 1% nano-SiO_2 can effectively improve the anti-corrosion ability of concrete, but it will affect the workability of concrete, and the water demand will increase sharply and the slump will decrease. Gu [43] modified nano- SiO_2 particles by polycarboxylic acid to solve the problem of dispersion and penetration, and then coated on the surface of cement-based materials can reduce the water absorption of cement-based materials.

3.4.3 Fatty acid materials

Hydrophobic materials with fatty acid salts can also be used to improve the properties of concrete substrates, and their calcium salts, ammonium salts, and butyl stearate are the most common types.

Calcium stearate is a hydrophobic compound of fatty acids and calcium ions, which can reduce the water absorption rate and chloride penetration depth of concrete, and improve the durability of concrete [44-45]. Calcium stearate is a component of petrolatum corrosion pastes and can be used to protect steel structures in coastal environments [0]. Maryoto [0] added calcium stearate to concrete with water cement ratio of 0.44, and added 1 kg calcium stearate per cubic meter of concrete. Compared with the reference group, the water absorption decreased from 2.00% to 0.94%, while the corrosion quality loss of steel bars decreased from 11.79% to 4.18%, indicating that calcium stearate can improve the chloride ion corrosion resistance of concrete, and the compressive strength of concrete has little change. Maryoto et al [0] Added 0.4% calcium stearate to the cement-based material can reduce the water absorption rate of concrete by 53%, and at the same time, it has little effect on strength, chloride ion corrosion can be reduced by 28.5%, and the chloride penetration depth can be reduced by 15%. The addition of 4 kg of calcium stearate per cubic concrete can increase the permeability of concrete by 50% while guaranteeing minimal change in concrete strength. Wu et al. [0] used calcium stearate to change the hydrophilicity of the mortar, and the contact angle of the mortar could reach 130° , and calcium stearate could reduce the water absorption rate of the mortar and improve the chloride ion permeability of the mortar, but the treatment steps of calcium stearate were more complicated.

3.4.4 Silanes, siloxanes and their derivatives

As an important chemical functional material, silane, siloxane and its derivatives are stably dispersed in the aqueous phase with nanometer or micron size particles, which have many advantages such as improving the toughness of hardened cement slurry and enhancing the anti-cracking and impermeability of cement slurry. However, the addition of silanes, siloxanes and their derivatives will significantly affect the cement hydration process, which is mainly manifested in delaying cement hydration, and then affecting the hardening and strength growth of cement-based materials.

He et al. [0] used 66% octyl triethoxysilane, 2% sodium dodecyl sulfonate and 32% water to prepare silane emulsion. When the silane content is 1%, the strength of the mortar decreases significantly, and the water absorption rate also decreases, but the water absorption rate changes little if the silane content continues to increase. The addition of silane can effectively improve the erosion resistance of the mortar to sulfuric acid solution. Vivian et al [0] used polymethylsiloxane to modify kaolin and silica fume, and

then used it to change the surface structure of concrete. The Different series of tests have shown that super-hydrophobicity can be achieved by adding 0.5% kaolin or 5% silica fume. Zhang et al [0] used polydimethylsiloxane and silane coupling agent to modify micro-silica powder, which can improve the contact angle of cement-based materials and reduce the porosity.

3.5 High-performance steel bars

In 1933, United States scholars added a small amount of copper, nickel and other corrosion-resistant elements to carbon steel for the first time to develop weathering steel, that is, atmospheric corrosion-resistant steel. In 1951, United States scholars developed seawater-resistant steel for the first time. Subsequently, various countries gradually carried out research on corrosion-resistant steel bars. Some researchers [0] added corrosion-resistant elements such as Cr and Ni to carbon steel to improve the corrosion resistance of steel bars. The results show that the corrosion resistance of steel bars containing 0.40%～0.70% Cr and 0.30%～0.50% Ni is better. At the same time, the content of Cr and Ni in the reinforcement is directly proportional to the critical pitting potential. Some researchers [54-55] added corrosion-resistant elements such as Cu and Mo to carbon steel to improve the corrosion resistance of steel bars. The addition of Mo to stainless steel can promote the increase of Cr content in the passivation film, and improve the stability and pitting resistance of the passivation film. Halada et al. [56] studied the influence of Mo and N elements on the corrosion resistance of steel bars. The results showed that the addition of Ni and Mo elements would form $MONi_4$ films, which would improve the stability of the passivation films. Hermas et al.[0] studied the influence of Si element on the corrosion resistance of steel bars, and showed that Si element can form a silicon-rich film on the surface of steel bars, thus improving the pitting corrosion resistance of stainless steel. Yoshioka et al.[0] found that the stability elements Nb and Ti can slow down the occurrence of pitting corrosion of steel bars and reduce the corrosion rate of steel bars.

Corrosion-resistant steel bars are an important means to prevent rust damage of steel bars in concrete. Although stainless steel can directly avoid the occurrence of steel corrosion, the price of stainless steel is about 7 times that of general carbon steel, and the high cost directly hinders the use of stainless-steel bars. Chromium has significant corrosion resistance, and adding a small amount of chromium to ordinary carbon steel can form a dense protective layer on the surface of the steel bar and improve the corrosion resistance of the steel bar. On the basis of alloying, chromium is added to the steel bar to form a corrosion-resistant low-alloy steel, which not only has an advantage in price, but also can prolong the service life of the steel bar in terms of performance.

6 Conclusion and prospect

At present, the research on improving the durability of reinforced concrete in marine engineering mainly focuses on concrete and steel bars, and there are few studies on the lifting methods of the steel-concrete transition zone. It is one of the key issues in the development of marine engineering to combine multiple interface optimization methods to achieve the highest protection effect under economic conditions.

Acknowledgments: This work were supported by Natural Science Foundation of Zhejiang Province (LQ23E080003), a Doctoral program of Zhejiang University of science and technology (F701104L08) and The Special Fund Project of Zhejiang University of Science and Technology's Basic Scientific Research Business Expenses in 2023 (2023QN016).

Conflict of interest: No potential conflict of interest was reported by the authors.

References

[1] C. Alonso, C. Andrade, J. A. González. Relation between concrete resistivity and corrosion rate of the reinforcements in carbonated mortar made with several cement types[J]. CEMENT CONCRETE RES, 1988(18):687-698.

[2] H. Yalcyn, M. Ergun. The Prediction of corrosion Rates of Reinforcing Steels in Concrete[J]. CEMENT CONCRETE RES, 1996(26):1593-1599.

[3] M. Otieno, H. Beushausen, M. Alexander. Resistivity-based chloride-induced corrosion rate prediction models and hypothetical framework for interpretation of resistivity measurements in cracked RC structures[J]. MATER STRUCT, 2015,49(6):2349-2366.

[4] M. Otieno, H. Beushausen, M. Alexander. Chloride-induced corrosion of steel in cracked concrete—Part II: corrosion rate prediction models[J]. CEMENT CONCRETE RES, 2016(79):386-394.

[5] G. Nossoni, R. S. Harichandran. Electrochemical-mechanistic model for concrete cover cracking due to corrosion initiated by chloride diffusion[J]. J MATER CIVIL ENG, 2014,26(6):4014001.

[6] B. Zhou, X. Gu, H. Guo, et al. Polarization behavior of activated reinforcing steel bars in concrete under chloride environments[J]. CONSTR BUILD MATER, 2018(164):877-887.

[7] C. Argiz, M. A. Sanjuán, P. C. Borges, et al. Modeling of corrosion rate and resistivity of steel reinforcement of calcium aluminate cement mortar[J]. ADV CIV ENG, 2018(11):1-9.

[8] T. Liu, R. W. Weyers. Modeling the dynamic corrosion process in chloride contaminated concrete structures[J]. CEMENT CONCRETE RES, 1998,28(3):365-379.

[9] A. Köliö, T. A. Pakkala, H. Hohti, et al. The corrosion rate in reinforced concrete facades exposed to outdoor environment[J]. MATER STRUCT, 2016,50(1):22-25.

[10] [10] ACI Committee 201. Guide to Durable Concrete [R].

Farmington Hills: American Concrete Institute, 2016.
[11] C. Andrade, C. Alonso, J. A. Gonzalez. Some laboratory experiments on the inhibitor effect of sodium nitrite on reinforcement corrosion[J]. CEMENT CONCRETE AGGR, 1986,8(2):110-115.
[12] V.T. Ngala, C.L. Page, M.M. Page. Corrosion inhibitor systems for remedial treatment of reinforced concrete. Part 2: sodium monofluorophosphate[J]. CORROS SCI, 2003, 45(7):55-58.
[13] M. M. Page, V. T. Ngala, C. L. Page. Corrosion inhibitors in concrete repair systems[J]. MAG CONCRETE RES, 2000,52(2):25.
[14] C. Alonso, C. Andrade, C. Argiz, et al. Na2PO3F as inhibitor of corroding reinforcement incarbonated concrete[J]. CEMENT CONCRETE RES, 1996,26(3):405-415.
[15] C. M. Hansson, L. Mammoliti, B. B. Hope. Corrosion inhibitors in concrete—part I: the principles[J]. CEMENT CONCRETE RES, 1998,28(12):33-37.
[16] Y. B. Gao, J. Hu, Q. Liu, et al. Application and prospect of reinforcement rust inhibitors[J]. Journal of Xiamen University, 2015,54(05):713-720.
[17] W. Morris, A. Vico, M. Vazquez. Corrosion of reinforcing steel by means of concrete resistivity measurements[J]. CORROS SCI, 2002(44):81-99.
[18] H. E. Jamil, A. Shriri, R. Boulif, et al. Corrosion behaviour of reinforcing steel exposed to an amino alcohol based corrosion inhibitor[J]. CEMENT CONCRETE COMP,2004,27(6):33-38.
[19] Maeder U. A New Class of Corrosion Inhibitors for Reinforced Concrete [J]. Special Publication, 1996, 163: 215-232.
[20] J. Tritthart. Transport of a surface-applied corrosion inhibitor in cement paste and concrete[J]. CEMENT CONCRETE RES, 2003,33(6):25-29.
[21] L. Betrolini, B. Elsener, P. Pediferri, et al. Corrosion of steel in concrete: prevention, diagnosis, repair[M]. Hoboken:John Wiley &Sons, 2013.
[22] Y. Li, Z. F. Li. Cathodic protection for offshore platforms[J]. Shipbuilding of China, 2002,43(10):162-164.
[23] X. Y. Xiong, T. Yan, C. B. Xu, et al. Development and application of cathodic protection monitoring system for offshore platforms[J]. Journal of Tropical Oceanography, 2003(1):70-75.
[24] L. Wu, C. Y. Wu, Z. Y. Ni. Practice of research on the design and application of cathodic protection engineering of industrial steel structures in offshore ports[C]. Beijing: CHINESE SCI BULL, 2006.
[25] P. F. Yin, W. Zhang, Z. K. Xu, et al. Impressed current cathodic protection technology for jacket platforms[J]. Corrosion & Protection, 2012,33(S2):18-22.
[26] Y. Luan, C. J. Ma, J. P. Hu. Impressed current cathodic protection technology for jack-up platforms[J]. Total Corrosion Control, 2015,29(10):33-37.
[27] S. X. Hu. Cathodic Protection Brochure[D]. Beijing:Chemical Industry Press, 1999.
[28] R. B. Teel, D. B. Anderson. The effect of iron in galvanic zinc anodes in sea water[J]. CORROS SCI, 1956(12):343-349.
[29] H.H. Bibikov, E. R. Ryublinsky, B. Povarova. Electrochemical protection of seagoing vessels[J]. National Defense Industry Press, 1975(22):15.
[30] K. P. Fischer. Field testing of CP current requirements at depth down to 1300 mon the northern Norwegian continental shelf from 63°to 67°N [C]. Corrosion, Houston: NACE, 1999.
[31] A.M. Beccaria, P. Fiordiponti, D. Mattongno. The effect of hydrostatic pressure on the corrosion of nickel in slightly alkaline solutions containing Cl- ions[J]. CORROS SCI, 1989,29(4):403-413.
[32] T. Alastair. Cathodic protection at a simulated depth of 2500m[J]. CORROS-US, 2000(21):134.
[33] M. Funahashi, T. Sirola, D. Mcintaggart. Cost effective cathodic protection system for concrete structures[J]. MATER PERFORMANCE, 2014,53(11):32-37.
[34] L. Raki, J. Beaudoin, R. Alizadeh, et al. Cement and Concrete Nanoscience and Nanotechnology[J]. MATER, 2010,3(2):918-42.
[35] H. Du, H. J. Gao, S. D. Pang. Improvement in concrete resistance against water and chloride ingress by adding graphene nanoplatelet[J]. CEMENT CONCRETE RES, 2016(83):114-23.
[36] H. Du, S. D. Pang. Enhancement of barrier properties of cement mortar with graphene nanoplatelet[J]. CEMENT CONCRETE RES, 2015(76):10-19.
[37] R. J. Gao. In-situ polymerization of GO-PCE and its effect on the properties of cement-based materials and its mechanism[D]. Beijing:China Academy of Building Materials Science, 2020.
[38] A. M. Said, M. S. Zeidan, M. T. Bassuoni, et al. Properties of concrete incorporating nano-silica[J]. CONSTR BUILD MATER, 2012(36):838-844.
[39] L. Feng, P. Zhao, Z. Wang, et al. Improvement of mechanical properties and chloride ion penetration resistance of cement pastes with the addition of pre-dispersed silica fume[J]. CONSTR BUILD MATER, 2018(182):483-492.
[40] H. Chen, P. Feng, Y. Du, et al. The effect of superhydrophobic nano-silica particles on the transport and mechanical properties of hardened cement pastes[J]. CONSTR BUILD MATER, 2018(182):620-628.
[41] D. Wang, P. Yang, P. Hou, et al. Effect of SiO2 oligomers on water absorption of cementitious materials[J]. CEMENT CONCRETE RES, 2016(87):22-30.
[42] Li Guhua. The effect of nanomaterials on the durability of concrete[D]. Chongqing: Southwest Jiaotong University, 2006. (in Chinese)
[43] Gu Yue. Study on the properties of core-shell nano-SiO2 modified cementitious materials[D]. Nanjing:Southeast University, 2017. (in Chinese)
[44] A. Maryoto, G. B. Sthenly, S. H. N. Intang, R. Setijadi. Effect of calcium stearate in the mechanical and physical properties of concrete with PCC and Fly ash as binders[J]. MATER, 2020,13(6):1394.
[45] A. Maryoto, B. S. Gan, N. I. S. Hermanto, et al. CORROS-US

resistance of self-compacting concrete containing calcium stearate[J]. J ENG SCI TECHNOL, 2018(13):3263-3276.

[46] Qian Bei. Research on corrosion protection technology in steel structure splash zone and corrosion inhibitor under dry and wet alternation[D]. Qingdao: Chinese Academy of Sciences, 2014.

[47] A. Maryoto. Resistance of Concrete with Calcium Stearate Due to Chloride Attack Tested by Accelerated[J]. CORROS-US, 2017(171):511-516.

[48] A. Maryoto, B. S. Gan, H. Aylie. Reduction of chloride ion ingress into reinforced concrete using a hydrophobic additive material[J]. J TEKNOL, 2017, 79(2):45-48.

[49] A. Maryoto. Improving Microstructures of Concrete Using $Ca(C_{18}H_{35}O_2)2$[J]. Procedia Engineering, 2015(125):631-637.

[50] He Kui. Research on organic functional materials for concrete in harsh environments and their protection mechanisms[D]. Hangzhou: Zhejiang University, 2014.

[51] I. Flores-Vivian, V. Hejazi, M. I. Kozhukhova, et al. Self-assembling particle-siloxane coatings for superhydrophobic concrete[J]. ACS APPL MATER INTER, 2013,5(24):13284-13294.

[52] B. Zhang, Q. Li, X. Niu, et al. Influence of a novel hydrophobic agent on freeze–thaw resistance and microstructure of concrete[J]. CONSTR BUILD MATER, 2021(269):121294.

[53] J. Horvath, H. H. Uhlig. Critical potentials for pitting corrosion of Ni, Cr-Ni, Cr-Fe, and related stainless steels[J]. J ELECTROCHEM SOC, 1986,115(8):791-794.

[54] S. Lameche, R. Nedjar, H. Rebbah, et al. CORROS-US and passivation behaviour of three stainless steels in different chloride concentration[J]. ASIAN J CHEM, 2008,20(4):2544.

[55] J. Shu, H. Bi, X. Li, et al. The effect of copper and molybdenum on pitting corrosion and stress CORROS-US cracking behavior of ultra-pure ferritic stainless steels[J]. CORROS SCI, 2012(57):89-98.

[56] G. P. Halada, D. Kim, C. R. Clayton. Influence of nitrogen on electrochemical passivation of high-nickel stainless steels and thin molybdenum-nickel films[J]. CORROS-US, 1996,52(1):36-45.

[57] A. A. Hermas, K. Ogura, S. Takagi, et al. Effects of alloying additions on corrosion and passivation behaviors of type 304 stainless steel[J]. CORROS-US, 1995,51(1):3-10.

[58] K. Yoshioka, S. Suzuki, N. Kinoshita, et al. ultra-low C and N high chromium ferritic stainless steel[J]. KAWASKTA STEEL TECH REP, 1986(14):101-112.

Publisher: Viser Technology Pte. Ltd.

URL: www.viserdata.com

Add.:111 North Bridge Rd, #21-01 Peninsula Plaza,
Singapore 179098

ISSN 2661-4456